Title
The Mechanical Properties of Spray-Formed Oxide Dispersion Strengthened Steel Alloy 14YWT

Author
Graham, Jeffrey John

Publication Date
2020

The Mechanical Properties of Spray-Formed Oxide Dispersion Strengthened Steel Alloy 14YWT

by

Jeffrey John Graham

A dissertation submitted in partial satisfaction of the

requirements for the degree of

Doctor of Philosophy

in

Engineering—Nuclear Engineering

in the

Graduate Division

of the

University of California, Berkeley

Committee in charge:

Professor Peter Hosemann, Chair
Professor Masamilliano Fratoni
Professor Mary Scott

Spring 2020

The Mechanical Properties of Spray-Formed Oxide Dispersion Strengthened Steel Alloy 14YWT

Abstract

The Mechanical Properties of Spray-Formed Oxide Dispersion Strengthened Steel Alloy 14YWT

by

Jeffrey John Graham

Doctor of Philosophy in Engineering—Nuclear Engineering

University of California, Berkeley

Professor Peter Hosemann, Chair

Next generation nuclear reactor concepts employ higher temperatures, harder neutron fluxes, and generally a more difficult material environment than the current fleet. This, in conjunction with economic demands for longer periods between outages and higher fuel utilization, require radiation-hardened materials capable of withstanding such conditions. Oxide dispersion strengthened (ODS) steel alloys are one such potential class of materials. These are induced to have nanostructures within their bulk which provide distinct advantages, but which also preclude the use of consolidation and joining techniques which would degrade or destroy the same features. Cold spraying is an additive technique which has been explored as a possible avenue toward efficiently creating bulk parts out of ODS-precursor feedstock, with superior efficiency and properties compared to other means of consolidation, most commonly hot extrusion.

This work has assessed the mechanical properties of one very promising ODS alloy, 14YWT, as formed by the cold spray technique. Results were not promising: the samples were brittle and weak, while not completely free of some of the disadvantages of hot extrusion. Additionally, the demands of the cold-spray process were determined to be distinctly limiting as to the formation of the feedstock material, with negative impacts on the quality of the nanostructuring that forms the unique and desirable feature of the alloy. Though additional material processing and quality control may be able to remediate some of these defects, this work concludes that cold spraying is not a suitable mechanism for consolidating ODS alloys.

To my beloved Wife, who has always been a rock in times of trial; To my family, and most especially my brother Joe, who have always had my back; And to certain others whose names are written in light.

Contents

List of Figures

List of Tables

Acknowledgments

I'd like to begin by thanking my advisor, Professor Peter Hosemann, whose support and engagement made it possible for me to begin and complete my Doctorate. Next, my coworkers, particularly Evan Still, Hi Vo, and Bengisu Yasar who helped me immensely with various bits of equipment and experimental techniques. This dissertation would not exist without them.

Special thanks must go to Col D. Walters, Col R. Kiziah, and Brig Gen Goodfellow, without whose support and intervention I'd have never begun this PhD.

And, finally, a huge block of thanks to my beloved wife, M. Elizabeth "Bree" Humphries, without whose support I'd have been wholly unequal to the task.

Chapter 1

Introduction

Nuclear reactors have a demonstrated record as a clean, reliable, and extremely powerful source of energy. Global demand for such energy is increasing rapidly, while the need to eliminate emissions provides powerful incentives to build an energy infrastructure that does not rely upon hydrocarbon combustion. Nuclear power, with its incredible energy density and high reliability, can make great contributions to this set of objectives, even with present technology. To fully realize the promise of atomic power, however, advanced reactors, those that have longer core lifetimes, experience higher working temperatures, are subjected to greater neutron fluences, and must contain novel coolants, are under development. These design concepts, in turn, require materials that can retain their engineered properties under such circumstances, while being economically manufacturable. One review observed that 100 gigawatt-days/tonne (GWd/t) is not out of the question: under such circumstances, a material must be resistant to neutron irradiation, it must resist deformation from internal damage or external forces, and it must resist corrosion from the coolant and mechanical supports. [82]

This is a tall bill. It is added to by demands for cost-effective manufacturability. This work seeks to address this last concern: a nanostructured ferritic alloy, 14YWT, has promise as a material which will meet the engineering requirements. Its manufacture, however, is hindered by the need to create and retain nanostructures within its bulk. This work explores the possibilities of a process called cold spraying, which would save time and material should it prove capable of producing satisfactory parts. In order to characterize what is meant by satisfactory, the remainder of this introduction will discuss the application environment, the challenges the material faces, and the principles underlying 14YWT's promise as a radiation-resistant material.

1.1 Nuclear Energy

Let the existence of atoms, with their nuclei and clouds of electrons, serve as the starting point for this discussion of nuclear energy. The nucleus itself is comprised of protons and neutrons—nucleons—with the number of the former corresponding to the chemical species and the neutrons determining the particular isotope of that species. Customarily, the numbers for proton, neutron, and total nucleon number are Z, N, and A; A is the number used for indicating the isotope, e.g. ^{235}U.

Interactions within the nucleus give rise to stable, metastable, or unstable conditions which form the headwaters of nuclear power. Most important is the competition between electrostatic repulsion between the protons, which provides the tremendous potential energy of nuclear fission, and the strong force, which attracts protons to neutrons and holds the nucleus together. The coulomb force has infinite range, diminishing according to the inverse square law, but the strong force between nucleons diminishes slightly faster than exponentially, giving a finite range. The interplay between nuclear size, nucleon interactions as a function of range, and the binding energy is modeled to an admirable degree of accuracy by the Bethe-Weizäcker Formula, an understanding of which is fruitful but beyond the scope of this paper. It suffices to remark that there exists the curve of binding energy,[1] fig. 1.1, so that useful work may be liberated by changes in the proton or neutron number. For example, a fission reaction such as $\mathrm{n}_0 + {}^{235}\mathrm{U} \longrightarrow {}^{144}\mathrm{Xe} + {}^{89}\mathrm{Sr} + 3\mathrm{n}_0$ has two fragments and three neutrons produced. The fragments themselves are significantly higher on the curve than the starting uranium, and have less mass per unit nucleon than when in the uranium nucleus. This lost mass, converted to energy, is in accordance with Einstein's most famous derivation, $E = mc^2$, and is carried off by the recoil of the daughter nuclei away from each other.

The previous example also includes the emission of neutrons during fission, enabling a chain reaction should some those neutrons act as triggers for subsequent fission reactions. Likewise, the fission fragments chosen are atypical only insofar as one is stable, and another is relatively stable. Fission fragments are frequently highly imbalanced in their proton and neutron distribution, leading to decay processes that produce a torrent of high-energy gamma rays, beta particles (high-energy electrons), alpha decay (production of a ^{4}He nucleus), and further neutrons. These provide an intense radiation field for the structural materials in the reactor core: for every megajoule of heat produced, there are approximately 10^{16} neutrons.

These neutrons are born with significant energy, about 2 MeV on average. Their spectrum is well represented by the Watt distribution $P(E_n) = 0.453 \sinh(\sqrt{2.29 E_n}) \exp(-1.036 E_n)$ [85], the numerical constants having been fit empirically, and is plotted in fig. 1.2. Such neutrons are referred to as "fast." At the same time, the fission cross-section of ^{235}U as a function of energy is shown in fig. 1.3, and it may be seen that the probability of an interaction increases dramatically as neutrons lose energy. The principle of the thermal reactor is to moderate neutrons from their birth energy to $kT_{moderator}$ in order to maximize the likelihood of neutrons causing fission and maintaining the reaction.

Conceptually, the neutron economy of a reactor may be understood by the four-factor formula $k_\infty = \epsilon p f \eta$. To unpack this, first consider a universe with discretized time, so that the neutron population at t_0 is wholly unambiguous, and likewise at t_1. The multiplication

---

[1] Also the title of an interesting book on the development of the atom bomb by John McPhee.

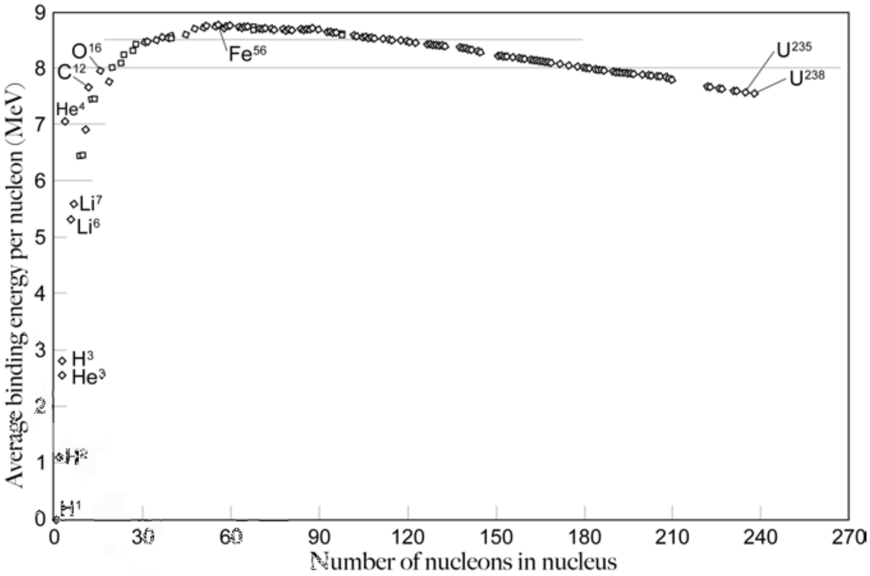

Figure 1.1: The Curve of Binding Energy, showing the amount of work would be necessary to remove a nucleon from a particular isotope. Motion toward the peak at ^{56}Fe liberates energy. [36]

factor k relates these populations as $n(t_1) = kn(t_0)$; k_∞ is the multiplication in an infinitely large reactor. $k = 1$ is clearly a steady-state condition, reflecting a critical reactor. p is the probability that a neutron will be thermalized instead of captured without causing fission, f is the probability that a thermal neutron will be absorbed in fuel rather than moderator, η is a factor to account for fissions caused by fast neutrons, and η is the neutron reproduction factor. Thermal reactors, then, raise p significantly by having regions of moderator where neutrons can lose energy efficiently to nuclei that have minimal capture cross-sections, and typically increase f by fuel enrichment.[2] This is not the whole story of reactor design, however.

The neutron multiplication factor can be expanded upon, as it is a function of energy:

$$\eta(E) = \frac{\nu(E)\Sigma_f(E)}{\Sigma_a(E)} \tag{1.1}$$

where $\nu(E)$ is the average number of neutrons produced per fission by a neutron of energy E, and Σ are macroscopic cross-sections, essentially weighted probabilities according to both microscopic cross-section σ and the number density of the isotopes constituting the components of the reactor. $\nu(E)$ increases linearly with incident energy for all fuel isotopes. As such, for thermal reactors η has an upper bound at 2.07 for ^{235}U and 2.14 ^{239}Pu, but

---

[2] Heavy water reactors, such as the CANDU, are so effective at moderating without loss by capture that they can forego enrichment altogether.

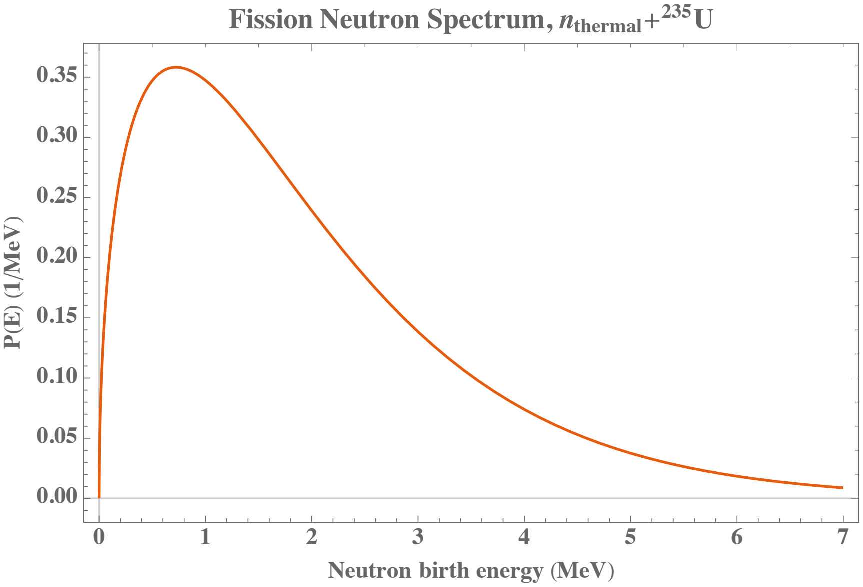

Figure 1.2: The spectrum of neutrons produced by the fission of a ^{235}U nucleus from a thermal neutron, as represented by the empirically-fit Watt spectrum. The peak is at 0.724 MeV, while the expectation energy is 1.98 MeV.

a significantly higher upper bound in both cases for fast reactors. In such cases converting fertile (non-fissile) ^{238}U in to fissile ^{2}39Pu becomes a very real possibility, even to the point of breeding: generating more fissile nuclei than were consumed in their production. In either case the quantity of fuel available for power consumption increases dramatically. This, in turn, has very real economic benefits: increased time between refueling, significantly greater employment of energy resources, and, in the case of the hypothetical traveling-wave reactor design, the ability to fuel a reactor for decades using an *in situ* breed-and-burn approach. To achieve these results, however, it is necessary to keep the neutron spectrum fast to both enable the $^{238}\mathrm{U} + \mathrm{n}^0 \longrightarrow {}^{239}\mathrm{U} \longrightarrow {}^{239}\mathrm{Np} + \beta^- \longrightarrow {}^{239}\mathrm{Pu} + \beta^-$ reaction and to keep η high enough that the loss of neutrons to capture is acceptable. Significant work has been done, and continues, to deploy and employ such fast reactors, but the tremendous energy of the neutrons, not taken up in the moderator, creates a significant challenge for the materials out of which such facilities might be built.

1.2 Defects and Radiation Damage in Materials

As discussed section 1.1 above, the radiation field in a nuclear reactor is prodigious. The neutron interaction with the materials, in particular, is the source of the majority of the damage. In order to assess radiation damage, however, it is necessary to have a reference—i.e. undamaged—material to serve as the basis. Forestalling a more thorough discussion

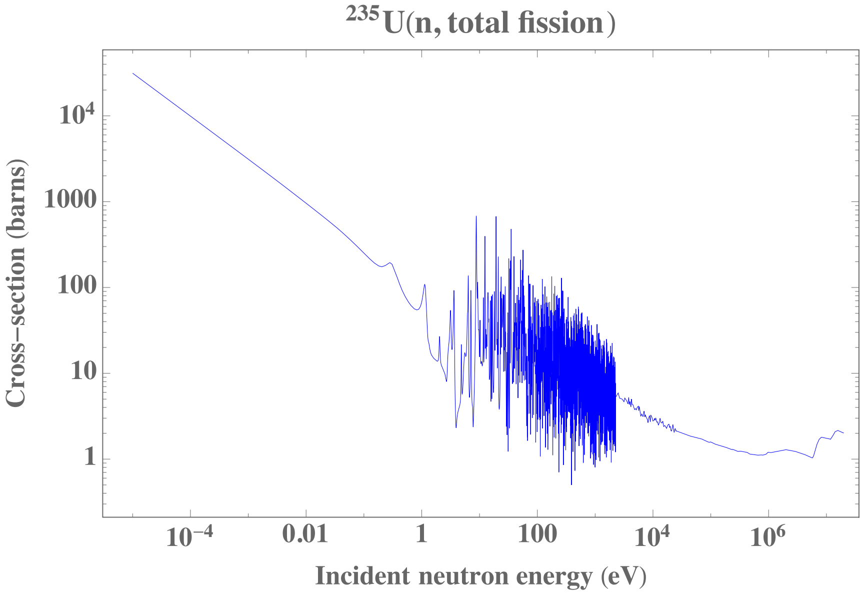

Figure 1.3: The total fission cross-section for ^{235}U, illustrating a significant increase as the neutron energy decreases. The jagged region starting at approximately 1 eV represents the resonances particular energies have in creating this reaction; this region is marked by a similar preponderance of capture rather than fission interactions and so thermal reactor design seeks to minimize the amount of time non-thermal neutrons spend in fuel rather than moderator.

of crystalline properties until sec. 2.1, it will be enough to assert the following: an ideal solid is made of a regular crystalline lattice, stretching to infinity in all directions and with every atom in is mathematically dictated postion. Real materials, on the other hand, have significant and sometimes frequent deviations. These can be classed by their dimensionality:

- Zero-dimensional:
    - Vacancies, when an atom is simply missing. The concentration of these defects is, in thermal equilibrium, wholly determined by the Boltzmann distribution ($\exp(-E_{vac}/kT)$), and insofar as the energy required to form such a defect is $\approx 1\,\mathrm{eV}$, are relatively common in all solids.
    - Substitutions, when an atomic site is occupied by the wrong type of atom; besides the dependence on the availability of the substituting material, the the energy of this depends on the degree of similarity in size, valance, crystal structure, and electronegativity between the original and substitutional atoms, in accordance with the Hume-Rothery rules.[65]
    - Interstitials, when an atom exists between lattice points. This can be either some kind of impurity dissolved in the lattice or a self-interstitial atom. The former case

generally occurs for small atoms (H, C, N, etc.) which can fit with relative ease into the spaces between larger atoms; a rule of thumb is that 0.59 times the larger atom diameter is the cutoff for interstitial solubility. Self-interstitials are naturally well above this limit, and require significant work to deform the lattice enough fit, on the order of 4 eV. At any temperature below the melting point of the material this amounts to a concentration of $\sim 10^{-70}$ per atom, or effectively zero, according to the Boltzmann distribution $\exp -H/kT$, where H is the enthalpy of formation [62]. Of importance to this work, however, self-interstitials can be formed by non-equilibrium processes.

  - Frenkel defects, the combination of a vacancy and interstitial defect
  - Schottky defect, an occurrence within ionic crystals where a cation and an anion are alike missing from the lattice in order to preserve local charge neutrality

- One-Dimensional Defects
  - Edge dislocations: these are misalignments of atomic planes with respect to their surroundings. An edge dislocation—an additional half-plane of atoms—is shown in fig. 1.4a, with an accompanying loop. Whereas this would be a closed loop in a perfect crystal, the additional half-plane necessitates an additional length, denoted the Burgers vector, to complete it. The edge dislocation itself is marked by the symbol $\perp$, and moves easily parallel to the Burgers vector, but cannot move perpendicular to it without vacancies or interstitials. Such behavior, climb, will be discussed in section 1.2.3.2.
  - Screw dislocations: these are shifts of atomic planes such that the burgers vector is perpendicular to the loop drawn around the dislocation, as shown in fig 1.4b. These dislocations are able to move more in any slip plane parallel to the burgers vector, and are consequently significantly more mobile than edge dislocations.
  - These linear defects appear as lines within the material, and can only terminate at surfaces. Lacking this, they form loops within the bulk. The two dislocations discussed above represent the pure forms; in practice, the vast majority of dislocations have a mixed character.

- Two-Dimensional Defects
  - Grain boundaries: two adjacent crystals, by definition, do not have lattices that overlap each other perfectly; rather, the degree of misorientation between them determines the frequency at which sites from both lattices overlap and bond the two together. High angle boundaries ($\theta > 10 - 15°$) are of particular interest, as they are more likely to have a relatively free volume within them, which serves as a place for solutes to collect—a point which will be of significance later.
  - Twin boundaries: occurring only in face-centered cubic (FCC) lattices, these are of little significance to the present work but are included for completeness. Briefly,

then, an FCC lattice is built up of layers of hexagonally-packed spheres which are in a permutation ABCABC. Should there be a location at which the permutation is flawed and gives rise to a permutation ABCAB**C**BACBA, the mirrored lattices created are referred to a twin.

  - Stacking faults: these come in two forms, intrinsic and extrinsic. In the case of extrinsic, a layer of atoms is missing from a limited region; in the case of the intrinsic, an extra layer exits. Again, this is a fault associated with FCC materials.

- Three-Dimensional Defects
  - Precipitates: these are volumes of some other material, or some other phase, from the matrix in which they find themselves embedded.
  - Voids: these are aggregations of vacancies, forming empty—that is to say, vacuum-filled—volumes within the bulk. They may dissipate back into the bulk as a result of thermodynamic processes.
  - Bubbles: very similar to voids, these regions have collected insoluble gasses and may have an impetus to grow. Unlike voids, they are stable and will not dissipate back into the bulk.

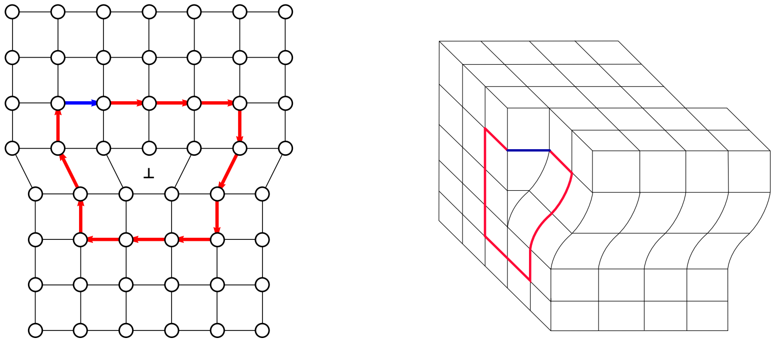

(a) (b)

Figure 1.4: (a) A depiction of an edge dislocation, marked by $\perp$ symbol, with the upright denoting the orientation of the added half-plane. The burgers vector, blue, denotes the extra step necessary to close the red loop, which would have already been closed in a perfect lattice. (b) A depiction of a screw dislocation. The burgers vector, blue, denotes the extra step necessary to close the red loop, induced by the shift of the planes.

These defects determine in large part the mechanical behavior of materials; e.g. it is the propagation of dislocations in material that allow for plastic deformations at forces several orders of magnitude lower than are predicted for a perfect crystal. Likewise, these defects can be created by and influence material response to radiation. In order to effectively engineer materials that can withstand the environment, significant work has been undertaken to understand these processes and interactions.

Likewise, the basic kinematic interactions of the neutrons with the material—not including nuclear reactions—are fundamental to all further understanding of damage in materials. Whether or not a neutron has an inelastic collision with a particle within a particular length is determined by the cross-section ($[L]^2$) of that particular interaction as a function of the isotope and particle energy, and the number density of those particles within a volume. Naturally, weighted averages of cross-sections are employed for mixtures. Assuming, however, that an in inelastic collision *does* occur, the interaction is a simple kinematic event, quite satisfactorily described by Newtonian mechanics. This leads to an energy transfer of $T = \frac{1}{2}\Lambda E_{m_1}(1 - \cos(\theta))$, where θ is the scattering angle in the center of mass frame and $\Lambda = \frac{4m_1m_2}{(m_1+m_2)^2}$. As the scattering angle is uniformly distributed in θ, the energy imparted in collisions across the system is well-modeled by expectation values.

An iron nucleus impacted by a fast neutron (energy $\approx 1\,\mathrm{MeV}$) will carry off, on average, approximately 68 keV. Displacing a nucleus from its lattice site does have a strong dependence on direction and material, but is generally on the order of tens of electron volts, so that the initially struck Fe nucleus—the primary knock-on atom, or PKA—has ample energy to create subsequent displacements, and so on down the line. This is known as a displacement cascade. Fig. 1.5 is a nominal calculation of such a cascade, showing the interstitials and vacancies in relative proximity to one another. Many of these do recombine, though not all, and give rise to long-term radiation damage, as will be discussed later.

Of particular importance is the assessment of the number of displacements so created as a function of the material available, measured in displacements per atom, or dpa. Experimentally measuring this is, owing to recombination and the practical indistinguishability of Fe nuclei, difficult; though some workers have conducted *in situ* measurements of displacement damage and damage rates in beamlines for materials diverse as, e.g., copper, aluminum, and sapphire [74, 40], assessments of dpa levels within a material are much more frequently based upon models. High in the ranks of such models by popularity is Kinchin-Pease (KP), which assume particular thresholds for displacement interactions and how many displacements can be caused at various energies. Before going into greater detail about this model, the most important consideration in its employment—or any other model—is to remain cognizant of the impressive degree to which dpa estimates can vary depending on the initial assumptions. In order to make creditable comparisons, then, it is imperative to be consistent in the assumptions underlying dpa calculations. [112, p. 385ff]

With that caveat in mind, the ubiquity of the KP model gives it claim to a greater description. Its key points:

- All collisions are of the hard-sphere elastic sort;
- Each neutron-nucleus displacement collision creates a primary knock-on atom (PKA) with energy E_{max};

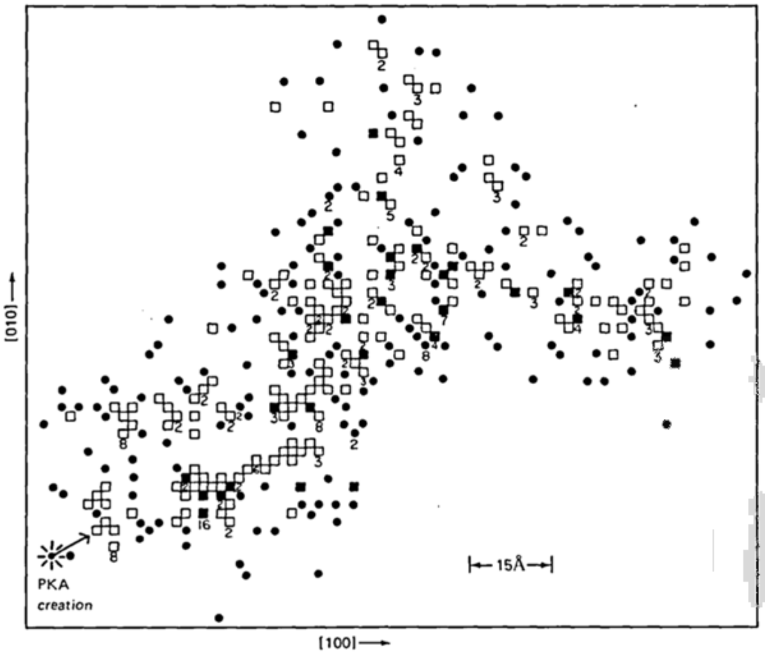

Figure 1.5: A displacement spike caused by a 20keV PKA in iron, from [112], after [25]. The numbers at various points indicate clusters of point defects otherwise unresolvable.

- There is a certain threshold energy E_d below which a displacement is not possible;
- Above a certain threshold energy E_c all PKA energy loss is via ionization;
- There is no vacancy-interstitial recombination;
- The crystal structure of the material is neglected.

Each PKA naturally goes about creating new displacements as long as it has energy above the E_d, and each of those may go on to create more displacements if they have received more than E_d themselves. Though the process is stochastic, the sheer number of collisions involved means that the average number of displacements caused by a given PKA is a good number to use, and this happens to be

$$N_d = T/2E_d, \ E_d < T < E_c, \tag{1.2}$$

where T is the kinetic energy of the PKA. In the case where $T > E_c$, eq. 1.2 simply has E_c inserted in place of T. The average amount of energy conveyed to the PKA from the neutron is, in turn,

$$T_{avg} = \frac{T_{max}}{2} = \frac{1}{2}\frac{4m_{\text{n}}M_{\text{PKA}}}{(m_{\text{n}}+M_{\text{PKA}})^2}E_n \tag{1.3}$$

where E_n is the neutron energy. The over-all behavior may be seen schematically in fig. 1.6.

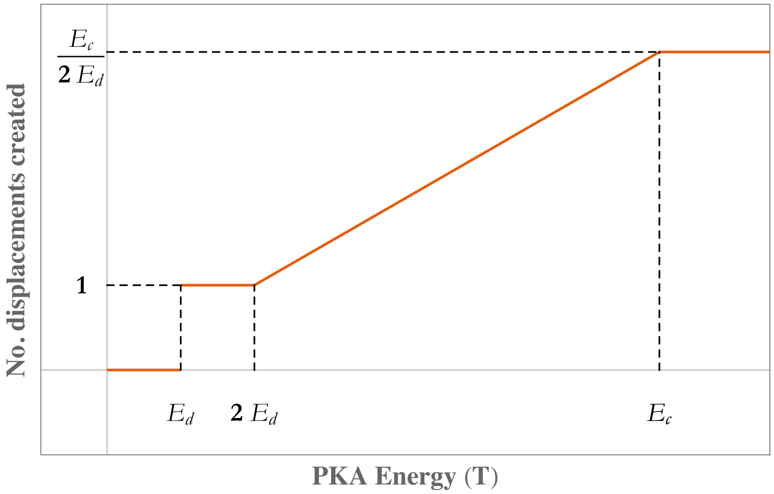

Figure 1.6: A schematic representation of the number of displacements caused by a KPA of energy T according to the Kinchin-Pease model. As one neutron should be expected to create many PKAs, this piecewise function must serve as a component of a sum (integral in the limit that neutron loses only an insignificant amount of its energy in a given collision) of successive energy loss interactions.

Denoting the function shown in fig. 1.6 as $d(T)$, and considering that the average energy of an incident neutron after the n^{th} collision[3] with one of the lattice atoms is

$$E_n = E_{\text{birth}} \left(1 - \frac{4A}{2(A+1)^2}\right)^n, \tag{1.4}$$

it follows that the total number of displacements predicted under the K-P model is

$$\text{displacements} = \sum_{n=0}^{\infty} d\left(E_{\text{birth}} \left(1 - \frac{4A}{2(A+1)^2}\right)^n\right). \tag{1.5}$$

The neutron and PKA interactions with the material give rise to a variety of different radiation damage behaviors, depending on regime: embrittlement, occurring for $T < 0.4T_m$ and greater than 0.1 dpa; irradiation creep, occurring generally above 10 dpa and below $0.45T_m$; radiation-induced or modified solute segregation and phase stability, occurring between $0.3T_m$ and $0.6T_m$, and for greater than 10 dpa; void swelling, for greater than 10 dpa and between $0.3T_m$ and $0.6T_m$; and high-temperature helium embrittlement, occurring at temperatures greater than half of the homologous temperature, and above 10 dpa.[141, 112] The following sections discuss each of these in turn.

---

[3] n may be allowed to go to ∞ rather than solving for the value at which it has thermalized since d(T) vanishes at E_d.

1.2.1 Hardening and Embrittlement

Embrittlement and hardening tend to be closely related. Insofar as a hardened material shows an increase in the yield strength and an over-all increase in resistance to plastic deformation, it frequently shows a decrease in the strain material failure occurs. This is, of course, a decrease in the ductility of the material. When plastic deformation has been hindered to the point where failure occurs suddenly and fracture propagates through the bulk, the material is wholly embrittled. One should not be surprised to see an increase in brittleness with an increase in hardness.

The primary cause of radiation hardening is the formation of nanometer-scale obstacles impeding dislocation motion. [110, 43] Self-interstitial atoms (SIA), in particular, are quite mobile within the lattice, having no restrictions on direction and a relatively low activation energy for movement, $\approx 0.25\,\text{eV}$. Clusters of SIAs, in turn, may move with an activation energy $< 0.1\,\text{eV}$. It also happens that an existing SIA can serve, in a sense, as a wedge, providing a favorable location for subsequent interstitials; a di-interstitial complex has a binding energy on the order of $1\,\text{eV}$.[62] It should come as no surprise, then, that interstitials can gather and form collections within the bulk material. These inhibit the flow of dislocations, and thereby inhibit extensive plastic flow by interrupting the glide planes upon which dislocations travel [41]

As it happens, these coalesced obstacles have been categorized and named [112]:

- Small vacancy clusters
- Dislocation loops
- Dislocation lines
- Cavities
- Precipitates

and of this list, dislocation loops have not been discussed in any foregoing section. They deserve increased explication. Foremost, these occur in a variety of styles, but a general depiction of the two major categories, vacancy and interstitial, may be seen in fig. 1.7. As they form, these loops are sessile and the dislocation lines can only move by climb. They can be unlocked by the interaction with other fault types—specifically, the Shockley dislocation—when the atoms of the loop register with the surrounding planes and the Burgers vector aligns with a slip system, at which point the defects can move quickly and easily. Until the temperature reaches about 800° C, however, these interactions are less likely. In the case of BCC materials this is especially pronounced, as clusters of impurities and defects combine to form barriers to dislocation motion more effective than either of those alone, and which is enhanced by the increased mobility of interstitials and impurities under irradiation. [112, 111]

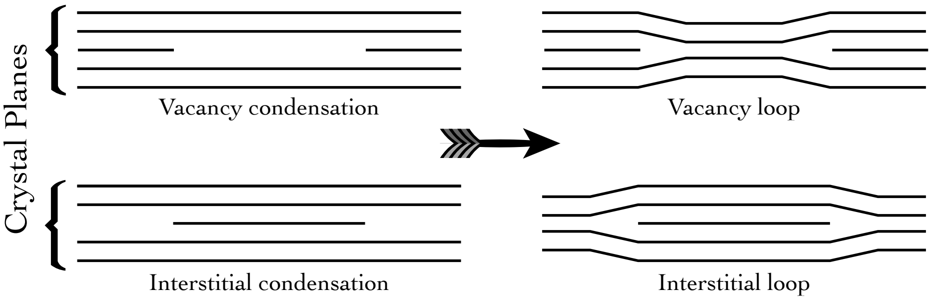

Figure 1.7: The process of loop formation, be it interstitial or vacancy, follows a general pattern: the point defects collect on a single atomic plane, expanding 2-dimensionally, eventually getting to the point where the surrounding planes collapse about them and form the bent geometries shown. Adapted from [112].

1.2.2 Swelling

Swelling is a net increase in the volume of the material as voids develop and the displaced matter moves toward the surface. Should swelling occur, the change in volume can result in tremendous stress within the swelling volume and in those structures restraining its motion. This can lead to buckling or rupture of structures. Were this in a cladding or other critical containment structure, the results would be, at least, significant and costly contamination.

For voids to develop, vacancies must be present in sufficient quantity and sufficiently mobile as to allow them to coalesce before annihilating at a grain boundary, surface, or self-interstitial. The latter criterion demands a certain amount of activation energy available to the system; void swelling is therefore observed at temperatures above $0.3T_m$. At the same time, voids can also evaporate by emitting vacancies; this dominates at high temperatures so that void swelling is not associated with temperatures above about $0.55T_m$ [112, p. 491].

The development of excess vacancies, as compared to interstitials, cannot occur solely from irradiation as the displacement reaction creates them in parity. Certain defect sinks, however, are biased toward interstitials and tend to remove them approximately 20% faster than vacancies [62], thereby generating an excess of the latter as irradiation progresses; dislocations are a prime example of such a sink. In any case, as the concentration of vacancies C_v grows with respect to the thermal equilibrium concentration of vacancies C_v^0, the chemical potential of a void made up of n vacancies

$$\mu_n = \frac{\partial G}{\partial \rho^0_{(n)}} \tag{1.6}$$

likewise changes. To achieve chemical equilibrium, this must be equal to the chemical potential of the reactants, viz. $n\mu_v = \mu_n$, and the total equilibrium of the system must also account fo the free energy of the surface that a void creates. Was ([134]) provides an excellent and considerably more detailed discussion of this and the preceding points, and the interested reader is referred to that text. Here it will suffice to skip to a critical result:

$$\Delta G_n^0 = -nkT \log \frac{C_v}{C_v^0} + (36\pi\Omega^2)^{1/3}\gamma n^{2/3}, \tag{1.7}$$

where Ω is the atomic volume. The relative growth of the positive and negative terms in this equation implies that there is a critical volume at which every additional vacancy added to the void will tend to push the change in Gibb's free energy more negative, leading to unrestrained void growth.

The presence of helium within the lattice, typically generated by (n, α) reactions within the material, is important for the development of void swelling. While the above work shows that a sufficient concentration of vacancies will be sufficient to precipitate stable voids, it also shows that below a certain critical size the vacancy will be more likely to evaporate vacancies back into the material lattice and thereby shrink. In a system in which helium is available, it will tend toward such vacancies and voids as it can find, it being insoluble in metals. Helium having precipitated, the change in Gibb's free energy to both remove a vacancy and reduce the volume in which He atoms may occupy is greater than removing a vacancy alone. Nor is this dependent on the pressure of the He within the void; the surface work and the PV work of the gas are not required to balance. The upshot is that even small amounts of helium will tend to stabilize voids, reducing the critical size. This substantially increases the void nucleation rate. [134]

It follows that any alloy composition that encourages helium formation will be more likely to experience void swelling. For example, 316 stainless steel, which can vary in nickel from 10 to 14 pct.[70], shows order of magnitude changes of swelling as the nickel content shifts from one end of the range to the other. [41, p. 400] An examination of the (n, α) cross-section for ^{59}Ni, and comparison to the orders of magnitude smaller cross-sections for other Ni and Fe isotopes,[32] strongly supports consideration of the material composition as a major factor in the occurrence of void swelling.

1.2.3 Creep

Creep, as the name suggests, is a slow, plastic deformation process. Following the initial displacement of an elastic loading, the strain will change from that predicted by Hooke's law to an elongation and even breaking, given enough time. This occurs in three phases, as indicated schematically in fig. 1.8. ϵ_0 represents the instantaneous strain imposed by the load when it is first applied. Region I of the figure represents a period of restructuring within the material, eventually crossing into the steady-state regime of region II. This region is defined by a balance between hardening and softening processes within the material, as Barrett *et al.* verified in the Fe-3Si system by demonstrating that the microstructure remained unchanged during steady-state creep. [23] Region III is marked by sufficient mechanical deformation to create mechanical instabilities, e.g. necking, which lead to localized strain increases and a feedback loop that leads to the behavior shown in the figure.

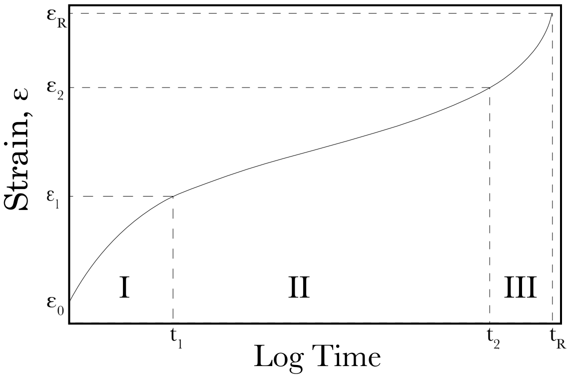

Figure 1.8: The phases of creep under constant load, separated by the (t_n, ϵ_n) pairs, up to the point of rupture at (t_R, ϵ_R).

For applications in which creep is a concern—those in which dimensional stability over a long period is required—the steady-state region dominates the deformation behavior. Great efforts have therefore gone into characterizing the functional dependencies of this behavior, and in general may be given as

$$\dot{\epsilon}_s = f(T, \sigma, \epsilon, m_1, m_2), \tag{1.8}$$

where T is the absolute temperature, σ is the applied stress, ϵ is the creep strain already existing, m_1 is a catch-all for the intrinsic material properties such as the lattice and moduli, and m_2 is a catch-all for the metallurgical factors such as grain size and processing history. So much for identifying the factors that go into $\dot{\epsilon}$—an engineer might, with some asperity, consider that there are more factors identified that do impact strain rate than do not. An identification of the functional form appropriate to each terms' contribution, and their relative strengths, is necessary for any progress to be made toward practical applications.[59]

The functional form of eq. 1.8, as it turns out, depends significantly on the mechanism being accessed by the variables. Fig. 1.9 shows an Ashby deformation mechanism map for pure silver, as an illustration of some of the mechanisms available. At low temperatures, the diffusion flow behavior dominates—this is not as strongly illustrated in silver, unfortunately, but experiments in nickel and maraging steel have shown diffusional flow creep at temperatures $0.2 - 0.3T_m$. The effect is of such significance that the normalized quantity $\dot{\epsilon}/D$ is approximately linear in σ (that is to say, $\dot{\epsilon}/D \overset{\sim}{\propto} \sigma$). In any case, self-diffusion, allowed by vacancies in the material, will be preferentially driven by the force applied as it creates potential imbalances. In the case of Coble creep, the vacancies proceed along grain boundaries, while in the Nabarro-Herring creep regime the vacancies travel through the grains themselves. It may be surmised that grain size has a prodigious effect on which of these mechanisms is preferable.

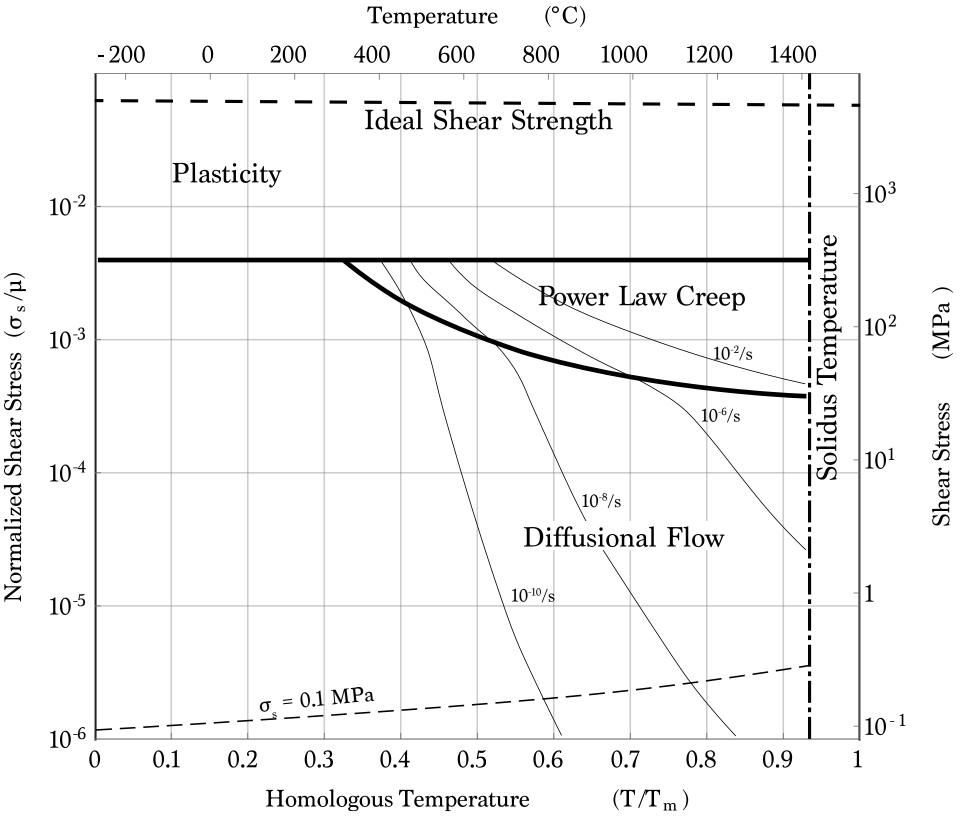

Figure 1.9: An Ashby deformation mechanism map for 50 μm grain-size 316SS, illustrating how creep mechanisms depend on external variables. Other materials may have significantly more complicated diagrams, with dependencies on strain rate or additional regions. Adapted from [46].

1.2.3.1 Thermal Creep

At high temperatures, greater than half the homologous temperature or so, dislocation-based creep mechanisms are activated. Edge dislocations move easily through an otherwise perfect crystal, but in this fallen world frequently come upon barriers to their motion. By emitting or accepting vacancies, however, edge dislocations can climb or descend to glide planes that are no-longer impeded by the blockage. Once there, the transition of the dislocation along the slip plane is rapid and the dislocation displaces to the next blockage, at which it is again arrested. This is depicted schematically in fig. 1.10. It may also be inferred that climb of the edge dislocation is the rate-limiting step. It is further worth observing that thermal creep will be impeded by the size of the impediment that the edge dislocation must climb around, and the average distance that a dislocation can travel before hitting the next impediment.

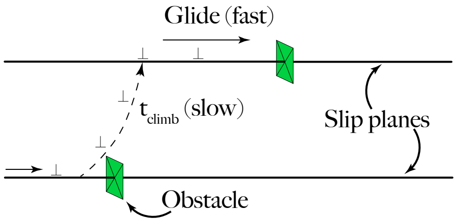

Figure 1.10: A cartoon depiction of the climb of an edge dislocation around an obstacle in order to access a glide plane which is locally unimpeded, and its motion along the new glide path to the next point of arrest.

1.2.3.2 Irradiation Creep

However, the mechanism of dislocation climb allows dislocations to pass barriers if enough vacancies and, to a lesser extent, interstitials are available to enable the process. This demands that the temperature be sufficient ($> 0.3T_m$) to allow for the creation and mobility of said vacancies, so that creep is generally understood to be a high-temperature phenomenon.

That said, irradiation has, as discussed above, the ability to produce significant numbers of vacancies and interstitials which can migrate to dislocations and enable climb if their absorption is not perfectly balanced. A number of mechanisms are acknowledged in this:

- Swelling-driven creep. By the development of voids, vacancies are prevented from participating in dislocation climb, leaving interstitials to do so.
- Stress-induced Preferred Absorption (SIPA) creep. A half-plane of atoms oriented perpendicular to the applied stress will show a preferential absorption of interstitials at its tip and grow in that direction, thereby wedging open the lattice. The natural explanation for this is that the applied stress (and commensurate strain) allows for a slightly easier fit than in other directions.
  - Preferred absorption glide (PAG). This is a process subsequent to SIPA, allowing dislocations to climb out of positions in which they are pinned. Fig. 1.11 shows edge climb by means of vacancy absorption; interstitial absorption is easily understood by the reverse of this process. In either case, the position of the edge dislocation proper has moved out of its original plane.
  - Experimental data suggests that SIPA and PAG are the primary mechanism for irradiation creep in the $\frac{d\epsilon}{dt}$ = const. region of creep behavior.

- Stress-induced Preferential Nucleation of Loops (SPIN) creep. This mechanism assumes an isotropic distribution of interstitials and vacancies to have been formed, and creates a potential function for a loop to form as a function of its orientation to a uniaxial stress applied to the body. As it happens, the potential is indeed biased toward forming interstitial loops perpendicular to the stress, and vacancy loops parallel to the stress.[134] In this respect, it is conceptually akin to SIPA creep, and may serve as a precursor to it. The degree to which SPIN creep accounts for observed irradiation creep behavior remains a matter of contention; it certainly cannot account for all of it, but may be a meaningful contributor.[97]

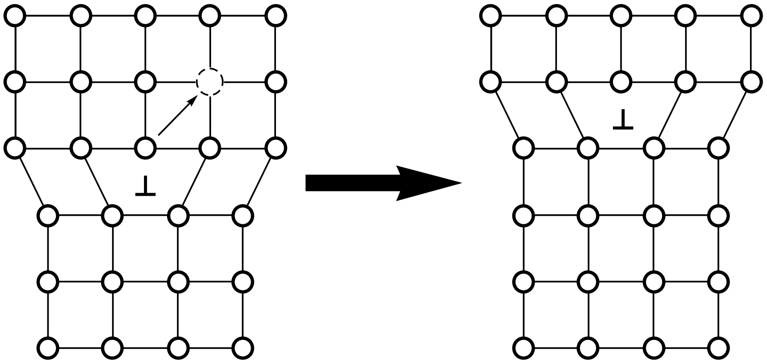

Figure 1.11: In this depiction of edge climb, the presence of a vacancy near the dislocation allows one of the atoms in the extra plane to move to the undisturbed bulk, thereby moving the edge dislocation up by one plane. The reverse process is also possible if a vacancy develops immediately below the edge dislocation and one of the surrounding lattice atoms moves in to fill the position.

As might be predicted from the dependence on vacancies, creep is an activation-determined process ($\propto \exp(-E/kT)$) when the defects are in thermal equilibrium. In irradiation creep, however, the presence of a neutron flux produces an excess of vacancies and interstitials that can dominate the rate at which the process occurs. [112, p. 499] At practical temperatures, radiation-produced interstitials dominate the thermal effects, so that strain rates in excess of $10^{-6}\,\mathrm{s}^{-1}$ have been observed when, absent radiation, thermal creep was negligible.[134]

1.3 The Basis for Radiation-Resistant Materials

Future reactors, especially developmental concepts employing harder neutron spectra for longer lifetimes, place stringent requirements on the materials out of which they're made. As may be inferred from the discussion in section 1.2, as long as there are fast neutrons, there will be radiation damage in a material. In principle, of course, reducing the elastic scattering cross section of the material would have salutary effects on the prevention of radiation damage, just as the removal of nickel was discussed sec. 1.2.2. It is also shown in fig. 1.12 that scattering cross-sections do have significant variation in the critical region between 1 MeV and thermalization (0.025eV), but all are above 1 barn. Aluminum does the best at 1.4±0.2 barns in this region, almost a factor of 8 better than ^{56}Fe. Nonetheless, other demands on the material, e.g. strength at working temperatures, take precedence. Iron can perform at the necessary temperatures, and for a reasonable price, while having acceptable neutronics properties.

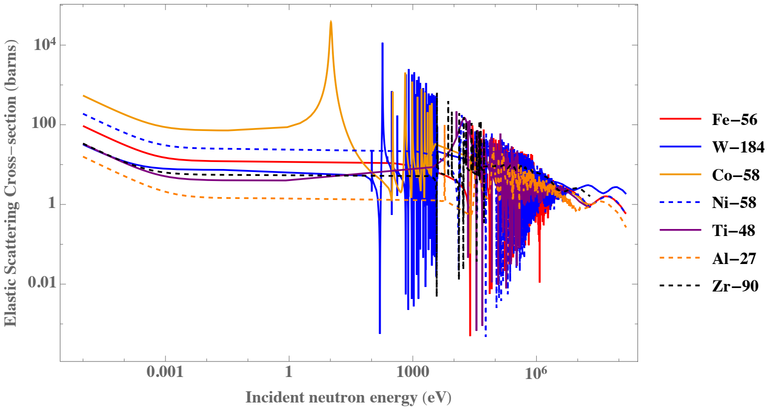

Figure 1.12: Scattering cross-sections as a function of energy for isotopes of commonly-used structural materials, some of their alloying elements, or those proposed for reactor use. Data is from ENDF/B-VII.1 [32], available at Brookhaven National Laboratory's National Nuclear Data Center portal.

The challenge is, therefore, to create a material that promotes damage repair (viz. interstitial-vacancy recombination), sequester it, or to lessen its relevance. Rate theory, as it pertains to the creation, motion, and destruction of vacancies, interstitials, and fission products provides a conceptually simple yet powerful framework for evaluating mechanisms by which damage can be mitigated. [108] It has been found, for instance, that minimizing the vacancy current within a material will generally decrease swelling; at the same time, increasing self- and solute-diffusion within the material can likewise reduce swelling, radiation enhanced diffusion, and radiation induced segregation of precipitates, by tending to push the material back toward its original equilibrium. The presence of defects ca, in turn, n increase the current of both vacancies and interstitials beyond what would be expected from purely diffusive calculations. This is defined by ratio $J = ZJ_0$, where J_0 is the diffusion only current and Z is known as the bias. [137]. The effect on vacancies and interstitials differ, however, so that there is a net bias appropriate to the material, $Z_{\text{int}}/Z_{\text{vac}} - 1$. Crystal structure also plays a role in the degree of net bias—FCC metals show a significantly greater net bias than BCC materials, about 50%. (*ibid*) This contributes to an imbalance of the two types of point defects, inimical to their meeting, annihilation, and local healing. Given all these considerations, it is gratifying, though not a great revelation, to observe that ferritic-martensitic steels have been found to be more favorable than austenitic steels. [109, 108]

Helium, more than other reaction products, provides a particularly important problem to mitigate. This is not to say that other inert gasses are more soluble within a lattice, as none of them particularly are, or that creation of impurities by transmutation might not ultimately create solid precipitates. That said, the nuclear reaction (n, α) has a vastly greater cross-section (probability) than any other transmutation reaction, particularly at lower neutron energies. It is also worth noting that no other noble gas can be formed by transmutation reaction other than by starting close (groups 1-2 or 16-17) and interacting appropriately, and elements in those groups are typically undesirable as alloying elements. As with other defects, sinks are important, but as helium bubbles are stable, further considerations obtain. Assuming spherical bubbles and an equal distribution of helium atoms in the bubbles produces the following expressions:

$$V_{\text{bubble}} = N_{\text{bubbles}} \frac{4}{3}\pi \left(\frac{N_{\text{He}}}{N_{\text{bubbles}}} \frac{3kT}{8\pi\gamma} \right)^{3/2} \tag{1.9}$$

$$= \frac{1}{\sqrt{N_{\text{bubbles}}}} \frac{4}{3}\pi \left(N_{\text{He}} \frac{3kT}{8\pi\gamma} \right)^{3/2} \tag{1.10}$$

$$\tag{1.11}$$

That is to say, increasing the number of bubbles within the bulk will tend to reduce the over-all swelling, albeit sub-linearly. It follows that providing sites for bubble nucleation will assist resistance to swelling and helium bubble embrittlement. Providing a satisfactory number of nucleation sites therefore becomes a significant priority for high-dpa materials.

Some work has pursued using fine-structured grains, with a commensurate grain boundary density, as a means for trapping bubbles; these are typically tempered martensitic steels (TMS) and there is evidence that they do resist swelling and other radiation damage effects [108]. It has been observed, however, that this approach, with its intrinsic reliance on grain boundaries as a defect sink, tends to create brittle fractures between the grains as voids and precipitates collect at them. [109, 129] For this reason, nucleation sites which are within the bulk provide a more attractive mechanism for providing robustness at high dpa.

Coherent precipitates, such as $Y_2Ti_2O_7$ nanoparticles within oxide dispersion strengthened steels [138], are an excellent basis for providing nucleation sites throughout a material. They can capture defects of either type, but cannot cause them to lose their identity; the defect can only wait to be annihilated by its opposite. While this behavior limits the number of defects that such precipitates can accept at one time, it does provide a fixed area for recombination.[112, p. 484]

Other forms of radiation damage can be also be mitigated by high precipitate densities. Consider creep, both thermal and irradiation-enhanced. In both cases dislocations climb around obstacles and so reach slip planes on which they are free to move with great speed. The over-all creep rate is given by the average distance a dislocation can move combined with the time it takes for the dislocation to get to a point at which it can move, the translation on the slip plane being essentially instantaneous on the timescales of interest. Assuming an isotropic distribution of cubic, coherent nanoparticles of edge length e, number density N, and material density ρ, the density of hardening material is $\rho e^3 N$, a constant. The mean-free path between dislocation arrests is $\sqrt[3]{1/N}$ and the average distance a dislocation will have to climb is $e/2$, at some velocity v which will be taken as a function of various factors: the temperature, the irradiation environment, the lattice constant, etc. Combining these factors gives the average dislocation velocity and its relationship to the distribution of a fixed amount of ODS hardening material:

$$
\begin{aligned}
v_{dis} &= \frac{2v}{e}\frac{1}{\sqrt[3]{N}} && (1.12)\\
dv_{dis} &= -\frac{2vde}{e^2N^{1/3}} - \frac{2vdN}{3eN^{4/3}} && (1.13)\\
0 &= \frac{3e^2\rho de}{N} - \frac{e^3\rho dN}{N^2} && (1.14)\\
0 &= \frac{3de}{e^2N^{1/3}} - \frac{dN}{eN^{4/3}} && (1.15)\\
dv_{dis} &= -\frac{8}{3}\frac{v}{eN^{4/3}}dN && (1.16)
\end{aligned}
$$

indicating that the dislocation velocity decreases as the number density increases, albeit with diminishing effect as the number increases. This is tantamount to asserting that alloys with large numbers of small particles within are preferable for creep resistance, hence the applicability of ODS alloys.

1.4 Oxide-Dispersion Strengthened Steels

The discussion of mechanisms by which radiation damage can be mitigated strongly suggest that oxide dispersion strengthened steel (ODS) alloys could be of employed as radiation-resistant material. These are, as the name suggests, steels in which small oxide particles, typically $Y_2Ti_2O_7$, are distributed in large numbers throughout the matrix. There is a further subset of ODS steels, known as nanostructured ferritic alloys (NFAs), which are an extreme case, in which the number density of the oxide particles is on the order of $10^{23}\,\mathrm{m}^{-3}$, with an average size of perhaps 1-5 nm in their major dimension [22]. Likewise, their ferritic structure is more suitable to restricting the development of precipitates and voids, as discussed above, and the absence of Ni (necessary to hold a high Cr steel in the austenitic phase) contributes significantly to a reduction in the amount of helium produced.

1.4.1 Powder Feedstock Manufacturing

The chief hinderance to the production of NFAs is the dissolution of the Y-Ti-O into the ferrite, from which it can precipitate into nanoparticles. This is a process that must be

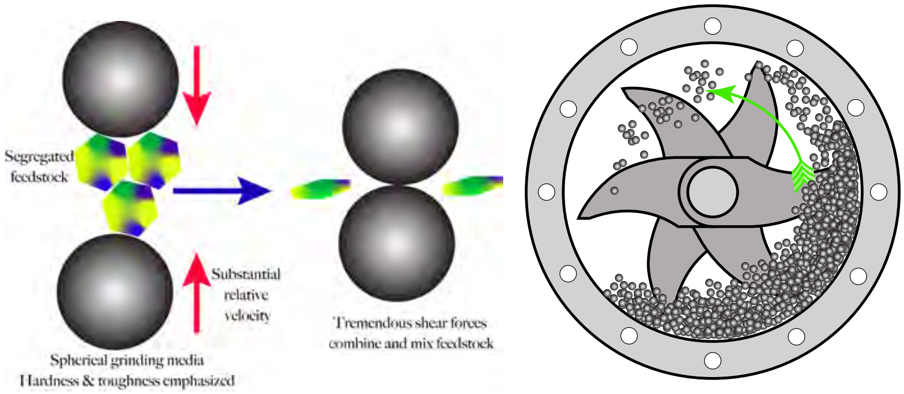

(a) (b)

Figure 1.13: a) Shows the basic principle of attritormilling, in which the grinding media smash and shear the product so as to merge and mix the components until the distribution is sufficiently homogenous as to be considered solvated. b) A depiction of a type of attritor-mill, in which a central agitator accelerates the grinding media to high speed to effect the process depicted in (a). The mechanism for accelerating the grinding media can be changed according to manufacturer, equipment availability, etc, so long as sufficient work can be done on the product. Images are original work.

conducted away from thermodynamic equilibrium. Most commonly, this is achieved by mechanical alloying—that is, repeatedly shearing Y_2O_3 and TiO_2 feed powders and mixing them into a ferrite bulk, to the point where they are not detectable by X-ray diffraction, having thoroughly dissolved into the iron. Subsequent heating will lead to the precipitation of nanoparticles, the size and distribution being significantly impacted by later heat treatment.[109, 10] Fig. 1.13 shows a typical milling apparatus and its mechanism of repeated compression and shearing. It must be remarked that details of the alloying process are only sporadically reported in papers which make use of the feedstock reported—whether or not the milling used an inert or reducing atmosphere, the ratio of grinding media to process material, duration, and milling speed being details that are included sometimes, but not unversally. This is unfortunate, as the quality of the feedstock and its surface characteristics appears to have a direct and substantial bearing on the quality of the final product.

A significant result in mechanically alloying materials is that they are typically maximally work-hardened and of an almost platelet-like morphology. This cannot be regarded as surprising, as the process in the attritor mill is one of repeated blows and shearing, but it does lead to certain difficulties for additive manufacturing, as will be discussed in section 1.5.2. For this reason, gas atomization has likewise been explored as a mechanism to create nanostructured 14YWT feedstock, and subsequently formed bodies.

This mechanism is depicted in fig. 1.14. A crucible of liquid metal, kept hot and under inert atmosphere or vacuum, is allowed to flow through at nozzle and become entrained

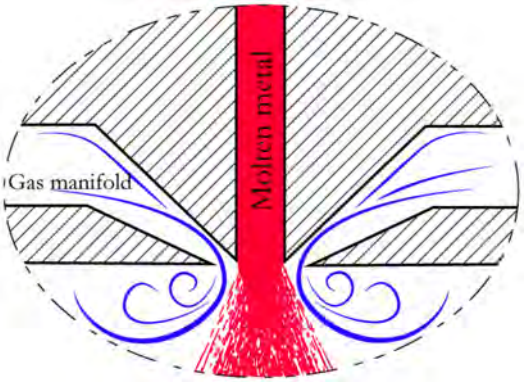

Figure 1.14: A depiction of a gas atomization apparatus of the "confined" form; the principle features of a hot metal reservoir and a stream of gas which breaks up the flow into micron-sized particles is universal to the process.

in a high velocity inert gas flow. This breaks up and agitates the original flow, creating a highly turbulent droplet spray into a collection chamber kept under vacuum. The extreme turbulence of the breakup provides mixing to homogenize the yttrium and titanium oxide within the material [119, 115, 51], while the high surface area and radiative cooling prevent premature resegregation of the oxides. The particles produced have a convenient spherical shape and are not work hardened in the slightest, factors which, again, are of significant interest to this work and will be addressed in section 1.5.2. Ominously, however, there is at least one report, [19] in which raw powder had been formed by gas atomization, and it was found necessary to perform additional mechanical alloying upon observation of Y-phase separation.

1.4.2 Consolidation

Suitable precursor powder having been formed, it must be formed into a body by some process. While the process most commonly explored up to the time of writing is hot extrusion, hot isostatic pressing (HIP) and hot spraying have also been considered [131, 9, 18, 123, 127, 120]. Various types of additive manufacturing have also been considered.

1.4.2.1 Hot Extrusion

Though different papers take varying approaches to hot extrusion, and to which aspects of the process they report, they do have definite commonalities. The existence of a feedstock powder being taken as a given, consideration of the hot extrusion process proper beings begins with the sealing of the powders into a canister. This vessel is typically a mild steel. This is followed by outgassing under heat and vacuum, which is where variations begin to set in. [9] employed 400° C for 2 hours, while [127] and [53] both employed 300° C for an unspecified time. [11] followed the processing recipe given in [55]—it incorporates the entire text of U.S. Patent 4,075,010 [45]—and provides no better bounds on the process than 926° C to 1205° C for the extrusion temperature and an extrusion ratio ranging from 3:1 "to 50:1 or higher." Interestingly, the patent does not mention outgassing of the sealed canister. [37] degassed at 400° C, again for an unstated duration. [132] outgassed for two hours at 400° C. [92] degassed at the same temperature, but for at least three hours.

Extrusion temperatures in the literature likewise lack a universal consensus on processing parameters. [37] employed 850° C on 14YWT, [10] employed 815° C, [127, 53] used 1100° C, [132] extruded at 1150° C. One study, [19] in its Process II, made use of two extrusions, first at 850° C and then at 815° C separated by a 1-hour, 1000° C anneal and a half-thickness reduction by hot cross-rolling. One study study, [60], in fact performed a comparison of hot extrusions at three temperatures, 850° C, 1000° C, and 1150° C; this will be explored in more detail below. [92] likewise employed 1150° C as its extrusion temperature, though it is notable that it included a hot forging process likewise at 1150° C. It is also important to note that various papers employ post-extrusion annealing processes of various temperatures, durations, and cooling rates. [127] reheated the bar to 1050° C for an hour before allowing it to cool in air; [132] performed a similar process save at 1100° C. [92] annealed for an hour at 1200° C.

The results from hot extrusion universally indicated the existence of strong grain textures and a grain structure of pronounced elongation in the extrusion direction. [127], working with alloy J05 (Fe-13.65 Cr-1.17 W - 0.30 Ti - 0.26 Y - 0.06 O - 0.05 C - 0.27 Si - 0.16 Ni - 0.33 Mn, wt.%), observed that the difference in tensile strength between the extrusion direction and those perpendicular to it was sufficient to identify the groups conclusively—the extrusion direction being significantly stronger. SEM images from that work, fig. 1.15, illustrate the defects within the material that significantly explain the lack of strength according to direction. The authors also observed that the only cracks found perpendicular to extrusion were in a brittle second phase material. In a similar vein, [53] explored the orientation-dependence of the Charpy impact test, showing that splitting requires significantly lower energy when the notch is parallel to the extrusion direction than in other cases, and that the fracture surface may have a distinct columnar morphology. An immediate analogy, though not employed by the original authors, is that of splitting wood along the grain. This immediately corroborates the observations of [127].

Nanocluster development in samples created with the hot extrusion process had reliable results. [127] reports a fine dispersion of nanoöxides, 2.3 nm mean size and $5 \times 10^{22}\,\mathrm{m}^{-3}$, though they also report that these were accompanied by substantially larger (100-200 nm) Ti-rich particles. [18] provides further material characterization of the samples produced in [19], and asserts that their multi-stage processing of extrusion, cold rolling, and extrusion produced nanoclusters of major dimension $2.8 \pm 0.7\,\mathrm{nm}$ and $4.3 \pm 0.7 \times 10^{23}\,\mathrm{m}^{-3}$. [60], with its three heat treatments, produced the following nanocharacteristics: 850° C, $2.63 \pm 0.56\,\mathrm{nm}$, $1.03 \pm 0.20 \times 10^{23}\,\mathrm{m}^{-3}$; 1000° C, $2.53 \pm 0.62\,\mathrm{nm}$, $1.25 \pm 0.25 \times 10^{23}\,\mathrm{m}^{-3}$; and 1150° C, $3.60 \pm 1.06\,\mathrm{nm}$, $0.77 \pm 0.34 \times 10^{23}\,\mathrm{m}^{-3}$. [132] presented TEM images of nanoclusters with the matrix, but did not provide a characterization of their average size or number density.

[124], analyzing material discussed in [92], found nanoöxide particles $3.5 \pm 0.7\,\mathrm{nm}$, average diameter, and approximately $1.3 \times 10^{23}\,\mathrm{m}^{-3}$.

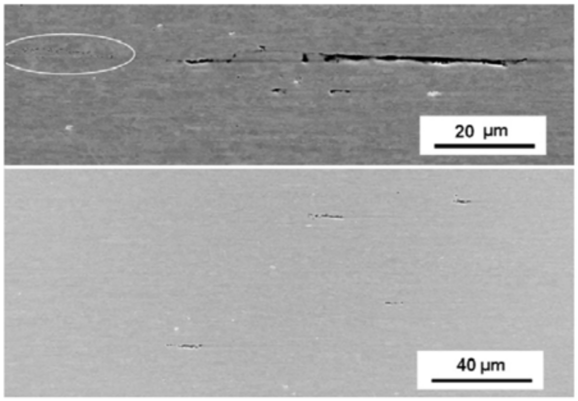

Figure 1.15: SEM images taken of a J05 creep test after 7200 hours at 650° C under 3500 MPa, with the extrusion direction aligned parallel to the scale bars. The original authors assert that the ellipse highlights a titanium-rich region of material, aligned to the extrusion direction, and apparently segregated. The cracks are regions of poor bonding between extruded layers. [127].

1.4.2.2 Hot Isostatic Pressing

Hot isostatic pressing (HIP) is a technique primarily focused on densifying bodies. As the name implies, uniform pressure helps to close pores within the material, while heat both increases the plasticity of the metal and improves the bonding between particles. Though this invites a comparison to sintering, though HIP temperatures may be 100° C — 200° C lower than the sintering temperature for comparable products. [57]

[115] HIP'd gas-atomized Fe-14Cr-2W-0.3Ti-0.2Y (nominal) powders formed by the novel—and tortuously named—Surface Treatment of gas Atomized powders followed by Reactive Synthesis (STARS) process, this latter ostensibly creates a Cr-Fe-oxide layer at the boundary of the powder particles, which then serves as the source of oxygen in precipitating nanoclusters following consolidation. The HIP itself occurred at $1220 - 1300°$ C, for between 1 and 4 hours, and between 120-140 MPa. Their results showed heterogeneously distributed nanoparticles in all cases. It is also noteworthy that their boundaries for acceptable nanoparticle sizes are on the large side: some of their higher densities were $1 \times 10^{22}\,\mathrm{m}^{-3}$ of particles below *50 nm*. (Emphasis added.) Insofar as most papers report significantly higher densities of particles smaller than 10nm, this is a questionable finding.

In a similar vein, de Castro *et al* [30] analyzed material produced by the procedure in [31]. Starting from ball milled (mechanically alloyed) powder, degassed for 10 hours at 350° C, before HIP consolidation for 2 hrs at 190MPa, 1100° C. The work also included a

750° C, 4 hour tempering step. In these works, the yttria-containing nanoclusters were bound at an upper size of 50 nm, and had local densities (that is, within test volumes typically $250 \times 250 \times 100\,\mathrm{nm}^{-3}$) ranging from wholly absent to $1.1 \times 10^{23}\,\mathrm{m}^{-3}$.

1.5 Additive Manufacturing

We may take it as axiomatic that manufacturing individual parts—that is, neglecting assembly operations—is a matter of putting particular materials into particular shapes. Doing so may involve subtracting material (e.g. milling, turning, engraving, etching), rearranging material (e.g. forging, stamping, injection molding), or adding material. This last forms the premise of additive manufacturing. In the reverse of chip removal during machining, small amounts of feedstock are added in a controlled fashion, layer by layer, to a body in order to reach a shape at or near final dimension. [5, 106]

It is important to emphasize that control—computer numerical control, in fact—is a major part of the definition of additive manufacturing (AM). To illustrate this point, consider a potter forming a coil pot out of clay. Clearly, it is built up by layers from raw material, but being done by hand limits the precision, repeatability, and throughput of the material. It is a cottage or artisanal craft, rather than a manufacturing process. Contrast this to NIST's research in extruded concrete [27], and the ability to employ machines to repeat a design with precision becomes a defining factor of an additive manufacturing process.

Additive manufacturing has advantages over the traditional extrusion or HIP process: it minimizes waste of feedstock by providing a body near to finished dimensions, the geometries available are significantly more complex than those achievable by extrusion, and likewise the dimensions of the finished part are not restricted by the need to maintain a volume of material at high temperature and pressure.,Additionally, it is suspected to avoid certain problems endemic to extrusion and pilgering, including the development of strong textures within the material.

1.5.0.1 Pyrodeposition

Though not a common technique, one study employed high-velocity oxy-fuel deposition. [19] That is to say, a spray technique in which the material to be deposited is entrained in and propelled by cone of flame. The material was deposited on an Al mandrel, which was subsequently etched away using phosphoric acid. Further machining was necessary to remove an intermetallic layer that the Fe and Al formed during deposition. The resulting piece was then left for 5h at 1000° C under vacuum to promote an oxygen exchange reaction and formation of Y-Ti-O clusters "within the coating." This tube was finally hot extruded to final dimension or close to, 4:1 area reduction at 815° C. In parallel, this work also explored a process (denoted no. 2) involving gas atomization and observed Y phase separation therein. To correct this, they resorted to ball milling to homogenize the chemistry: 40h in a Zoz attritor with additional FeO added. This was annealed for 1 hour at 850° C. The process

I (oxy-fuel) tubes showed a texture index approximately one-quarter of that shown by the process II tubes. The authors followed up with further characterization of these parts in [18]. Process I produced nanoclusters 7.2 ± 1.5nm in size, at $2.3 \pm 0.4 \times 10^{21}\,\mathrm{m}^{-3}$ concentration, while process II produced 2.8 ± 0.7nm nanoparticles, at $4.3 \pm 0.7 \times 10^{23}\,\mathrm{m}^{-3}$ concentration. They also, conveniently, performed some mechanical characterization, showing that the first process had $\sigma_y = 612 \pm 18$ MPa, and the second 1242 ± 39 MPa.

1.5.1 3D Printing

The term 3D printing is so broad and of such wide applicability that it might, in other works, stand in for the whole additive manufacturing title. That said, there are a few technologies commonly applied to metal manufacturing that must be discussed and dispensed with as alternatives to forming ODS alloy parts. For metal forming, the class referred to as powder bed fusion accounts for a majority of the manufacturing currently employed, [50] with direct feed of material (either in powder or wire form) exists as a viable alternative. In either case, once the feedstock delivery is handled, the metal powder consolidation may be achieved by a number of different techniques, depending on the heat source and temperature reached: direct metal laser sintering (DMLS), selective laser sintering (SLS), electron beam melting, and selective laser melting (SLM) [103]. A number of these methods have been explored for ODS alloy formation.

[136] employed laser melting in conjunction with a high (21.03%) Cr, 4.67% Al, ODS feedstock produced by sonication and aqueous mixing rather than mechanical alloying. The powder itself was deposited into the melt zone by a stream of inert gas for one of the processes explored, Laser Melt Deposition or LMD, and pre-existing for their SLM experiments. The LMD sample produced oxie partiles which were visible, if homogeneously distributed, on the scale of millimeters, suggesting that the results were less than satisfactory as to the presence and fineness of nanoparticles. Further, such LMD produced work showed no difference in Vicker's hardness attributable to oxide particles, which strongly suggests that the product is not a satisfactory nanostructured alloy. The SLM samples did not fare better. Similarly weak results for a TiAl alloy and SLM were displayed in [80]. The work of Kenel *et al*, which explored spark plasma sintering and laser melting, found, for their best material, nanoparticle dispersions of 29nm at $4.4 \times 10^{2}\,\mathrm{m}^{-3}$ [79]. While this did impart an improvement to the material with respect to a non-ODS variant, this number density is still orders of magnitude lower than those found in hot extrusion methods.

The work of Wang *et al.* ([133]) has proposed the laser-induced forward transfer (LIFT) method for the creation of submicron metal structures in direct competition with the processes discussed above which, owing to their material melting principle of operation, are not suitable to such fine work. This new process employs a multi-step process in order to form the individual layers:

1. A sacrificial material is laid down upon the surface to be augmented.

2. The sacrificial material is ablated to form, essentially, small molds, using a femtosecond laser. The authors promote the use of a patterning mask to create the mold pattern across the entire surface simultaneously, though individual applications may presumably decide whether the creation of such masks is the more time and material efficient mechanism.

3. The desired structural material is deposited, filling the ablated channels and covering the lands between them. The work in question employed an electrolytic solution, from which the desired structural material is precipitated by electric current as in a galvanic cell.

4. The surface is planed down (laser ablation in the original paper) to provide an even surface of structural and sacrificial material areas. At this point, the process may repeat from step one until the final thickness is achieved. After completing this loop, the remaining sacrificial material can be etched out of the body.

Such technology may strike the reader as familiar: it has similarities with some types of integrated circuit manufacturing [94], and on a much larger scale, has been in place for almost 200 years [58]. It could ostensibly be employed to create bulk ODS parts assuming one criterion could be met: the availability of a solvent simultaneously compatible with all the components of 14YWT and capable of precipitating them uniformly. This work is not particularly sanguine about finding such, particularly with respect to the oxide species involved, though it does speculate that perhaps Fe, Cr, W, Ti, and Y could be mutually solvated and precipitated, with the O necessary to form the Y-Ti-O structures diffused in during a later heat treatment step. Further discussion is, in any case, beyond the scope of this work.

From the foregoing, it may be concluded that the local high temperatures necessary for forming solid parts by 3D printing are indeed inimical to the formation of a fine nanoparticle dispersion in the bulk. The additional shear forces of other manufacturing processes (a factor touched upon in greater detail below) are apparently a critical component in avoiding high temperatures and retaining feedstock nanostructure.

1.5.2 Cold Spraying

Cold spraying is process that, historically, has been used for creating coatings on bodies of dissimilar materials or performing repairs on existing parts [68, 128, 33, 21, 125, 116]. Its ability to produce successive layers of material, however, suggest its application additive manufacturing process, and research to this end has been underway for some years [139, 20, 49, 114]. In particular, it may be applicable to the forming of ODS components [95, 89]. The process, only cold in the sense that the process employs temperatures well below the material's melting point, avoids the temperatures which are most conducive to the formation of large nanoparticles and so permits the retention of the fine particle structure which is the purpose and advantage of these steels.

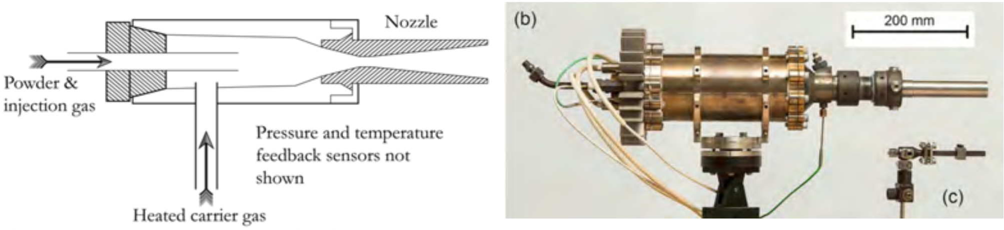

(a) (b)

Figure 1.16: (a) A cold spray nozzle assembly schematic (original work). (b) Cold spray nozzles realized: b, a commercial model from Helmut Schmidt University; (c) a simple home-brew system by Anatolii Papyrin.[13]

The mechanism of cold spray is thought to be primarily a function of adiabatic shear instabilities within the material. [121, 122, 16, 93, 14] That is to say, the tremendous forces brought about by the impact of the particle set up shear flow and corresponding plastic deformation, while most of the energy of impact (around 90%) is converted to heat. Such adiabatic heating and tremendous force causes both plastic strain and a prodigious strain rate at the interface between the existing layer layer and the impacting particle. This is depicted by the simulations shown in fig. 1.17a [16]. Such shear and heating can serve to break up oxide layers existing on the surface of the substrate and incident particles, while also bringing the respective lattices into close contact. This allows bonding to take place along the surfaces, as shown in 1.17b [13].

So much for the notional description of the cold spray process. It provides a diagnostic and some idea of the point at which the experimenter or process engineer aims, but does not greatly help in designing a process to get there. Successful cold spraying becomes, therefore, a matter of parameter selection. The simplicity of this statement belies the difficulty of the task: one review paper [15] lists some 67 factors that may go into modeling the cold spray process. Some of these are physical constants, and some are fixed by the material properties of the material to be sprayed (specific heat, density, melting point, etc.). This still leaves open to the researcher the average particle size, the nozzle geometry (thereby expansion ratio), the gas pressure, the choice of gas itself (implicitly selecting its density as a function of pressure, specific heat, etc.). Even aspects that a researcher might be inclined to neglect, such as thermal diffusion on the sub-microsecond scale, are actually relevant in such small particles, demanding their inclusion in all but the simplest computational models. [13] Perhaps the most important parameter of the process, however, is the hardness of the material. The more difficult to deform a material, the more challenging obtaining a suitable part becomes.

Under such circumstances, first-principles modeling is frequently abandoned in favor of parametric models and empirical formulae.[15] It is true that certain aspects, particularly the fluid dynamics and particle acceleration, can be modeled with existing fluid dynamics

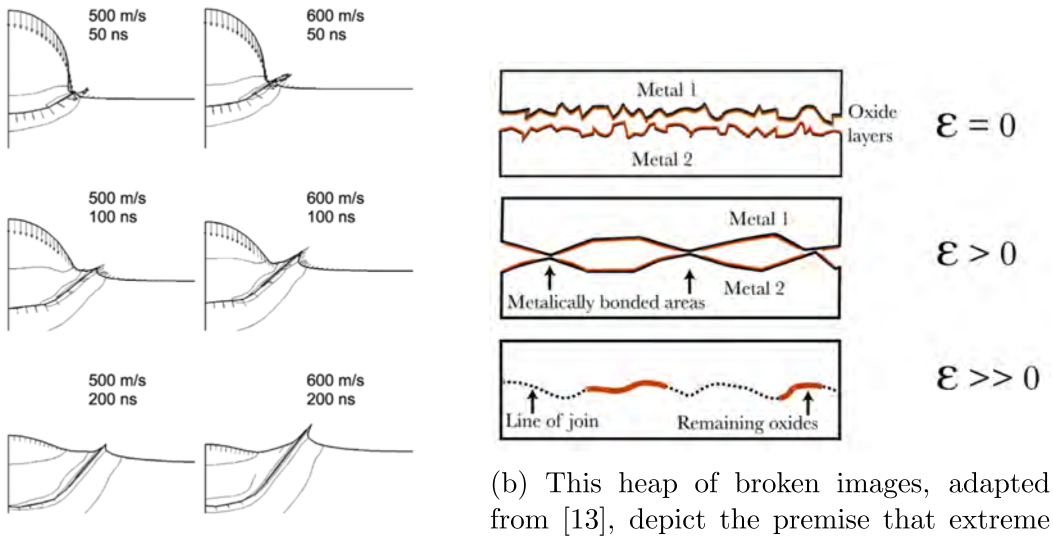

(a) This set of images, from [16], show a copper-on-copper impact at the two initial velocities indicated. The arrows shown are attached to individual nodes in the simulation grid and represent velocities, while the contours represent the temperature distribution.

(b) This heap of broken images, adapted from [13], depict the premise that extreme shear plastic deformation provides regions of metal-metal contact uninhibited by oxides, while retaining internal regions of oxide blockage. This will be of particular significance when examining the tensile test behavior of sprayed 14YWT samples.

Figure 1.17: Aspects of the cold spray impact and bonding process.

codes [122], which is fortunate. The most critical factor in determining the success or failure of the cold-spray process is the impact velocity. This has a lower bound, v_{crit} below which deposition does not occur, and an upper threshold, v_{errosion} above which the process is more akin to sand-blasting. [15, 121, 122, 13] [4]

This velocity window is dependent upon the material to be sprayed and the initial particle size. In general, melting temperature, specific heat, and hardness tend to correlate positively with v_{crit}; particle size, density, and carrier gas temperature negatively. [15] Further, of these can be tied to a sprayability condition presented by Assadi *et al*, ([13]) based on the thermal and kinetic energy of the impacting particle. This model assumes two reference numbers, E_k^0 and E_{th}^0, being the kinetic energy required to cause bonding for a particle without thermal energy, and the thermal energy required to bond without kinetic energy, respectively. The

---

[4] Ceramics are right out.

proposed relationship and bonding condition are thus:

$$\eta_E = \frac{1}{2E_k^0} v_p^2 + c_p(T_p - T_{ref}) \frac{1}{E_{th}^0} = \frac{E_k}{E_k^0} + \frac{E_{th}}{E_{th}^0} \tag{1.17}$$

$$\eta_E \geq 1 \tag{1.18}$$

The function captures the relationship between the impact velocity and, though it has evidently normalized out the particle mass (barring a misprint), the increase of particle size would cause an increase in the kinetic energy term independent of the velocity and thereby account for the noted negative correlation.

[26] explored the impact of different feedstock production routes on the final product: hydride de-hydride, plasma atomized, gas atomized. The authors measured the nanohardness of the particles as received, finding gas atomized production to be significantly softer than the other two options—3.91±0.19 GPa compared to 4.35±0.19 GPa (plasma) and 4.32±0.18 GPa (HDH). All of the coatings produced in this study had a porosity less than 3%, and could be taken to less than 1% given powder-specific spraying conditions. Particle velocity was found to be the most important factor for the quality of the sprayed surface. Their analysis of the strength of the material was limited by their coating testing procedure, which required an adhesive to bond the coating to a loading mechanism. The measurement therefore had an upper-bound to its range of applicability, 69MPa. None of the coatings produced broke with this maximum stress. One particularly interesting observation is that the final microstructure produced from the gas atomized powder depended distinctly on the degree of local strain, with the high-strain regions showing a region described as "featureless," that is, in which interesting microstructure is not visible at the magnification of the micrographs.

The generalization from forming a flat plate to more complex geometry is a matter of relative motions. While there are restrictions on the steepness of the angle achievable in cold spraying, which could provide a restriction on the tightest radius manufacturable, as a practical matter it is simply a matter of arranging the incoming stream to be always normal to the position on the mandrel. Work has already been performed to show the manufacturability of tubes by means of cold-spraying. Fig. 1.18 shows a particularly relevant depiction of how such tubes have been formed. [95, 89]

It also is appropriate to illustrate that cold spraying has been found to have promise in other areas of research, to support the idea that such advantages might be found for 14YWT. In the work done in [20], parts made of Inconel 718 were found to have fatigue properties that compare favorably to those found in wrought and cast parts. The cold-spray parts also had a homogenous structure and were found to retain the microstructure of the precursor material; their comparison process, selective laser melting (SLM) did not do so. Subsequent heat treatments did promote enhancement of both cohesion and ductility that the original paper characterized as "remarkable." This corresponds well to the work of [116], which explored test objects which were machined to have stress risers (simulated cracks or other defects needing repair) subsequently filled by cold spray (simulated repair). In particular, they used gas-atomized aluminum on an aluminum substrate. That set of

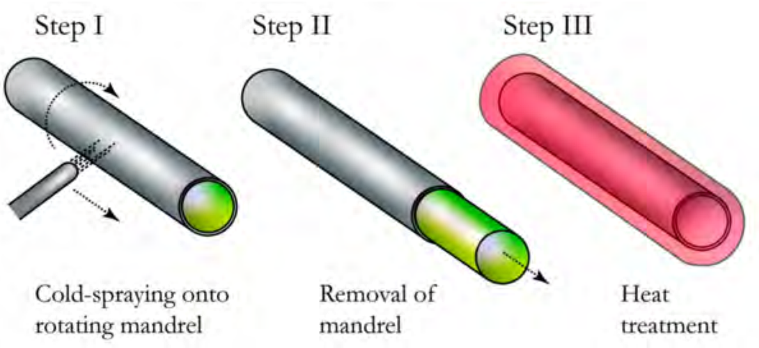

Figure 1.18: This shows the process by which cold-spray is combined with the relative motion of a mandrel to create more complicated bodies. This is a simple enough geometry, intended to create cladding tubes with a minimal number of steps; the generalization of the process is straightforward. Original graphic after [96].

experiments showed that the cold spray repair was effective annulling stress concentration and was not subject to delamination. Nor was the cold spray region ever the region of crack initiation, auguring well for the utility of the process.

Nonetheless, despite the potential for additive manufacturing applications in cold spray, the vast majority of literature currently available on the subject is primarily focused on its ability to form coatings or minor additions to more traditionally formed parts. This work, in part, seeks to remedy this, and to particularly to determine whether the properties of bulk 14YWT consolidated by the cold-spray process can be sufficient for employment in nuclear energy.

1.6 Statement of Research Hypothesis

This work proposes that cold-sprayed 14YWT is competitive with more traditionally consolidated 14YWT. This is to be evaluated with respect to a number of key properties:

- Grain Size and Distribution. Grain size, as discussed above, has a significant impact on both the hardness and the toughness of the material in question. The homogeneity of the grains, too, determines the degree to which behavior of the sample is also homogenous, or if there will be regions of differential behavior which could be detrimental to manufacturing, characterization, and qualification testing. What is most desirable will be a fully homogenized grain structure, as created by normalizing or annealing. Additionally, having large grains with high angles of joining, to better arrest cracks and prevent fracture, will be preferable to a fine-grained material.

- Grain Texture and Isotropy. Texture leads to anisotropy in material properties which can decrease the robustness of a system in unexpected ways and enhance the creep rate of the parts, as well as enhance paths by which cracks may propagate and enhance fracture.

- Hardness. While this is, broadly, negatively correlated with toughness, hardness is also a valuable trait for materials that are subjected to rubbing, material flow, and generally such mechanical action as would contribute to wear. Harder materials wear less, which is advantageous against fretting, erosion, and surface damage in general.
- Elastic Modulus. This directly relates to the material's deformability under load, and the degree to which it will undergo fatigue. For both dimensional stability and part lifetime under circumstances which may very well include vibration, a higher elastic modulus is preferable to a lower one.
- Yield Strength, Ultimate Tensile Strength. These two related properties are crucial to the viability of any material, for they are a direct measurement of how much load a given cross-section can handle or, conversely, how small a cross-section can be and still function to its intended purpose. Moreover, as the weight of a structure goes as its volume, and its strength as the square, the strength of a material can be a crucial distinction between a viable structure and one that simply will not work. The difference between the yield strength and the ultimate tensile strength is also important: it is a measure of the degree to which a material can fail gracefully, leaking before it breaks. Materials in which there is little or no difference between the two are brittle—ceramics, glass, etc—which, from direct experience, are known to fail catastrophically or not at all.
- Nanoparticle Size and Distribution. This is the *sine qua non* of ODS alloys. ODS parts produced by this process must be shown to possess nanoparticles of a size, number density, and uniformity throughout the body that is comparable with components formed by other mechanisms.

The discussion of each of these properties follows in the chapter Material Properties, while the experimental means for evaluating them is the subject of the chapter, naturally, Experimental Methods.

Chapter 2

Material Properties

As above, so below. — Hermes Trismegistus

While it is apparent that the utility of a particular material for a particular purpose is dependent on its material properties—nearly a tautology—which properties are most relevant to 14YWT and its processing are less so. More than that, what one expects from each property, and how it is expected to be impact the ultimate utility of the material in particular applications may not be immediately obvious, and brooks discussion. What follows is an enchiridion of the most important properties for 14YWT, and particularly how bulk properties are effected by the small scale nature.

2.1 Microstructure

As prefigured in section 1.2, all classical metals exist in periodic lattices. In the ideal conception, these are possessed of unbroken translational symmetry in all directions. It is in their imperfections, however, that materials achieve some of their most useful properties. In particular, the bulk is commonly found to be composed of individual small crystals, referred to as grains, which meet at grain boundaries. The size, shape, orientation, and interrelationships of these grains all have substantial effects on the over-all performance of the bulk which they comprise, manifesting in their hardness, yield strength, and fracture toughness behavior.

2.1.1 Yield Strength

The size of grains within a metal has a tremendous impact of their microstructure. As discussed in sec, 1.2, materials deform plastically by the movement of dislocations, and these dislocations have significant difficulty passing through high-angle grain-boundaries. The ratio of grain volume to grain boundary area is inversely proportional to the diameter of the grain; a direct consequence of this is that, in many cases, the yield strength σ_{ys} may be directly modeled $\sigma_{\mathrm{ys}} = \sigma_i + k_y d^{-1/2}$, where σ_i is the intrinsic resistance of the crystal to dislocation movement, k_y is the "locking parameter" which accounts for the difficulty of dislocations to pass the grain boundaries, and d is the average grain size. Consequently, finer grained materials are typically harder and stronger. [29]

The presence of secondary phases and their arrangement within the microstructure can also have significant effects on the strength of materials. Pearlite, spheroidite, and bainite are good examples, all being various arrangements of cementite (Fe_3C) in ferrite. In the case of pearlite, the microstructure is one of alternating layers of ferrite and cementite, strongly adhered to each other. Dislocations attempting to pass through the material are blocked at the phase boundaries, increasing hardness,. In complete contrast is spheroidite, in which the cementite is found in isolated inclusions embedded in the ferrite. This is the lowest yield strength that the steel can form for a given weight percent of carbon, as dislocations can avoid the harder carbide phase. Bainite, a micrograph of which is shown in fig. 2.1 has a lath structure with a finer carbide particle distribution in the ferrite than pearlite or spheroidite; they can be stronger than pearlite, but with greater ductility—a highly desirable combination. [29] An astute reader may observe that the improvement in bainite's materials, correlated with a finer hard-particle second phase, prefigures ODS alloy steels.

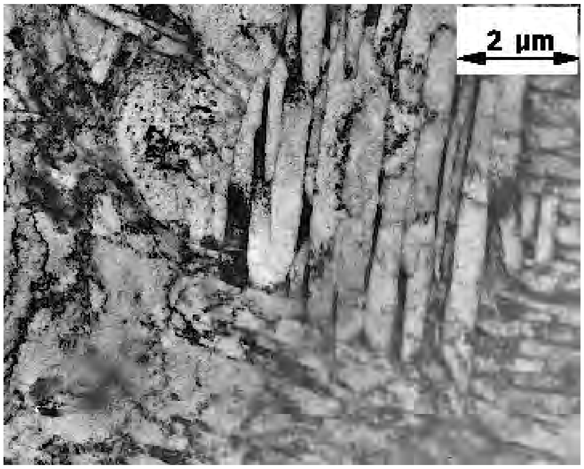

Figure 2.1: A TEM image of bainite from Oak Ridge National Laboratory illustrating the elongated, interlocking grains that contribute to its favorable material properties. [61]

2.1.2 Fracture Toughness

For applications in real-world environments, it is desirable that parts manufactured by cold spray demonstrate toughness against fracture. Such a part can deform plastically in such a way as to be detectable and reparable in the course of regular maintenance and operations, in line with the "leak-before-break" operating concept. [72, 69] Toughness can be understood

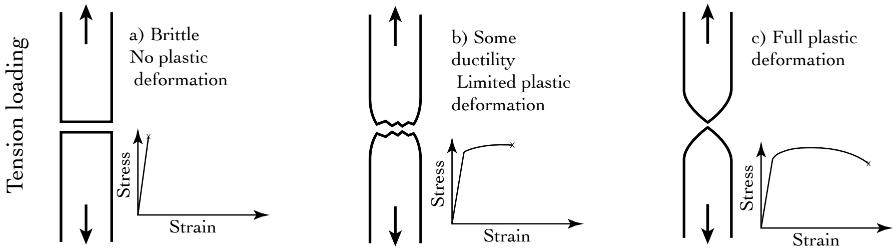

Figure 2.2: In the cartoon above, adapted from [29], relative degrees of plastic deformation are depicted along with notional engineering stress-strain curves illustrating the effect of increased ductility on its extent and, necessarily, the amount of work done to fracture the test piece.

as the amount of energy a material can absorb before it breaks. Phrased mathematically, as Callister does, it is the integral of the stress strain curve:

$$\frac{\text{energy}}{\text{volume}} = \int_0^{\epsilon_f} \sigma d\epsilon, \tag{2.1}$$

where ϵ_f is the strain at which the sample fractures. [59, 29] In this conception, the energy is absorbed in a plastically deformed region near the site of the fracture such that, for equal stresses, a greater amount of plastic deformation correlates to a greater degree of toughness. (viz. fig. 2.2). That said, while these general considerations are important for a conceptual grounding, many factors go into the toughness of a part, and the adage that a chain is only as strong as its weakest link is, in this context, nearly literal.

Starting at full scale, consider a crack somewhere in the part. Fig. 2.3 depicts idealized versions of such flaws in a uniform plate, subjected to a perpendicular stress σ. The radii of these ellipses at their tips are denoted ρ, and the semi-minor axis b. At the narrow ends of these cracks, the stress on the system is amplified by an amount related to its length and the radius of the crack. For the limit $a \gg \rho$, $a \gg b$—a very common configuration—in the idealized system defined, this amplification is $\sigma_{\text{max}} = 2\sigma\sqrt{a/\rho}$. It is apparent that, in the region near the tips of the crack, the local stress might very easily exceed the yield stress of a material. [29]

The premise of stress amplification near cracks within the material was expanded upon in the early 20th century: Griffith, Orowan, and Irwin (among others) analyzed the energetic relationships of strain release by crack opening, the expansion of the area of the crack with surface energy γ_s, and the work done in plastic deformation of the material near the tip, γ_p This led to a number of useful relations for predicting the stress under which a particular

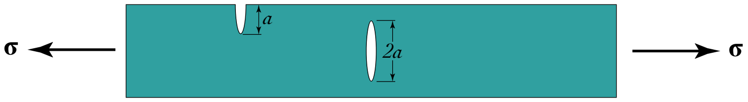

Figure 2.3: Idealized cracks of both surface and interior variety in a plate of material. For the purposes of analysis, the plate is assumed to be of constant thickness t and of infinite extent.

crack would fail, particularly

$$\sigma = \sqrt{\frac{2E\gamma_s}{\pi a}\left(1 + \frac{\gamma_p}{\gamma_s}\right)}, \tag{2.2}$$

$$K_{Ic} = Y\sigma\sqrt{\pi a}, \tag{2.3}$$

where E is the elastic modulus, Y is a dimensionless factor to account for particular crack geometries, and K_{Ic} is an empirical parameter known as the fracture toughness for a Mode I fracture. This latter refers to the sort of opening mode illustrated in fig. 2.3; there are two other modes, encompassing parallel sliding and tearing, respectively, but they are of little consequence in the vast majority of applications. [71, 102, 29, 59]

The theory of internal cracks and resulting fracture is of particular relevance to ODS alloy formation. The quality of the join between a particle and the substrate, ideally, will form a contiguous metallic bond, but if this should fail then then material may have an internal crack. FIg. 1.17b also suggests that oxide inclusions may block the formation of a contiguous metallic bond, with several possible outcomes. One possibility, should the oxides of the respective surfaces do not join, then they have promoted the formation of a crack between the two layers, and the above analysis obtains; another, if the oxides adhere and form a single oxide inclusion, a crack that encounters it may attempt to expand it and the lower γ_p in the oxide will enable the crack to propagate more quickly through. Neither case is particularly desirable.

Moving to smaller scales, grain size and morphology have an impact on the toughness of materials. Regarding size, it may be summarized that, for all microstructure types, a finer structure imparts a more fracture toughness. The theory of Cotterell and Petch makes this explicit:

$$\sigma_f \approx \frac{4G\gamma_m}{k_y}\sqrt{d} \tag{2.4}$$

where G is the shear modulus, γ_m is plastic deformation work done as the crack moves through the material, and d is the grain size. [59]

The grain morphology can give rise to further fracture toughness phenomena—particularly the manifestation of anisotropic behavior. Cracks may propagate along grain boundaries, or be arrested by them. A microstructure in which cracks cannot propagate tend to be In systems, such as extruded or forged materials, grains can demonstrate alignment and extension in the direction of material flow, resulting in mechanical fibering. Cracks running parallel to the fiber direction will find their progress enhanced, while those going transverse to the fibers will be more likely to arrest at a grain boundary. Forgings, in fact, take advantage of this: the alignment of their fibers parallel to the surfaces of the part so manufactured makes it more difficult for cracks to begin between grain boundaries or propagate along them, and toughens the material. This is not without its risk, however: should anisotropy fail to be taken into account and allowed to form a crack parallel, the phenomenon of lamellar tearing may arise, severely compromising the quality of the material. [59]

Temperature also has an effect on the fracture behavior of body-centered cubic (BCC(metals—the reader may recall that ferrite ($\alpha-$Fe) is of this class. Each slip system within the BCC crystal has an activation energy, corresponding to a temperature at which they can be activated. As the sample cools, fewer slip systems are available for the motion of dislocations, leading to a reduction of plasticity. This gives rise to the phenomenon of ductile to brittle transition, marked by the ductile-to-brittle transition temperature (DBTT). It has a logarithmic dependence on microstructure:

$$T_c = C^{-1} \log \Big(\frac{B k_s \sqrt{d}}{\beta G \gamma - k_y k_s} \Big), \tag{2.5}$$

where C and B are constants that have subsumed the temperature dependence of σ, and k_s is the locking factor divided by the Taylor orientation factor. For a more full derivation of this relationship, the reader is once again directed to consult Was' incomparably thorough text. [134]

2.1.3 Texture

Texture in materials is the degree to which grains within the bulk are oriented in the same direction. If all grains are randomly oriented, then the sample has no texture; if all grains are aligned, then the texture is strong. This has a direct impact on the mechanical properties of the bulk: textureless patterns give rise to isotropic material properties, while strong textures give rise to anisotropic properties, even in the case of cubic materials with high unit cell symmetry. The result of this is that the grain boundaries will tend to be low angle—that is to say, the mismatch between one grain orientation and the next is minimal, leading to a situation in which dislocations are more able to move through the system. As shown in fig. 2.4, the texture within extruded 14YWT is very strong; similar results from [78] show a slightly weaker but still noteworthy crystallographic texture.

The propagation of these defects correlates directly to the creep behavior of these materials. As discussed in sec. 1.2.3.2, creep is motivated by long-term, low stress movement of defects through a material. Depending on the microstructure and alignment of the grains, the dislocations enabling creep may proceed with greater or lesser difficulty. Grain boundaries provide one such impediment to motion and, as may be assumed, the lower the angle

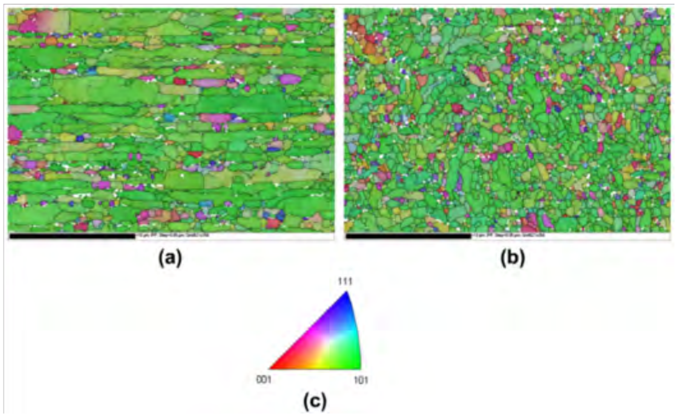

Figure 2.4: From [123], an EBSD (cf. sec. 3.2.1) image showing the remarkably aligned texture of hot-extruded 14YWT.

between two adjacent grains (closer the match) the less impeded the dislocations will be. [76] This corresponds well to observations that, in materials with strong texture, creep may be significantly enhanced anisotropically. [104, 6, 91]

2.2 Nanoparticle Distribution

The advantageous properties unique to ODS alloys are the result of the nanoparticles located within them. Their size and hardness provides a barrier to dislocation motion, increasing the over-all hardness of the material and increasing its creep strength, while their boundaries provide nucleation sites for helium bubbles. Intuitively, one might expect that dislocation motion would be hindered in some proportion to the frequency with which the particles are distributed; arguing by hydrodynamic analogy, one large barrier tends to create less drag than an equivalent area of small barriers, particularly if appropriately spaced. [126] gives an equation illustrative of this, in fact, $\tau = \alpha\mu b/L$, where τ is the yield stress, μ is the shear modulus, b is the magnitude of the burgers vector, and L is the mean spacing between the individual particles.

Likewise, while the ease of diffusion of vacancies, interstitials, and helium are all dependent on their physical properties within the bulk material, all will diffuse to a mean distance $\sqrt{D_x[T]t}$ in time t, or—reworking—travel to a nanoöxide site in time $\frac{d^2}{4D_x[T]}$.

For a given mass of oxide material and volume of final product (proportional density, that is), the number density of oxide particles is, naturally, inversely proportional to the volume of the particles themselves. In terms of the major dimensions usually employed in the literature to characterize nanoparticles, this amounts to a number density that increases inversely to the cube of the particle size. It follows that any effort to decrease the particle size will have a significant impact on the final number of nanoparticles within the material.

To achieve optimum distribution, it is therefore necessary to minimize the amount of growth that the particles can undergo. At the same time, a certain amount of heat treatment is necessary to remove the prodigious amount of cold work created by the impact and adiabatic sheer deformation process, and to help consolidate the particles into a working mass.

2.3 Hardness

Hardness is a principal factor in a material's wearing characteristics. Though the concept is generally well understood from day-to-day experience, it is well to be precise in our definitions from the outset, and state that it is a material's resistance to deformation under pressure. Some books, notably *Machinery's Handbook* specifically call hardness the ability of a material to resist penetration, which is likewise close. In any case, hardness contributes tremendously to the wear characteristics of the material in question. Indeed, one common and straightforward statement of the relationship between surface wear and the hardness of the softer of the two materials in contact is given by Archibald's formula,

$$Q = \frac{KW}{H} \tag{2.6}$$

where Q is the volume removed over distance traveled, K is knowns the wear coefficient, and H is the hardness. This description has, with reason, been characterized as crude, and is only weakly applicable to some classes of materials (e.g. polymers). [67, 66] Oberle proposed, in 1951, an alternative in the ratio of hardness to elastic modulus [107], which has been more recently adopted in a nanoindentation context as H/E_r and termed the plasticity index.[90, 42] In either characterization, it is the case that improved wear characteristics occur with increased hardness.

One point that may be raised: if the hardness is the result of a second phase, might not the softer matrix wear preferentially, undercutting the advantages that might be expected from a bulk hardness measurement? While this paper does not, and cannot, claim that such is impossible, with particular dependence on surface conditions, it has recently been found that incorporating hard, micro-scale particles has improved wear resistance in maraging steel.[77] The particles in that case were distributed on the scale of tens to hundreds of microns, with particle sizes on the order of 10 microns. A finer distribution of smaller particles must be that much more resistant to this concern, and so differential wear is not considered to be a significant concern.

Hardness testing is also a useful mechanism for assessing the presence of nanoclusters within the bulk: it has been observed that "there is an excellent correlation between the microhardness and the size and the volume fraction of the [nanoclusters (NCs)] or their spacing on a slip plane." [83] This leads to the conclusion that a material may be evaluated for the likelihood of the presence of such NCs by a simple and inexpensive nanoindentation test. If the sample is no harder than would be expected given a known absence of nanoparticles, then it is reasonable to conclude that the particles are themselves absent. Certainly, it is no replacement for TEM imaging in the full proof that nanoclusters exist within the material; however, as the property is so easily measured, such a diagnostic should be included in the analysis.

2.4 Elastic Moduli

An elastic modulus describes the reversable displacement of a body with respect to forces applied to it. The simplest variation of this, a purely linear response in a single dimension, is that of an ideal spring: $F = k\Delta x$, where F is the force applied to the spring, k is the constant of proportionality, and Δx is the change in length. This is a good start toward a description of material response to surface forces, particularly the linear response. Further development is required, however, as real forces are distributed over areas and all the dimensions of the body must be taken into account.

The first remark to address is that of the sufficiency of a linear equation to describe the response of the system. This is experimentally validated, but also comes from the generally small displacements seen in the elastic response of metals and other hard materials. Considering a body of arbitrary dimension, where each infinitesimal bit of matter dm (occupying, naturally, volume $\rho^{-1}dm$) is labeled by its initial position $\mathbf{x}$. For the body to elastically deform, some set of these points must be moved from their original, equilibrium positions according to a function $\xi(\mathbf{x})$, the displacement vector. This is not, however, quite satisfactory to describe a strained body: if all the points are deformed by a constant vector, the body has simply moved in space. Similarly, if two bits are displaced by an equal amount in the same direction, their strain in one direction should be equal, while the induced strain between them ought to vanish. These and similar considerations are handily answered by the gradient operation, so that the strain tensor is defined $\mathbb{S} = \nabla\xi$.[130] This definition of strain does differ from other definitions, notably [12], which would refer to $\mathbb{S}$ as the displacement gradient tensor, and define a number of different possible strains. Of the most relevance to this work, however, is the infinitesimal strain there defined as $\epsilon = \frac{1}{2}(\mathbb{S} + \mathbb{S}^{\intercal})$. As will be seen below, this is functionally equivalent $\mathbb{S}$. Moreover, in the elastic—linear— region, displacements are ideally small in accordance with the Taylor expansion of any response that the material might have, so that these definitions of the strain are satisfactory.

A full discussion of tensors, though extremely interesting and rewarding, is sadly beyond the scope of this text. Interested readers should consult Matthews and Walker (1965), Messiah (1962), or Blandford and Thorne (2018) for a more thorough introduction.[1] For the purposes of this work, it will be sufficient to remark that the dis tensor $\mathbb{S}_{ij}$ can be broken up into three components: its trace $\Theta = \mathbb{S}_{ii}$, its antisymmetric component $R_{ij} = \frac{1}{2}(S_{ij} - \mathbb{S} - ji)$, and its symmetric, trace-free component $\Sigma_{ij} = \frac{1}{2}(\mathbb{S}_{ij} + \mathbb{S}_{ij}) - \frac{1}{3}g_{ij}\mathbb{S}_{kk}$, where g_{ij} is the local metric tensor. As is customary, the Einstein summation convention has been employed. In any case, these correspond to basic constitutive relations within the body: Θ

---

[1] The present author admits to a certain fondness for Blandford and Thorne, and suggests that it should be considered as a cornerstone for any comprehensive physics education.

is an isotropically expansion or contraction; Σ is a shearing motion; and R is a rotation. A solid rotation, however, does not contribute to a strain, and so can be neglected; from a mathematics standpoint, $\epsilon = \frac{1}{2}(\mathbb{S} + \mathbb{S}^{\intercal})$ specifically subtracts out this rotation, leading to the functional equivalence alluded to above.

So much for the strain. Stress, too, turns out to be a second-rank tensor. Consider an arbitrary force acting on some surface, which will necessarily be of some extent and which can be described as a field called the traction: $\mathbf{t}(\mathbf{n}, \mathbf{x}, t)$, where $\mathbf{n}$ is the normal of the surface. For a body unaccelerated, all the forces so imposed must balance. It is possible to construct a system which allows for the decomposition of arbitrary vectors into their components and, indeed, culminates in Cauchy's law:

$$\mathbf{t}(\mathbf{n}, \mathbf{x}) = \sigma(\mathbf{x})\mathbf{n}, \quad t_i = \sigma_{ij} n_j \tag{2.7}$$

Fig. 2.5 shows the typical interpretation of these tensorial components as related to an arbitrarily small cube of matter. Furthermore, it is of particular importance to note that this definition allows evaluation at any surface, including one within a material, and at an arbitrary angle. The stress, and the traction between any two sections of material, is thus defined.

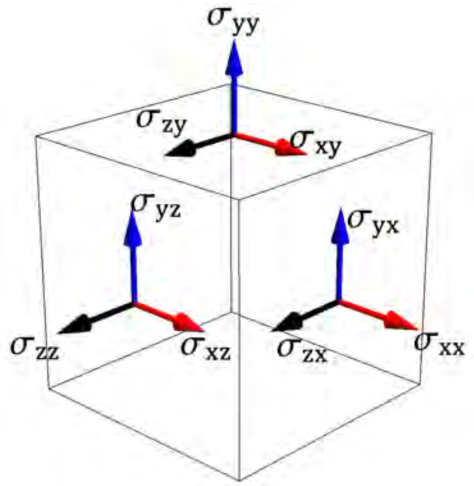

Figure 2.5: Behold the cube of forces on faces (original work). "If you want an image of the future, Winston, imagine a boot [applying a traction to a deformable surface]—forever." Apologies to Orwell.

Having established the ideas of stress and strain tensors, and having taken it as a postulate that one cannot exist without the other, there must be some functional relationship $f(\epsilon) = \sigma$. The discussion above about the employment of infinitesimal stresses at any given point further implies that a linear equation is appropriate for this construction, and so we get the most general description of a linear elastic system:

$$\sigma_{ij} = C_{ijkl}\epsilon_{kl} \tag{2.8}$$

As $\mathbb{C}$ is, by necessity, a fourth-rank tensor in $\mathbb{R}^3$, it has, in the most general possible case, $3^4 = 81$ independent terms. But, as so often happens in the physical sciences, symmetry comes to our aid. The stress tensor, as shown above, is symmetric, and this implies that the constitutive tensor $\mathbb{C}$ is symmetric in its first and second pairs of indices; likewise, it can be shown that the first and second pairs of indices themselves can be interchanged, so that there are, in the most general case, only 21 free variables. In the case of an isotropic material—which is generally a quite good description of a bulk metal in which the grain size is small compared to the length scale of interest, and randomly oriented—a there cannot be any dependence on direction, and the properties of interest should be scalars corresponding to the two irreducible tensorial parts. These are commonly the bulk modulus λ, corresponding to the uniform expansion or compression of the body, and the shear modulus μ, corresponding quite naturally to the shear deformation. As a practical matter, the bulk modulus is frequently transformed into the Young's modulus: $E = \mu(3\lambda + 2\mu)/(\lambda + \mu)$; this will be the more natural variable to employ in this work, but it does not represent any change of information content.

One direct consequence of a change in the modulus is the material's resistance to fatigue—that is, the build-up of defects by means of cyclic loading and deformation. One may model the number of cycles to failure N_f as $\Delta\epsilon = 3.5\epsilon_f N_t^{-0.12}$, where $\Delta\epsilon$ is the strain loading and ϵ_f is a fatigue strain parameter [41]. Recasting this in terms of the modulus and cyclic stress and solving for the number of fatigue cycles shows

$$N_f \approx \frac{34190}{\left(\frac{\Delta\sigma}{E\epsilon_f}\right)^{25/3}} \tag{2.9}$$

so that the number of cycles before fatigue failure increases dramatically as the modulus grows with respect to the load. It follows that for an element within a system, lifetime and reliability can be increased by increasing the moduli.

While it is a truism to state that the ideal value for a parameter is wholly dependent upon the application envisioned, should that application demand close adherence to design size under a wide variety of loads, that a higher elastic modulus would be superior. 14YWT is in the class of applications where significant deformation during handling or operation is detrimental, so that increased moduli are in its favor.

2.5 Yield and Ultimate Tensile Strength

Any material is elastic for a sufficiently small displacement. At some point, however, the elastic limit of the material may be exceeded and, assuming that it does not fracture, the body will be permanently, or plastically, deformed. This point is termed the yield stress, with corresponding yield strain. After plastic deformation has begun, the material continues to harden until it reaches a point known as the ultimate tensile strength. It is not the case, of course, that the work-hardening ceases or reverses after this point; it is, however, the case that the part has lost cross-sectional area so that the total force supportable is lessened. A typical stress-strain apparatus only measures force and displacement, giving rise to the apparent deviation as an assumed constant begins to vary significantly. An investigator sufficiently motivated, who had established a means of measuring both $A(x)$ and $F(x)$ could assemble what is known as the true stress-strain curve, but this work does not see a particular advantage to that course of action. The engineering stress-strain, depicted in a general way in fig. 2.6, shows directly the inflection point of the ultimate tensile strength, after which the system is mechanically unstable and will proceed directly to fracture.

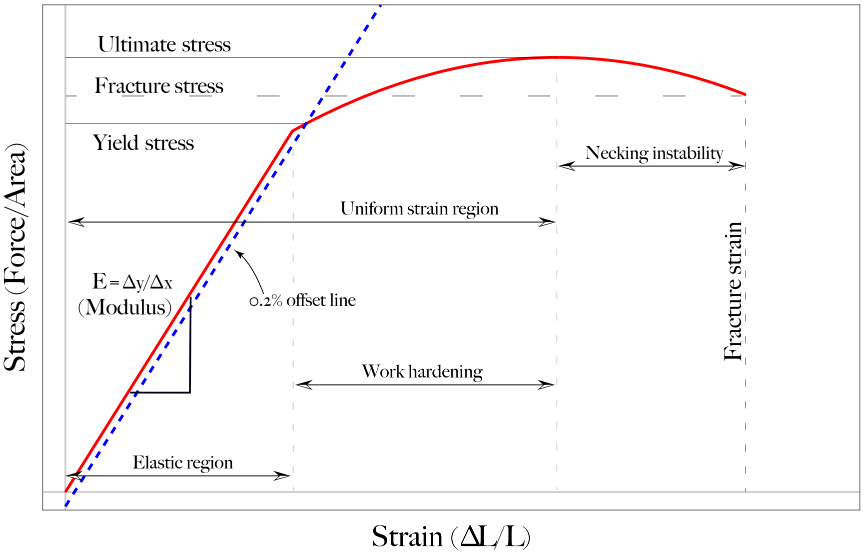

Figure 2.6: A schematic engineering stress-strain curve, showing the yield stress Y_S at the offset line (typically 0.2%, here significantly greater for legibility), and the ultimate tensile strength at the peak. Where the plot terminates, there the sample has finally fractured.

It is desirable to have a high yield stress in a material intended to support various loads, such as the 14YWT in this study: either less material will be necessary to achieve the requisite strength or, if the pitch and diameter of the fuel rods are fixed by other considerations, additional margin between the anticipated working load and the beginning of plastic deformation. Similarly, while it is ostensibly desirable to have a high ultimate tenslle strength, of greater significance is the difference beteen the yield strain and the ultimate tensile strain. In this region of the curve, noticeable changes the loading and dimensions of a part can occur without the immediate loss of all the force it had provided; failure can occur gracefully and with at a pace to allow for remedial actions. Brittle materials, on the other hand, will appear normal up until the point at which they fracture, leading to a total and abrupt loss of the structural properties involved, potentially leading to a catastrophic event.

Chapter 3

Experimental Methods

3.1 Sample Preparation

3.1.1 ODS Stock Formation and Cold-Spraying

The principles of gas atomization and cold-spray have been discussed in section 1.5.2. In practice, the author's collaborators at the University of Wisconsin-Madison performed the actual cold-spraying, as Berkeley is not equipped with the necessary apparatus, nor has plans to acquire it. The plates thus provided were typically prepared using gas atomized powders provided by Dr. D. Hoelzer of Oak Ridge National Laboratory, having contracted with ATI Powder Metals of Pittsburg, PA, USA for the actual production batch. The feedstock was nominally Fe-14Cr-3W-0.4Ti-0.2Y-0.25O nominal, [89] though a more thorough characterization was performed after the fact.

Spray was conducted with a commercial system, to wit a Cold Gas Technologies Kinetiks 400/34 unit, combined with a six-axis industrial robot. Substrates were commercially available 6061-T6 and 7075-T6 aluminum flat sheets, or 9.525 mm∅ (3/8”) rounds of 6061-T6 exclusively. The U. Wisconsin team performed a thorough parametric study of the cold spray parameters best suited to the laying down of these bodies, varying the ratio of N_2 to He in the flow and the temperature from 350°C to 750°C. The pressure most suited was found to be approximately 40 bar; this does not translate directly to an impact velocity, as the particle sizes produced in the gas atomization ranged generally 2μm to 10μm. but with some outliers not greater than 44μm.[89] Such variations in mass and drag are presumed to have had commensurate effects on the velocity achieved and the impact velocity of individual particles.

The first round of samples were left on their substrate prior to heat-treatment and machining. They were $350 - 400\,\mu$m thick atop 4130 steel. Chemical analysis showed that the particular composition was Fe-14Cr-3W-0.4Ti-0.2Y-0.25O. This was the only sample wherein the sample was allowed to remain atop the substrate through heat-treatment, as this was found to allow significant carbon diffusion from the substrate into the ODS; see sec. 4.3.1.3 for further discussion of this. Subsequent samples were made significantly thicker to allow for free-standing processing.

For second round of tensile tests, three plates were prepared of approximately 1mm thickness. One was left in an as-prepared state; the other two were vacuum heat treated at 800°C and 1100°C. The feedstock was found to be of composition Fe-14Cr-3.1W-0.39Ti-0.23Y-0.14O (wt.%).[87]

3.1.2 Vacuum heat treatment

In order to precipitate $Y_2Ti_2O_7$ and other yttrium-titanium-oxide species in the consolidated body, improve cohesion between the sprayed particles, and to remove cold-work induced by the adiabatic shear deformation during impact, it is necessary to heat treat the spray-formed bodies. In order to prevent excessive oxidation, and indeed the transformation of the part into its calx, it is necessary to perform the heat treatment in the absence of oxygen. This can be achieved either by the replacement of air by an inert working gas (frequently argon or an $Ar/5\%H_2$ mix), or by conducting the treatment under vacuum. In either case, the interior of the furnace itself could be maintained in an anoxic environment, or the material and atmosphere could be sealed within an air-tight capsule. This work employed both techniques: the former principally employed by the team producing samples at University of Wisconsin-Madison, whilst the sealed capsule technique was found at UC Berkeley.

Though early tests at Berkeley did seek to pull a hard vacuum on the tube furnace itself for processing, this was found to be unworkable early on in the project, for a number of reasons:

- The tube in the tube furnace was found to be of insufficient length to provide thermal isolation between the heated section and such vacuum fittings as would be necessary to attach a vacuum pump—with unfortunate results.
- As an alternative to pulling vacuum, continuous flow of $Ar/5\%$ H_2 was proposed but discarded as, at best, unsafe by the UC Berkeley Safety Office. Further considerations militating against it would have been the profligate use of gas and the potential for the hydrogen to remove necessary oxygen from the bulk.

After settling on using sealed capsules, initial work employed capsules with Swagelok fittings sealed in a glove box with inert gas fill and tantalum backup. Early thoughts that the capsules would be reusable were quickly discarded as the oxidation and galling created during the first heat treatments became apparent; a more cost-effective plan became necessary. Sealed glass capsules were known to the author and other researchers to be of great practical value in such cases, and apparently employed with frequency in the field, so this became a logical route to explore. Material selection, in this case, was trivial: only fused silica had a working temperature high enough to withstand the heat treatment temperatures employed. The nearest candidate would have been Vycor No. 7913, which may be used at 1300°C "intermittently," insufficient for a heat treatment of 2 hours or more, and not known to have significantly better working qualities than outright fuzed silica.[135]

Figure 3.1: One may see the length of fused silica tube held in the quick connect, which is in turn mounted in the vise. The length of the glass tube used was not precise, but generally about 60 cm was desirable; much longer became unwieldy, and much shorter, about 30 cm or so, the flame became uncomfortably close to the sealing gasket, the samples, and the worker's hand.

The process finally settled on employed fused silica capsules connected to a vacuum pump and gauge through an o-ring compression quick connect. This was connected to a 304SS manifold with Swagelok connectors, which were then attached to the vacuum pump by a flexible vacuum hose with appropriate hose-clamp fittings, a KF adapter, and KF fittings. Despite the number of different interchanges and areas for possible leakage, the system was capable of holding the system at pressures of $\approx 5 \times 10^{-3}$ torr. In addition, each tube was provided a a tantalum getter as insurance against trace gas remaining in the system or, as occurred a number of times, incontestable proof that the capsule had had a small leak in it and should therefore be rejected. The prospect of backfilling the capsules to achieve a similar effect was rejected out of concerns that a such a pressurized capsule could over-pressurize at temperature and not sufficiently superior to justify the risk.

Some practice was necessary to achieve consistent results with this technique. Only an oxyacetylene flame produced sufficient heat to work with fused silica, and had to be manipulated to get the material hot enough uniformly to flow, without causing a localized hotspot that could burst due to pressure imbalance. To create the capsules, a length of fused silica tube would first be heated locally and counter-rotated to form a twisted seal—not standard practice for forming rounded bottoms, but effective and minimizing the length of tubing requiring heating. Owing to the difficulty of keeping the glass at a satisfactory working temperature all the way around, this was considered to be an advantageous tradeoff. This end having been formed, the tube would be loaded with samples to be heat-treated, a tantalum strip, and attached to the vacuum manifold by means of a quick-connect fitting. The vacuum was then engaged, and typically achieved pressures in the vicinity of of 4×10^{-3} torr. The glass was then sealed by moving the torch about the fixed glass, as depicted in fig. 3.1. As work progressed, and experience increased, it became the practice to include a smaller fused silica tube within the larger, as the glass being pushed inward by atmospheric pressure would be stopped before bursting and ruining the vacuum seal.

3.1.3 Polishing

The quality of the sample surface can greatly impact the quality of the results of all the later steps. In the case of tensile or other tests, stress concentrations due to surface damage can reduce the assessed tensile strength of the material. Metallography and EBSD (see section 3.2.1) can be hindered, or even fully stymied, by poor surface preparation. Plastic deformation induced by surface preparation can influence micrstructural investigations; it is therefore important to minimize such deformation. Even in the case of micromachining for obtaining TEM lift-outs (see section 3.3.1), where the images are not needed for analysis, a good surface finish provides a significantly more convenient surface on which to work. For this reason, a great deal of this work hinged on the quality of the polish achieved on individual parts.

Sample mounting is frequently, though not universally, required in order to provide a satisfactory work-holding surface—this is especially true with small samples, powders, or specimens to be prepared on a thin section. One option, particularly suited to powders, was a two-part epoxy mixed and poured over samples, and allowed to cure at room temperature. Graphite was frequently added in order to improve conductivity when performing electron microscopy without negatively affecting the mechanical properties. At the same time, removal of samples from the epoxy, though enabled by means of specialized epoxy dissolver, was seen as highly undesirable, and therefore epoxy mounting was avoided when subsequent freedom from the mounting was predicted to be necessary. Mounting larger samples to polishing pucks by means of Crystalbond was preferable when precise thicknesses were required; the adhesive could be removed by heating and subsequent dissolution in acetone. And, of course, in some cases it was seen as unnecessary to mount specimens at all, as in the rings, which could be controlled when slid onto a close-fitting piece of rod stock, or with the SJ22 pieces, which could be managed by careful finger pressure.

Polishing itself proceeded by successive degrees of abrasive, with each step removing smaller cuts of material, as illustrated in figure 3.2. Some sources and industrial practice does not make a distinction between grinding and polishing, but a common delineation lies in whether the cutting abrasive is bound to some material or not: for grinding, the media is bound and can cut with greater force; for polishing, the media is more limited in the features it can remove. [34] In this work, grinding up to 1200 grit (equivalent to P4000 or 5 micron cuts) occurred with silicon carbide abrasive paper affixed to a rotating platen and with flowing water to cool and clear debris. Polishing beyond this occurred on felt polishing pads likewise attached to rotating platens, with diamond pastes of 3, 1, 0.5, and 0.1 micron particle size in succession with alcohol-based lubricants. Finer polishing was generally only required for EBSD, and employed a vibrational polisher with colloidal silica of 0.01 micron diameter; this would effectively remove any remaining damage near the crystal surface. Between all steps, and especially after use of the vibration polisher, thorough cleaning was required to prevent contamination of the next step down—an occurrence which would frequently leave an unacceptable gouge across the previously prepared surface.

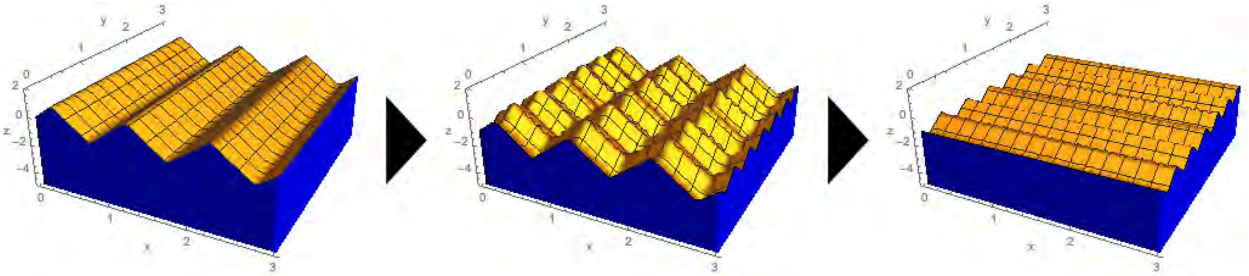

Figure 3.2: From left to right, a sample with a relatively rough surface finish—widely spaced, deep gouges—are cut over by smaller, more closely spaced gouges until the entire surface is closer to the average height, with a corresponding loss of material. This proceeds until the average deviation from the mean is acceptably small. The 90° turn between cuts is advantageous, as it shows clearly when the original pattern of cuts has been excised by the smaller.

3.2 Scanning Electron Microscopy

Scanning electron microscopy is an easily executed technique with great practical value, and has therefore been employed extensively in this work. In this type of electron microscopy, an electron probe is formed by means of magnetic lenses and rastered over the sample surface by means of deflection coils. This probe generates a spray of backscattered and secondary electrons, some of which find their way to a detector. This is typically an Everhart-Thornley detector, which is comprised of a Faraday cage for electron discrimination, a scintillator, a light-guide, and a photomultiplier tube to increase detector efficiency. The faraday cage is of particular importance: with a positive charge of 250V, the cage strongly attracts low-energy secondary electrons; with a -50V charge, it repels secondary electrons and becomes an effective backscattered electron detector. Some instruments provide a continuous range of potentials for the cage, allowing for a mixed-mode operation, but this has not been applied to the present work.

Of particular importance is the degree to which electron penetration depends on the orientation of the crystal lattice to the beam. Certain directions with the lattice are typically more open than others (fig. 3.3) so that an electron will penetrate deeper into the material when the beam is parallel to one of those directions. This phenomenon is known as channeling, and gives rise to contrast variation in the SEM, as secondary electrons have a limited ability to escape from a deeper region. With a satisfactorily polished sample—damaged surfaces tend to lack the regularity needed to give rise to channeling, and therefore inhibit the development of contrast—it is possible to perform metallography entirely by SEM.

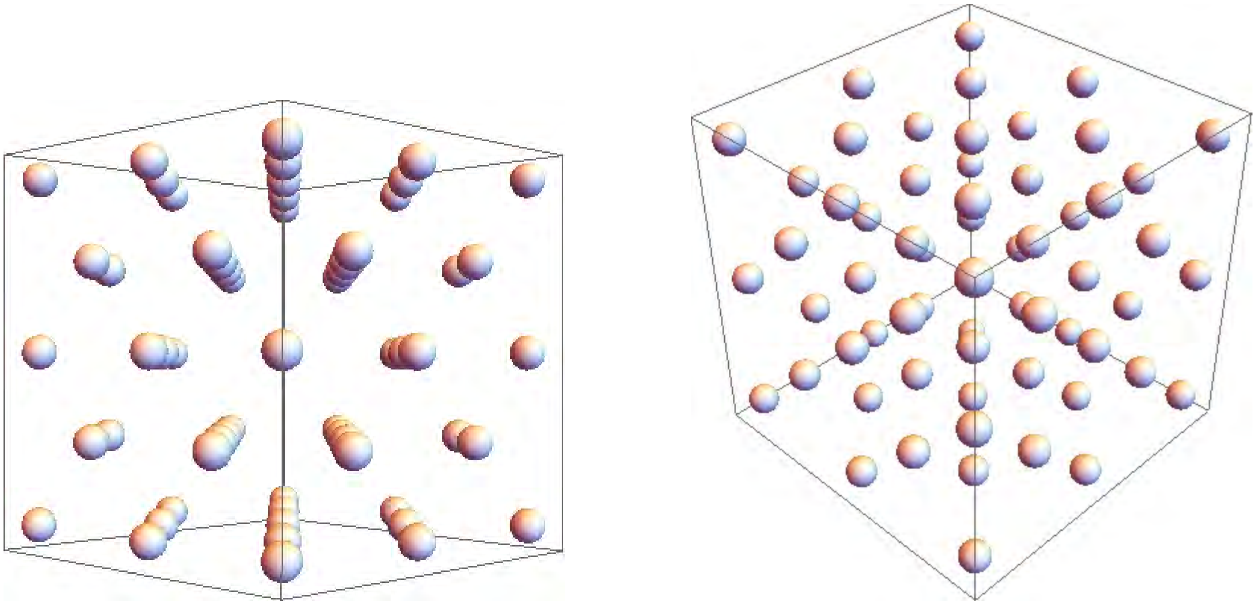

(a) Looking along [110].

(b) Looking along [111].

Figure 3.3: A Face-Centered Cubic lattice, made of eight unit cells, shown along two directions, to emphasize the difference in ease of travel along separate directions.

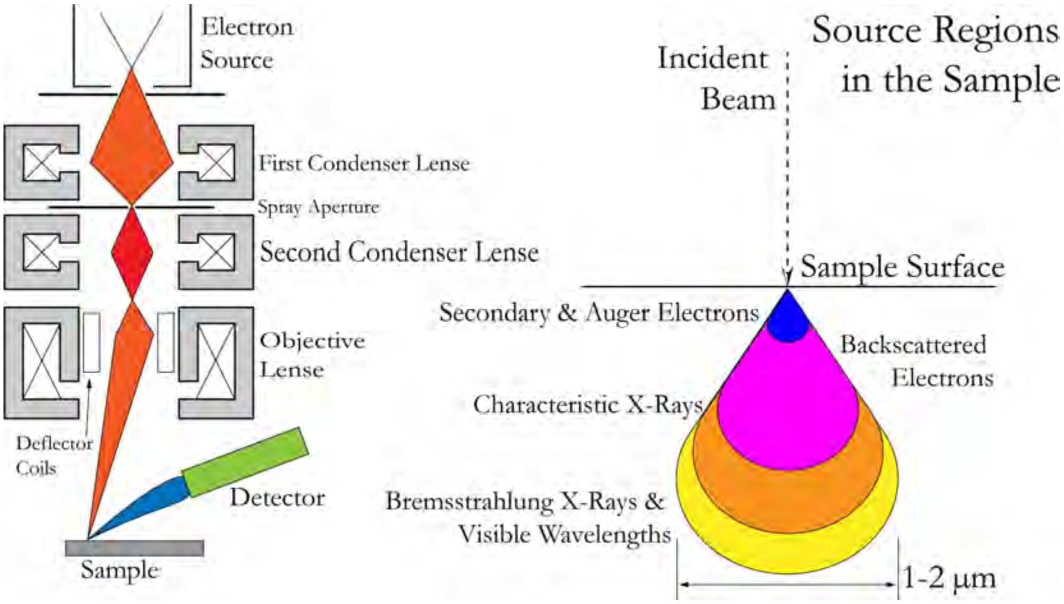

Figure 3.4: On the left, a schematic of the operation of an SEM; on the right, regions from which different signals originate with respect to the probe beam. Adapted from [48, 86].

3.2.1 Electron Backscatter Diffraction

Electron Backscatter Diffraction, henceforth EBSD, is an extremely useful tool in assessing crystal species and orientation at the surface of a specimen. Its origin lies in the scattering of electrons incident from the SEM beam, some of fraction of which may be modeled as isotropically distributed in space and direction. This amounts to a uniform source of illumination diffused throughout the sample, which undergoes Bragg diffraction according to the crystal lattice of the crystal it encounters immediately before exiting the surface. Owing to the preferential diffraction, each plane will scatter electrons from one portion of the incident wave to another, leading to a parallel line of bright and dark electron illumination on the sensing surface; the bands so formed are known as Kikuchi bands, and in principle exist for every scattering plane within the crystal, though as a practical matter low-order planes are significantly brighter and dominate the signal. Figure 3.5 depicts some of the bands that would be expected from an FCC crystal; the pattern seen at the detector is a projection of the surface of this sphere; these can be detected by the Hough transform, and the spacing between the bands measured, to determine lattice parameters and orientation of the crystal (up to symmetries) with respect to the detector. Thanks to the algorithmic nature of this operation, it can be done automatically, and allows for maps of crystal species and orientation to be built up over an entire surface.

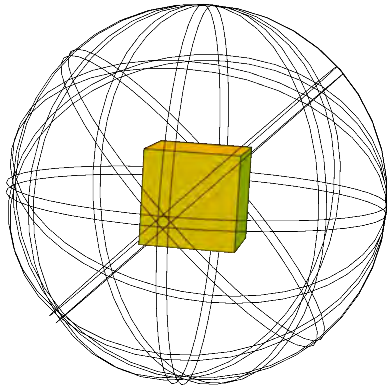

Figure 3.5: A cubic crystal with some of the Kikuchi lines it would generate projected on a nominal sphere around it. Shown are the $< 100 >$, $< 110 >$, and $< 111 >$ families. Image is author's work.

EBSD, though powerful, does have its limitations. The foremost is the demand for surface preparation: deviations from a perfect lattice naturally blunt the clarity of the lines; therefore, it is imperative to have as clean and gently-polished surface as possible. Similarly, no amount of fine polishing will suffice to create a surface capable of yielding EBSD data if the internal structure contains significant damage and disruption to crystallinity. Another significant hinderance to automatic indexing is from the limited number of test phases that can be incorporated as a practical matter. Phase identification hinges on the lattice constants derived from the spacing of the lines and angles, so that two species of the same crystal habit and relatively close lattice constants are indistinguishable by the instrument; it is necessary to limit the number of inputs according to the chemistry of the sample (assumed to be known by other means) and thermodynamics to minimize the chances for misidentification and to conduct efficient searches. And, finally, only phases of spatial extent equal to or greater than that of the scan resolution can be registered; though some EBSD systems claim resolution on the order of tens of nanometers, precipitates of nanometer scale will be missed.

The particular instrument employed for this work was an Oxford Instruments NordlysNano detector attached to an FEI Quanta SEM, with Oxford Instruments' provided AZtecHKL software controlling acquisition and solving for Kikuchi pattern. Geometrically, it was necessary to mount all samples in a 70° tilted stage in order for diffracted electrons to reach the detector face. The SEM was kept at 30keV for the scanning, with a beam current generally set at 11 or 16nA, depending on daily condition of the machine. This was found to provide consistently satisfactory signal given a well-polished surface and detector optimally placed near the surface.

EBSD's ability to distinguish grains by distinct patterns also gives it a capability to clearly delineate different grains. The Oxford Instruments software employs the ASTM E2627 standard for reporting grain size information. [117] This particular standard recommends that grains contain at least 100 points in order to be included, with 500 points per grain being considered a desirable average. The software itself demands at least 10 points to consider a grain reportable. Most important, though, is the calculation of the total area of a grain: for the number of points P in a particular grain and the step size Δ—that is, for the i^{th} grain, $A_i = P_i\Delta^2$ for a square pattern. An area factor is employed if a hexagonal tessellation is employed. [17]

3.3 Transmission Electron Microscopy

Transmission Electron Microscopy (TEM) is a powerful tool for quantifying the size and distribution of nano-oxide particles within a bulk matrix. While other techniques, powder X-ray diffraction for instance, are able to illustrate the presence of multiple material phases within a body and even their relative concentrations if the relative diffraction intensities of each species are accounted for, they are not able to identify where the material is located within the body, let alone the average particle size. Given that the size and distribution of the Y-Ti-O nano oxide particles is the most salient feature of the 14YWT alloy under consideration, it is necessary to effectively characterize them by such methods.

The intricacies of TEM can fill books, indeed careers, so that the following discussion does not pretend to completeness. With this caveat in place, it is a good starting place to consider a TEM as a microscope in which electrons have been exchanged for photons as the imaging particle. Following de Broglie's celebrated equation

$$\lambda = \frac{h}{p} \tag{3.1}$$

the greater the momentum, the smaller the wavelength of the imaging particle, which in turn directly proportional to the resolution of the instrument. An electron, with a non-zero rest mass, can achieve momenta—and thereby resolutions—ten times greater than a comparably energetic photon at 10 keV. And, while it is certainly possible to create X-rays of this energy, or even higher, creating suitably even illumination at that energy is difficult, and even should this be accomplished, such high-energy photons cannot be focused in the same way as visible wavelengths, preventing them from being used in an imaging system. Electrons, on the other hand, can be focused and refracted by magnetic lenses described by exactly the same thin lens equations used in classical optics.

Interactions of the electrons with the material give rise to diffracted electrons. This changes the local beam intensity and creates an image referred to as a diffraction contrast image. In a bright field image, wherein the illumination passes directly from the source to the imaging device, regions which have seen a stronger diffraction will be darker. Alternately, a dark field image may be created by selectively capturing those photons which were diffracted in a particular direction, allowing for significantly more discretion in the features to be imaged. This is particularly the principle behind the Selected Area Diffraction (SAD) technique, in which precise illumination and selection of diffraction spots can confirm that particular features are, in fact, associated with particular diffractions, while subsequent analysis of the diffractions so generated can lead to identification of a particular material phase [48].

The scattering processes that gives rise to diffraction also introduces phase differences in the electron beam. Using these as the basis for imaging gives rise to HRTEM, a technique capable of resolving individual atoms. Its extreme sensitivity, however, places greater obligations on the researcher. The specimen must be a weak phase object to introduce perturbations to the incident beam, but not overwhelm it. For some heavy (strongly scattering) nuclei, this can be on the order of tens of atoms. Further, the interference patterns generated are generally not directly interpretable: the information of the lattice is encoded in a phase contrast transfer function, which is the non-linear convolution of two phase-inducing functions, that of the objective lens and that of the sample. It is true that, under certain weak diffraction conditions, the Weak Phase Object Approximation holds and the resulting image may be directly interpreted, but this may fail for even a few layers of atoms of higher atomic numbers. [48, 100]

3.3.1 Focused Ion Beam Micromachining

Electron transparent samples are a prerequisite for TEM. These are, predictably, exceptionally thin and smooth samples. Demands for precision only increase for high-resolution TEM (HRTEM), desiring thicknesses of tens of nanometers. Such preparations are difficult, at best, to achieve by traditional polishing methods. Micromachining provides a significantly more reliable mechanism for sectioning and preparing TEM samples. By use of a focused ion beam—in this case, Ga^+—surface material can be selectively knocked out and a double-trench formed on either side of a prospective slab. By careful use of a micormanipulator needle (Omniprobe) and electron or ion activated organo-platinum gas as an adhesive, a sample may be lifted out and attached to a suitable support, typically a copper grid, at which point the manipulation needle is cut from the original sample. Thinning is a most delicate procedure, and proceeds from high to low energy ions in order to successively reduce the amount of surface disruption caused by the removal of material.

3.4 Nanoindentation

This technique measures the response of a material to displacement by an indenter, and from the plot of force against displacement, the hardness and reduced elastic modulus may be derived. These load curves are generally of the form shown in figure 3.8, with distinct portions of loading, hold at depth, and unloading. The unloading curve, in particular, may be analyzed by the method of Oliver and Pharr [113, 140], the equations of which are:

$$\frac{dP}{dh} = \frac{2}{\sqrt{\pi}} E_r \sqrt{A} \tag{3.2}$$

$$H = P_{\max}/A \tag{3.3}$$

$$\frac{1}{E_r} = \frac{1-\nu^2}{E} + \frac{1-\nu_i^2}{E_i}, \tag{3.4}$$

where E_r is the reduced modulus, E is the normal material modulus, E_i is the indenter modulus, ν represents the Poisson ratio for the respective material, and A the contact area between the indenter and the material. This last is ideally a function of depth h, wholly determined by the geometry of the Berkovich nanoindentation tip depicted in fig. 3.6, and matches that of Vickers indentation tip; in practice, there are slight divergences, particularly at small h due to unavoidable rounding of the tip, for which reason the establishment of a diamond area function (DAF) with a known standard is necessary. It is also advantageous to perform indentations significantly deeper than the region of tip rounding, so that its impact on the measured force is reduced to negligibility.

It is of importance to calculate A at h_c, the depth of actual contact. The motion of the indenter into the surface causes the material surrounding the indent to be deflected, giving the impression of a greater contact area than is actually the case, and depicted schematically in fig. 3.7. This generally takes the form $h_c = h_{\max} - \epsilon \frac{P_{\max}}{dP/dh}$. In the case of $\epsilon = 1$ this reduces to the x-intercept of the dashed tangent line shown in fig. 3.8, but in the case of a Berkovich tip $\epsilon = 0.75$ has been found to give superior results [44]. In the case of calculating hardness, however, the depth of contact at the maximum displacement, $h_{\max}$, is employed even though it may project contact area that is not actually touching. This methodology—which also

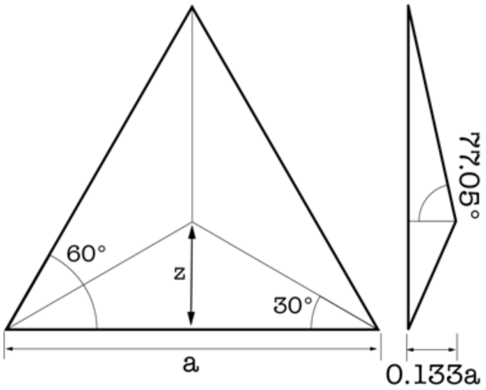

Figure 3.6: The geometry of a Berkovich tip. Angular dimensions from [84].

differs from the direct measurement of the indentation dimensions in the Vickers and other hardness tests—has been justified in this field by the potential of elastic deformation at the periphery being omitted by such measurements, and by its efficacy.

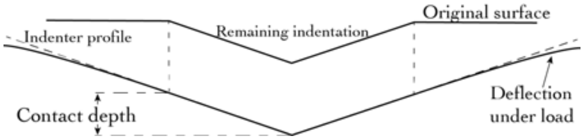

Figure 3.7: The material deflects around the indent. This must be accounted for in order to correctly calculate the indentation area. Original graphic after [113].

3.5 Tensile Testing

The importance of tensile strength having been established in 2.5, it was incumbent on this work to perform direct measurements of cold-sprayed samples. These were carried out on a Kammrath-Weiss GmbH Tensile Testing module, shown in 3.9. This robust mechanical frame provides various jaws for firmly affixing the test samples on the movable supports. One jaw is attached to the frame through a load cell which measures the tensile force in the test specimen, while the distance that the jaws have moved is read off from the number of turns of the driving screw. The ideal circumstance is that the test pieces are sufficiently well clamped into the module that any motion on the part of the jaws is a direct expression of the change in length of the test sample; this is not necessarily true, but can be compensated for without great difficulty. Similarly, the size of the paired lead screws is such that the deformation of the frame is, in principle, negligible compared to the deformation of the much smaller test sample; nonetheless, the compliance of the frame is a potential source of error that must be considered.

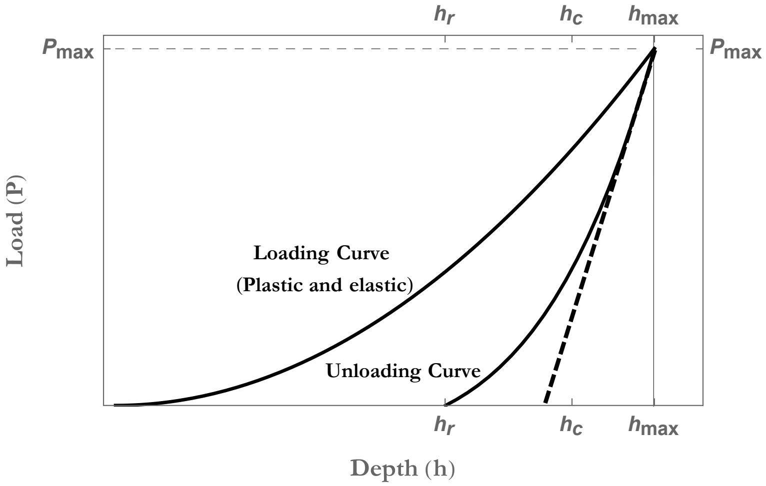

Figure 3.8: A nominal loading curve for a material showing combined plastic and elastic behavior. The thick dashed line, dP/dh, is the pure elastic behavior shown during the unloading phase, and so forms the basis for extracting the elastic modulus. Original graphic after [113, 84].

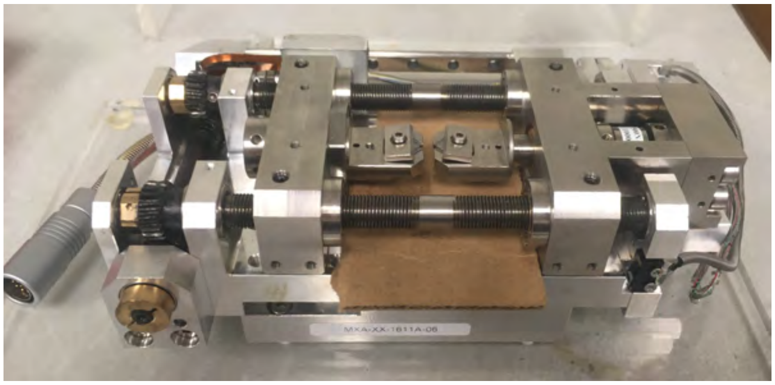

Figure 3.9: The Kammrath-Weiss Tensile/Compression Module at UC Berkeley.

The astute will have no doubt noticed that the observables the machine reports, displacement and force, are not transformable into the units of tensile strength without further information. Appropriate models of the tensile sample are necessary to identify the surface of maximum stress within the sample, and use the integral of that stress to obtain the force measured at the load cell. In the simplest cases, with high symmetry and uniformity, this is done easily enough, with a uniform stress throughout and a constant integral over the area. In cases with notches or holes, the force is borne by a reduced area, leading to stress concentrations, though these may still be simple enough to treat by focusing on the reduced area as the limiting factor; in the case of a ring tensile test, with interior support, a full analytic treatment has been performed in order to model the actual stresses and strains imparted within the system.

3.5.1 SSJ2 tensile tests

The title of this section refers to the particular geometry of the tensile specimen, illustrated in fig. 3.10. Pulling forces are applied on the curved surfaces and by clamping on the wide sections at either end, leading to a uniaxial stress field in the middle section of the bar. This is the weakest section and where it is expected to deform and eventually break. This stress, σ_{xx}, automatically satisfies the intuitive traction-free boundary condition in this region as $\boldsymbol{n} \cdot \hat{x} = 0$, and the total force is simply the product of the cross-sectional area of the bar and the stress. Such a test is relatively easy to perform, but care must still be taken to align the jaws of the tensile rig correctly, to prevent the inducement of shear forces in the system. Moreover, imperfections in the surface can serve as stress risers in the system and lead to lower yield and ultimate tensile strength values than would be warranted in an ideal system. Sample preparation and polishing are therefore of significance in the conduct of these experiments.

3.5.2 Ring tensile tests

Given the geometry of the specimens, calculating the stresses at the yield point was not assumed to be a simple matter of dividing the force by the total cross-sectional area of the ring $((\varnothing_{\text{outer}} - \varnothing_{\text{outer}}) \times thickness)$, as was the case in 3.5.1, though this was calculated to serve as a basis of comparison to later modeling work.Appropriate means of accounting for shear forces and stress rising due to the hole geometry were explored. At the outset, attempts were made to apply the work of Batistat and Usenik [24] or Hudson [64], whose papers provided stress concentration factors associating the ring geometry to the applied force. Upon reflection, however, the assumptions of these models were not entirely satisfactory, despite attempts to account for their differences. The fundamental problem was that they did have any internal jaws forming a barrier to inward motion, which this did, and which would have provided a support that the empty ring would have lacked. It was therefore decided to perform an analytical solution for the stresses within the ring itself, using the theory of linear elasticity.

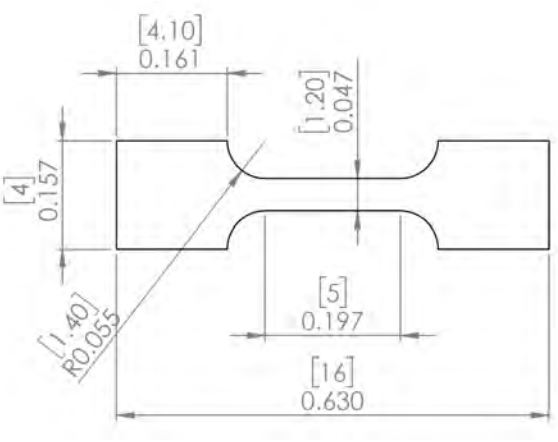

Figure 3.10: The SSJ2 tensile test specimen geometry. Primary measurements are inches, secondary, in brackets, are millimeters. Tolerances for this part are ±0.0002 in on all indicated dimensions; the thickness is not specified as it will be dependent on the sample stock thickness, polishing, and other factors, necessitating its measurement for each sample.

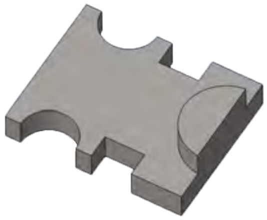

Figure 3.11: One of the ring-pulling grips; force is exerted internally by the semicircle.

3.5.2.1 Analytical Solution of the Ring-Test

To begin, as the stress is presumed to be applied evenly across the entire height of the ring to be tested, the system can be treated as a plane strain, in two dimensions. This suggests using the Airy stress function as a means of addressing the equilibrium and constitutive requirements of the solution in a single function. The general form of the solution is a sum of biharmonic functions; in polar coordinates some of these can be composed after Mitchell's form

$$\phi(r,\theta) = \sum_{n=0}^{\infty} \big(\sin(n\theta) f_n^{\sin}(r) + \cos(n\theta) f_n^{\cos}(r)\big) \tag{3.5}$$

$$f_0 = a_0 r^2 + b_0 r^2 \log(r) + c_0 + d_0 \log(r) \tag{3.6}$$

$$f_1 = a_1 r^3 + b_1 r + c_1 r \log(r) + \frac{d_1}{r} \tag{3.7}$$

$$f_n = a_n r^{n+2} + b_n r^n + c_n r^{2-n} + d_n r^{-n} \tag{3.8}$$

[12] Given the geometry of the ring, this is the obvious coordinate system to work with; the breaking of the symmetry from the uniaxial pulling suggests aligning the $\theta = \{0, \pi\}$ diameter along that direction, which shall be done.

As noted, the boundary conditions constitute the most critical part of this solution. The outer boundary, being nominally untouched by other surfaces makes for a traction-free boundary, which is to say $\boldsymbol{\sigma}(\hat{\boldsymbol{e}}_r) = \mathbf{0}$. The inner boundary is more taxing: imposing a stress or traction boundary condition purely in the direction of tensile loading neglects the support that the material body can provide to the ring, and we do not know going into the solution what that force should be. It is known, however, that the jaws are moving outward and that they are moving material around them. This suggests a displacement boundary condition. Other considerations: both jaws are moving apart in a balanced fashion, so the sign of the displacement must change past the $\{\pi/2, -\pi/2\}$ plane. Moreover, the jaws are moving parallel to the surface of the ring at that point, so (neglecting friction) the displacement that surface must be undergoing should vanish. Finally, the circular shape suggests the use of $\cos(\theta)$ as a proportionality function that fulfills the preceding two requirements; $\vec{u} = u\cos(\theta)\hat{\boldsymbol{e}}_x$. This, however, turns out to give the wrong parity for the displacement, while $\cos^2\theta$ shows the correct sign for all values of (r, θ) and has therefore been used.

In any case, finding the correct expression for the direction is done by transformation into polar coordinates by means of the connection tensor:

$$\begin{pmatrix} \hat{e}_x \\ \hat{e}_y \end{pmatrix} = \frac{\partial(x,y)}{\partial(r,\theta)} \cdot \begin{pmatrix} \hat{e}_r \\ \hat{e}_\theta \end{pmatrix} = \begin{pmatrix} \cos(\theta) & -r\sin(\theta) \\ \sin(\theta) & r\cos(\theta) \end{pmatrix} \cdot \begin{pmatrix} \hat{e}_r \\ \hat{e}_\theta \end{pmatrix} \tag{3.9}$$

This is solved for vanishing displacement in y, yielding the relationships

$$\hat{\boldsymbol{e}}_x = \cos(\theta)\hat{\boldsymbol{e}}_r \quad \hat{\boldsymbol{e}}_x = -\frac{\sin(\theta)}{r}\hat{\boldsymbol{e}}_\theta \tag{3.10}$$

which are then plugged into the line element of polar coordinates

$$ds = rd\theta\hat{\boldsymbol{e}}_\theta + dr\hat{\boldsymbol{e}}_r \to dx\hat{x} = \cos\theta\, dr\hat{x} - \sin\theta\, d\theta\hat{x} \tag{3.11}$$

to give the appropriate direction. Applying the $\cos^2$ displacement discussed above gives

$$\overset{\rightharpoonup}{u} = u\cos^2(\theta) \begin{pmatrix} \cos(\theta) \\ -\sin(\theta) \end{pmatrix} = \begin{pmatrix} \frac{1}{4}(3u\cos(\theta) + u\cos(3\theta)) \\ \frac{1}{4}(-u\sin(\theta) - u\sin(3\theta)) \end{pmatrix} \tag{3.12}$$

a visualization of which imposed displacements is shown in fig. 3.12.

The presence of $\cos(\theta)$, $\cos(3\theta)$, etc. suggests keeping only the terms from eq. 3.5 that are proportional to them. Consequently, the trial solution for the Airy stress function ϕ takes the form

$$\begin{aligned}\phi(r,\theta) =& \cos(\theta)\left(a_{11}r^3 + a_{12}r + a_{13}r\log(r) + \frac{a_{14}}{r}\right)\\ &+ \cos(3\theta)\left(a_{31}r^5 + a_{32}r^3 + \frac{a_{33}}{r} + \frac{a_{34}}{r^3}\right)\\ &+ \sin(\theta)\left(b_{11}r^3 + b_{12}r + b_{13}r\log(r) + \frac{b_{14}}{r}\right)\\ &+ \sin(3\theta)\left(b_{31}r^5 + b_{32}r^3 + \frac{b_{33}}{r} + \frac{b_{34}}{r^3}\right)\end{aligned}$$

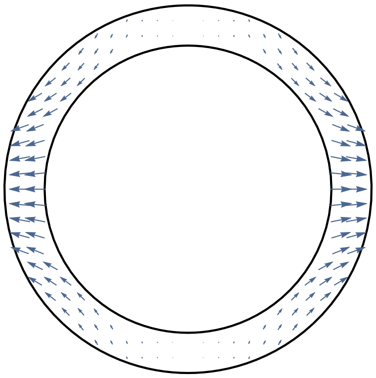

Figure 3.12: The strain boundary condition function as plotted over a nominal annulus.

In polar coordinates the Airy stress function has the following relationship with the displacements, neglecting potential functions or rigid displacements that are irrelevant to the problem:

$$u_r = -\frac{1+\nu}{E}\frac{\partial\phi}{\partial r} \qquad u_\theta = -\frac{1+\nu}{E}\frac{1}{r}\frac{\partial\phi}{\partial\theta}. \tag{3.13}$$

Applying these functions to the trial ϕ above, evaluating at the inner radius A and matching up linearly independent components ($\cos(\theta)$, etc.) gives the following eight relationships for the coefficients:

$$\begin{aligned}3A^2b_{11} - \frac{b_{14}}{A^2} + b_{13}\log(A) + b_{12} + b_{13} &= 0\\ -5A^8b_{31} - 3A^6b_{32} + A^2b_{33} + 3b_{34} &= 0\\ A^8b_{31} + A^6b_{32} + A^2b_{33} + b_{34} &= 0\\ A^4b_{11} + A^2b_{11} + A^2b_{13}\log(A) + b_{14} &= 0\\ u &= \frac{(4(\nu+1))\left(-5a_{31}A^8 - 3a_{32}A^6 + a_{33}A^2 + 3a_{34}\right)}{A^4E}\\ u &= -\frac{12(\nu+1)\left(a_{31}A^8 + a_{32}A^6 + a_{33}A^2 + a_{34}\right)}{A^4E}\\ u &= -\frac{(4(\nu+1))\left(3a_{11}A^2 - \frac{a_{14}}{A^2} + a_{13}\log(A) + a_{12} + a_{13}\right)}{3E}\\ u &= -\frac{4(\nu+1)\left(a_{11}A^4 + a_{12}A^2 + a_{13}A^2\log(A) + a_{14}\right)}{A^2E}\end{aligned}$$

The outer boundary condition, mentioned earlier, gives rise to the relationships at the outer radius B: $\sigma_{rr}(B,\theta) = 0$ and $\sigma_{\theta r}(B,\theta) = 0$. In order to make use of them, extracting the stress terms from the Airy function proceeds by the formulae

$$\begin{aligned}\sigma_{rr} &= \frac{1}{r}\partial_\theta\phi + \frac{1}{r^2}\partial_{\theta\theta}\phi\\ \sigma_{\theta\theta} &= \partial_{rr}\phi\\ \sigma_{r\theta} &= -\partial_r\Big(\frac{1}{r}\partial_\theta\phi\Big),\end{aligned}$$

the relevant two of which are then set to vanish. Once again, owing to the linear independence of cos, $\sin n\theta$, their coefficient groups must vanish independently, leading to another set of equations similar to those shown above, which have been elided for brevity.

With both sets of boundary conditions, it now becomes possible to solve the 16 simultaneous equations for the 16 coefficients, particularly with computer algebra systems. Surprisingly, a_{13} is nonetheless undefined with the equations provided, but it can be observed that, where it appears in determining a different coefficient, it is not proportional to the displacement u, it would imply a stress where none exists, and should be set to zero. The same is true for b_{13}. This leads to the Airy function

$$\begin{aligned}\phi(r,\theta) =& \frac{Eu}{12(\nu+1)r^3(A-B)^3(A+B)^3}\times\\ &\Bigg(-\frac{3r^2\left(A^2-B^2\right)^2\left(A^2\left(B^4+r^4\right)-2B^4r^2\right)}{A^2+B^2}\cos(\theta)\\ &+\frac{A^2(B-r)^2(B+r)^2}{A^4+4A^2B^2+B^4}\Big(2A^2B^2\left(A^4+A^2B^2+B^4\right)\\ &+r^2\left(A^6+A^4B^2+A^2B^4-3B^6\right)-6B^4r^4\Big)\cos(3\theta)\Bigg),\end{aligned} \tag{3.14}$$

which can now be used to find the stress at various points within the ring, particularly as a function of the force measured in the load cell.

In order to balance this with the force that the load-cell registers, it will be necessary to find the total force the ring imposes on the inner jaw that is antiparallel to the pulling force. The plane in which this acts has normal $-\hat{x}$, so that the stress at any given point may be found as $-\hat{x}\cdot\boldsymbol{\sigma}(-\hat{x})$, and then integrated over one-half of the inner surface. This expression for the stress amounts to σ_{xx} in cartesian coordinates, so a similarity transform between that and the polar coordinates that the solution employs is in order: $R^{-1}\cdot\boldsymbol{\sigma}\cdot R$, where R is the usual rotation matrix. The analytic solution this produces is longer than it is immediately informative; this can be condensed significantly by introducing the appropriate values for A and B—4.7625 mm and 5.7912 mm, respectively—by employing a representative value for E. This was 205.0 ± 21.3 GPa, as discussed in the section on nanoindentation, and by setting $r \to A$, as the surface of integration is a constant radius. These values give the following cartesian matrix for the stress:

$$\begin{aligned}
\sigma_{xx} &= u(472.598\cos(\theta) - 613.566\cos(3\theta) + 128.714\cos(5\theta)) \\
\sigma_{xy} &= u(471.806\sin(\theta) + 12.5029\sin(3\theta) - 128.714\sin(5\theta)) \\
\sigma_{yy} &= u(-502.646\cos(\theta) - 588.56\cos(3\theta) - 128.714\cos(5\theta))
\end{aligned}$$

where the numerical values are in units of $\mathrm{GPa\,mm^{-1}}$. The integral evaluated to

$$\int_0^h \int_{-\frac{\pi}{2}}^{\frac{\pi}{2}} \sigma_{xx}(A, \theta, u) A d\theta dz = 6694.76hu = F, \tag{3.15}$$

a simple linear relationship used in evaluating the strain at the maximum extension below, where h is the length in z of the test ring in mm, and F is in newtons. Evaluating and plugging this back into the system to obtain a maximum strain for a given measured load provides a link between the force and the strain throughout the system.

As to the evaluation of the maximum stress within the body—at which point the system would be expected to begin yielding, and subsequently to fail—the force in the body is carried around hoop, parallel to it. This suggests that $\sigma_{\theta\theta}$ is the relevant component of the stress tensor. That said, significant shear stresses are likely to occur within the body and may contribute significantly to the failure mode. For this reason it is appropriate to calculate the von Mises stress as well, giving the form

$$\begin{aligned}
\sigma_{\mathrm{vM}} &= \sqrt{\frac{3}{2}\sigma'_{\alpha\beta}\sigma'_{\alpha\beta}} \\
&= \frac{F}{h}\sqrt{0.000929153\cos(2\theta) + 0.000832571\cos(4\theta) + 0.0026595\cos(6\theta) + 0.00275608}
\end{aligned} \tag{3.16}$$

where $\sigma' = \sigma - \frac{1}{3}\mathrm{Tr}(\sigma)\mathbb{I}$. For both the $\sigma_{\theta\theta}$ and σ_{vM} extremal values are spaced at ≈ 60° intervals, starting from the loading axis. This 60° alignment was, in fact, observed during the 800° C tests, as shown in fig. 3.13, though not during the tests of the samples which had been treated to 1000° C. Consequently, both eq. 3.16 and $\sigma_{\theta\theta}$ been evaluated there to get a short form relating the sample height h and force to the maximum von Mises stress the sample experienced: $\sigma_{\theta\theta\ \mathrm{max}} = 0.119566F/h$ and $\sigma_{\mathrm{vM\ max}} = 0.0673403F/h$. Clearly the azimuthal stress is dominating the von Mises, and furthermore all breaks were essentially on surfaces of constant θ, so it will be the stress employed.

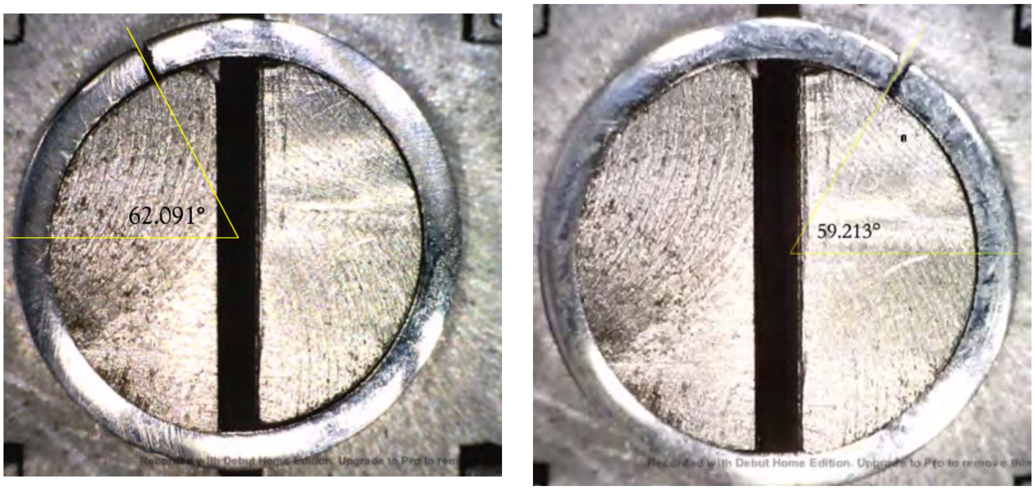

(a) 800°, Ring 1

(b) 800°, Ring 3

Figure 3.13: Breaks of the ring in parallel to the $\sigma_{\theta\theta}$ stress, at the approximately 60° calculated.

Chapter 4

Experimental Results

Samples were produced iteratively over the course of this work, with some variations as to heat treatments and other tests performed on each. As a result, it has been deemed worthwhile to provide an overview of the samples produced and tested, and by what means.

- Attritormilled 14YWT powder. Tests conducted on these samples:
  - Heat treated at temperatures from 400° C to 1100° C
  - Nanoindentation
  - Scanning electron microscopy
- Gas-atomized feedstock sprayed on coupons of 4130 stainless steel, which was not removed before heat treatment and testing. Tests conducted on these samples:
  - Vacuum heat treatments at 800° C and 1000° C
  - Nanoindentation, electron microscopy, and EBSD
- Gas-atomized feedstock sprayed on an aluminum substrate which was subsequently dissolved to leave a free-standing piece. Vacuum heat treatments at 800° C and 1100° C were performed at University of Wisconsin-Madison; UC Berkeley did not receive any non-treated samples of this run. Tests conducted on these samples:
  - Nanoindentation
  - EBSD
  - Tensile testing
  - Scanning electron microscopy
  - X-ray diffraction
  - Transmission electron microscopy on the 1100° C heat-treated material
  - Etching penetration examination on the 800° C heat-treated material

  - Commercial hot isostatic pressing
    - Tensile testing
    - Scanning electron micrography
    - Electron dispersive X-ray spectroscopy (EDS)
  - Iron ion irradiation at Argonne National Laboratory, followed by nanoindentation

- Gas atomized feestock sprayed on a cylindrical aluminum mandrel. The mandrel was subsequently dissolved, and the resulting tube sectioned into rings. Four rings were heat treated at 800° C and three at 1100° C.
  - Ring-jaw tensile testing
  - Scanning electron microscopy

4.1 Attritormilled 14YWT Powder

In sec. 1.4.1, there was some discussion about the employment of gas atomized powders for this work, rather than the more conventional attritormilled powders. This was not the original intention of the project. Early on, the Berkeley team received a 1 pound sample of 14YWT powder from Los Alamos National Laboratory[1] that had been prepared at Zoz GmbH, having been milled for 40 hours. It was assumed that the material would be severely work hardened and would require heat treatment prior to spraying. Work was carried out to attempt to identify the optimum temperature for annealing the powders, by conducting heat treatments under vacuum as described in sec. 3.1.2, followed by mounting in epoxy and polishing. The samples were indented at 200nm in all cases, this being the minimum depth at which the Platform3 produced acceptable loading-unloading curves, while endeavoring to avoid activating the epoxy mounting under the powder flakes. Fig. 4.1 shows the results of various heat treatment processes. As may be observed, significant softening did not occur until 1100° C, at which point premature precipitation of the desired oxide phases is considered a problem.

The morphology of the attritormilled 14YWT powder was also of concern. After mounting in epoxy and polishing, electron micrographs were taken in an effort to characterize the grain structure in which the indents had been made. Owing to the inexperience of the operator[2], the resolution of the images was insufficient to make definitive statements about the indents themselves, but were revealing as to the shape of the powder flakes. Fig. 4.2 illustrates wide, flattened plates with significant internal fracturing. This morphology is inimical to the cold-spray process, as the preferred orientation of the flakes with respect to one another allows them to bind within the nozzle. This, in combination with the hardness data discussed above, led to the adoption of gas atomized powder as feedstock for subsequent experiments.

---

[1] The author would like to express thanks to Dr. Stu Maloy for providing the material.

[2] The author, early in the Berkeley PhD program

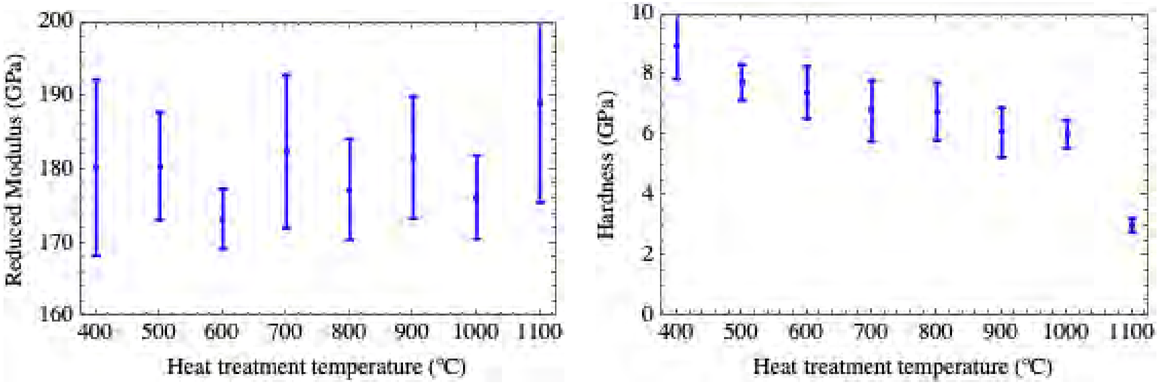

(a) (b)

Figure 4.1: Nanoindentation data for 14YWT powder. Indentation depth was 200nm.

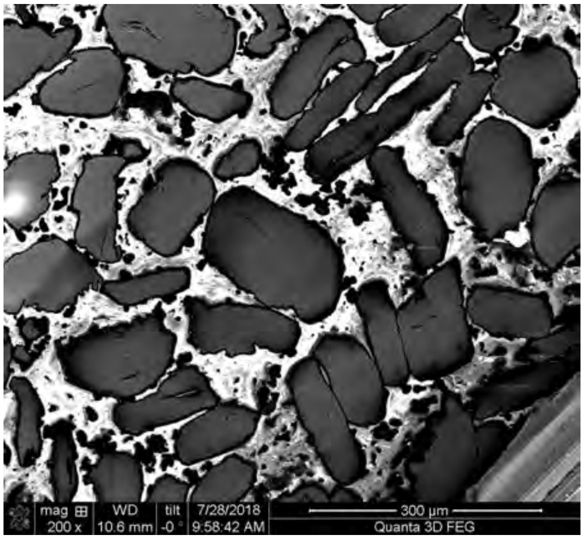

Figure 4.2: A sample of the attritormilled 14YWT, 500° C heat treatment, mounted in epoxy, polished, and imaged in the SEM, showing a plate morphology. The linear feature in the lower right-hand corner of the image is copper tape to mitigate sample charging.

4.2 Nanoparticle Size and Distribution

The gas-atomized powder provided to U. Wisconsin-Madison (viz. section 3.1.1) was examined for nanoparticles with TEM. Yttrium-rich particles were indeed found dispersed throughout the ferrite matrix, possessed of a wide range of diameters—from 20 to 200 nm. It was found, further, that the Y, Ti, and O were not completely homogenized.[89]

This work, however, did not reveal $Y_2Ti_2O_7$ nanoparticles by means of HRTEM. Quite the reverse, in fact. A sample was focused-ion-beam milled from the 1100° C treated free-standing sample and subjected to HRTEM; images from this exploration are shown in fig. 4.3.[3] Of course, the absence of a nanoparticle in any given image, or even the sequence of images presented, does not prove that there are no particles; in fact, assuming a distribution of $10^{23}\,\mathrm{m}^{-3}$, the density of particles in a projected area is $0.0022\,\mathrm{nm}^{-2}$. The images presented in figs. 4.3 are approximately 22.3nm on a side, and adding a 1nm margin on the assumption of 2 nm spherical nanoparticles, the expected number of particles visible in a given image would be 1.24. Using this expectation value as the parameter for the Poisson distribution implies that the probability of getting an image with no $Y_2Ti_2O_7$ particles visible is 28.9%, so that a single image not displaying a nanoparticle does not constitute evidence of their absence. However, a series of 80 such images were taken at the same scale, randomly distributed, and found no evidence of oxide particles. Using the probability just mentioned, and treating each image as an independent trial, the probability of no hits can be calculated by the binomial distribution:

$$\binom{n}{x} p^x (1-p)^{n-x}. \tag{4.1}$$

In this case, 80 successes out of 80 trials (n, x = 80) and p=0.289 gives a probability of 8.27×10^{-44}. The grotesque unlikelihood of this implies that there are not nanoparticles on the density expected for an NFA. In point of fact, to get an even chance of 80 trials and 80 successes, the odds of success for any given trial have to be above 99%. Continuing the calculations in the reverse direction implies that the expectation number of particles in an image must be no more than 0.00867, and this in turn demands a nanoparticle density less than $5.8 \times 10^{19}\,\mathrm{m}^{-3}$.

In some sense, this test was principally about thoroughness. The hardness of the piece, measures of which are presented in sec. 4.5.2.2 was sufficiently soft as to cast doubt on the presence of particles within acting to harden the system. This having been confirmed for the sample presented above, no further samples were subjected to the rather involved process of HRTEM.

In order to confirm the results above more thoroughly, the author arranged for powder XRD to be performed on the unsupported 14YWT samples that had been heat treated at 800° C and 1100° C.[4] The data from these tests is plotted in The Lawrence Livermore National Laboratory Materials Project [75], an online database of lattice constants, crystal structures, and similar, provided reference values for the XRD peaks of Fe, Cr, and W. These were combined linearly according to the atomic percent of the materials in the sample and the atomic form factors for scattering given by [47] via [52]. These gave two peaks of particular interest, 46.179° and 65.364°. It may be seen that these match well with the peaks observed. The same database also contains XRD numbers for $Y_2Ti_2O_7$, with the largest peaks at 30.392°, 50.688°, and 60.656°. Though the database gives only relative intensities, and these

---

[3] The author would like to express his utmost gratitude to Bengisu Yasar of Dr. Mary Scott's research group for her inestimable help in operating the TEM.

[4] Many thanks to Prof. Joe Graham's research group at MIssouri S&T—Rolla.

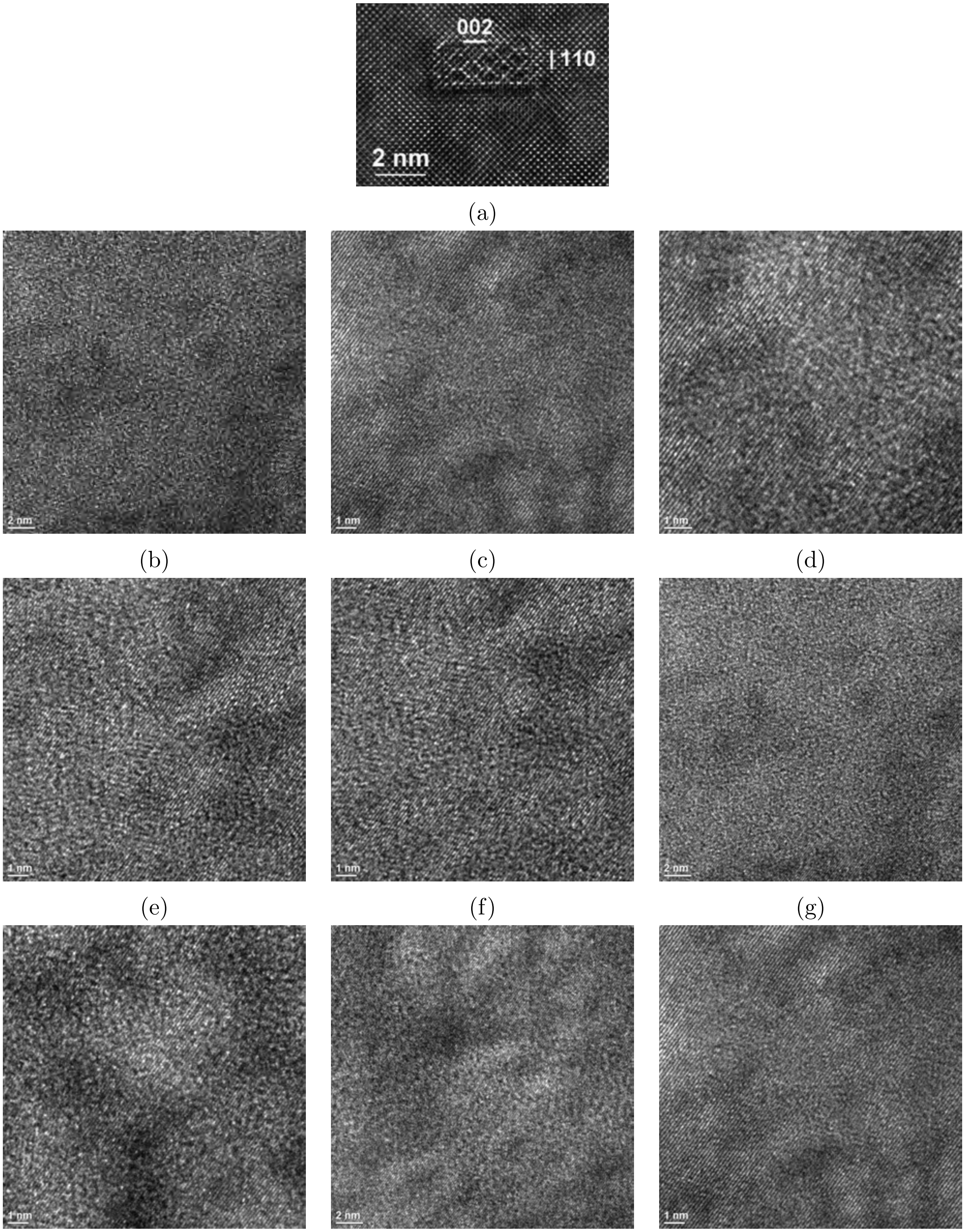

(a)

(b) (c) (d)

(e) (f) (g)

(h) (i) (j)

Figure 4.3: (a) An example TEM image showing an easily-recognized $Y_2Ti_2O_7$ nanoparticle embedded within the ferrite matrix, from [138]. (b-j) Images from the HRTEM exploration of the 1100° C searching for nanoparticles, showing a lack of lack of possible candidates.

cannot be considered commensurate, the use of the atomic form factors in combination with atomic percentages allows for the estimation of the size of a peak that would be caused by the presence of 0.25wt.% of the oxide. For the 800° C data, the expectation is 117 counts, and for the 1100° C, 185 counts. The smaller peaks on each of the curves are 220 and 169 counts, respectively, implying that $Y_2Ti_2O_7$ should be visible if present in the concentrations intended.

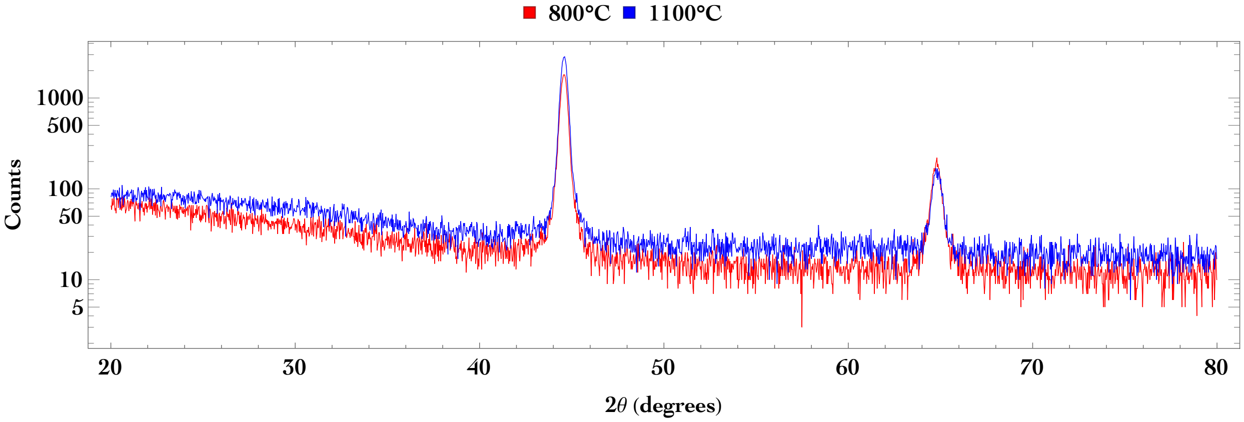

Figure 4.4: Powder XRD of 800° C and 1100° C heat treated pieces. The 800° C peaks are at 44.6° and 64.8°, and those of the 1100° C are at 44.6° and 64.7°.

4.3 Grain Size and Distribution

As discussed in sec. 2.1, the grain size and distribution contributes to the hardness and ductility of the material. EBSD has been an exceptionally productive tool for obtaining this data, in that it provides a mechanism for clearly delineating different regions by grain orientation, rather than by contrast mapping. That said, the visual comparison of grains is a useful method for rapid qualitative analysis, and in particular helped to rapidly explain certain hardness results, and is available in circumstances where EBSD is difficult to obtain, as is particularly relevant in sec. 4.3.1.1.

In all cases, the only phase EBSD identified was the ferrite phase—as might well be expected, as the nano-particles should be either absent or too small to be seen by this technique, and a combination of Fe-14Cr is stable in BCC from room temperature to melting. The step size was typically close to 0.4 μm, for a minimum resolvable $\Delta A = 0.16\,\mu\text{m}^2$ and a minimum reported area of 1.6 μm^2. In the size histograms that follow, therefore, grains smaller than this will not be represented; larger grains, however, are thought to be accurate.

4.3.1 Gas-atomized powder on 4130 substrate

In this experiment, gas atomized powder was deposited onto a 4130 steel coupon, where it remained through the heat treatment and subsequent characterization steps. The presence of a substrate during the spraying process is necessary until such time as the sprayed particles have achieved sufficient size to be self-supporting. In this case, a very thin layer was sprayed and the coupon not removed. As the presence of the coupon was not expected to have any deleterious effect on nanoindentation or EBSD, this was seen as a reasonable saving of material, processing time, and labor. Unfortunately, this assumption was proven wrong, but some valuable data was still collected from these samples.

4.3.1.1 Gas-atomized powder on 4130 substrate, unheated

Evaluating grains in the spray-formed plates with the substrate revealed information about the as-sprayed grain structure, and also demonstrated the importance of having spray-formed ODS alloys kept separate from Fe-C alloys during the heat treatment process. Fig. 4.5 shows the morphology of the as-sprayed surface. The smooth variation of the grayscale value is not typical of an SEM micrograph; grains display one value according to the degree of penetration of the electron beam as discussed in sec. 3.2. This implies that, at the resolution of the SEM images, the orientation of the grains with respect to the electron beam are also smoothly varying. This is not to say that the structure is amorphous, but consists of a high density of low-angle grain boundaries.

EBSD was difficult to obtain from this sample. Despite significant additional fine polishing, patterns did not improve. This is attributed to deformation of the material pervading the sample. As discussed in sec. 3.2.1, large amounts of cold-work create defects and strain, which blur the Kikuchi patterns formed by the crystal, and in turn inhibit recognition of orientation patterns. Some regions were identifiable, it is true; that said, of the $179.613\,\mu\text{m}^2$ mapped in one case, represented in table A.1, $140.056\,\mu\text{m}^2$ were null solutions separating minor patches of sufficiently ordered material.

One point of interest is that there was a tendency of regions having continuous EBSD solutions to have high aspect ratios—that is, to be significantly longer in one direction than the other. Most of these ratios were above 2, and three regions were above 5. These may have been the interiors of the sprayed particles that were stretched but did not undergo the same degree of adiabatic shear deformation as the exterior portion of the particles. They may also have had residual heat from the mechanical work done. Such could have allowed for localized annealing within the particles, particularly if residual oxides at the erstwhile particle surface retarded heat loss. It illustrates that, while the incoming particles do flatten during their impacts, the residual cold work is restricted to the perimeter of the impacted bodies.

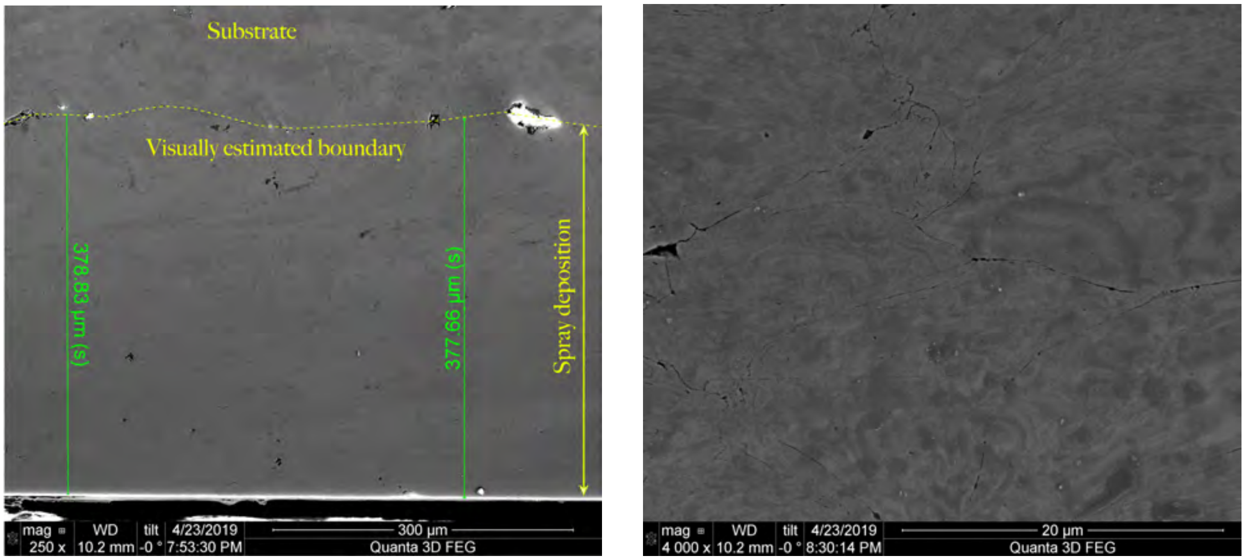

(a) SEM of a non-heat treated gas-atomized powder deposition on a 4130 steel coupon. The image is arranged such that the spray direction is to the bottom of the page and the substrate at the top, the actual thickness of the coupon being shown by the annotations on the image. As may be observed, the deposited component is, in this image, generally uniform with occasional porous or seam features.

(b) Non-heat treated 14YWT sprayed on substrate at 4000x magnification. The most telling aspect of this image is the absence of clear boundaries between one grain and another, replaced by a field of soft gradients. This may be explained by regions of extremely fine grains having been created in the collision process, leading to a prodigious number of grain-boundaries and perceptually continuous variation in the grain orientation.

Figure 4.5: SEM images of non-heat-treated 14YWT deposited on 4130 coupons and polished.

4.3.1.2 Gas-atomized powder on 4130 substrate, 800° C heat treatment

The 800° C treated piece, displayed in annotated overview in fig. 4.7a showed a distinct transition from the more smoothly-varying grayscale of the unheated sample to a piece with a defined grain structure. This suggests an annealing of high-stress regions within the previous sample. Also of particular importance is the differential grain structure that persists from the substrate-ODS boundary to about 60 μm into the deposited layer (viz. fig. 4.7b). This is believed to be the result of carbon diffusion, as will be discussed below.

Whereas in the preceding section it was practicable to include all of the grain detections, in this case the analysis software (Oxford Instruments' Tango) identified some 346 grains (and 443 regions, including zero solution patches). The particle sizes, however, were distributed according to the histogram shown in fig. 4.12, using only such data as was not along an edge of the frame. As the image suggests, there is a strong possibility that limited solutions from a smaller-grained, carbon-contaminated zone may be impacting the statistics and skewing

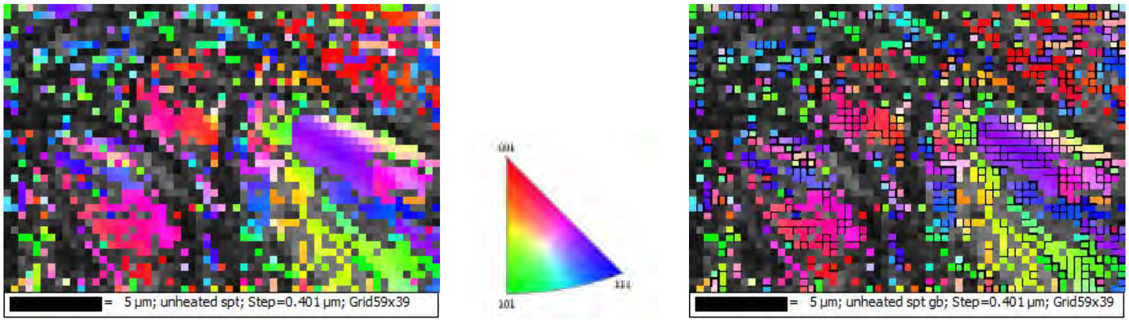

(a) Showing orientation only.

(b) Black lines between non-black regions represent grain boundaries of $> 10°$.

Figure 4.6: EBSD of 14YWT on the 4130 coupon, unheated. These images corroborate the large number of individual regions in the sample.

the histogram to smaller sizes; this must be compared to subsequent samples.

4.3.1.3 Gas-atomized powder on 4130 substrate, 1000° C heat treatment

The sample that underwent a 1000° C heat treatment provided an exceptional demonstration of the diffusion of carbon into the ODS alloy from the substrate. EDS line scans in fig. 4.10 illustrate that carbon is preferentially found in the finer-grained region of the sample. Fig. 4.11a shows the three regions of the sample—substrate, diffused, and largely free of diffused carbon—as well as a number of nanoindentations performed before the SEM experiment, and which had proven most confusing up to that point. Zooming in, as shown in fig. 4.11b also shows definite regions of porosity between what are presumed to be the deformed body of the sprayed feedstock particles.

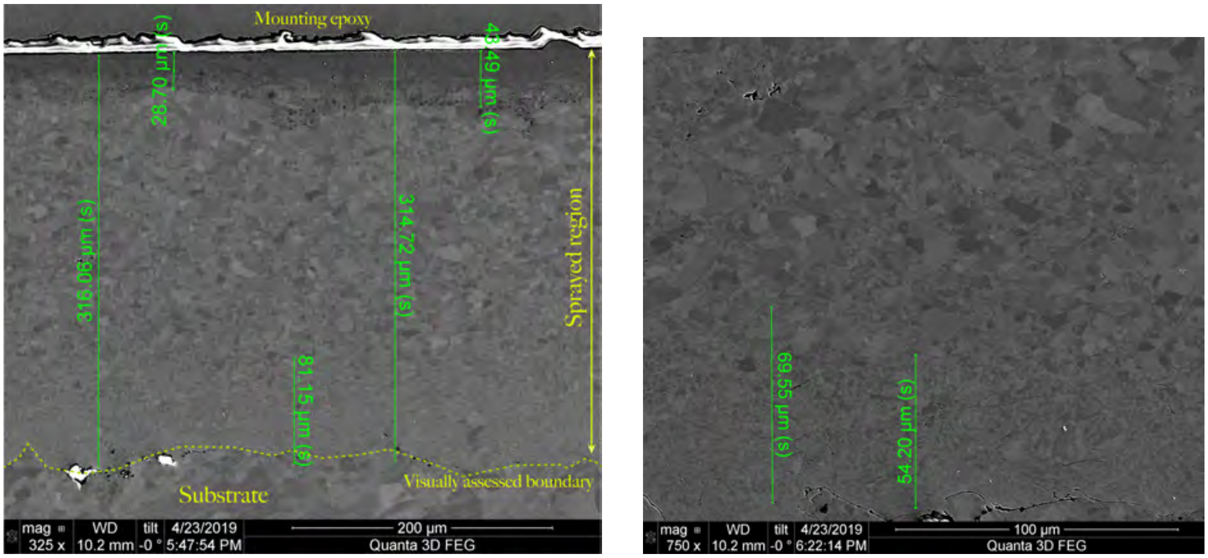

(a) (b)

Figure 4.7: Gas-atomized powder deposition on a 4130 coupon, having been treated for two hours at 800° C. In this case, the spray direction was from the top of the page. The region of discoloration of 30 to 40μm near the epoxy is puzzling, but two possibilities present themselves. First, it may be oxidation from the heat treatment process, though the tantalum getter makes this somewhat unlikely. Second, it could be a surface at a slight angle to the rest of the material owing to the relative softness of the epoxy compared to the iron, and the errors intrinsic to hand polishing.

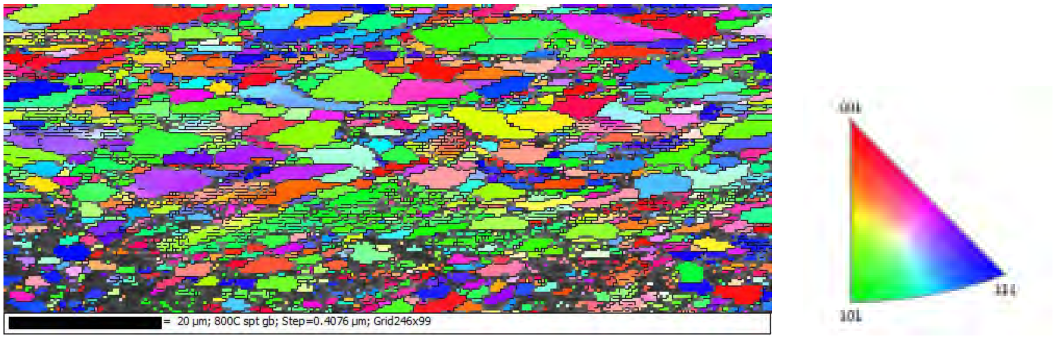

Figure 4.8: EBSD map of the 4130 supported, 800° C treated sample. Black lines represent grain boundaries of > 10°.

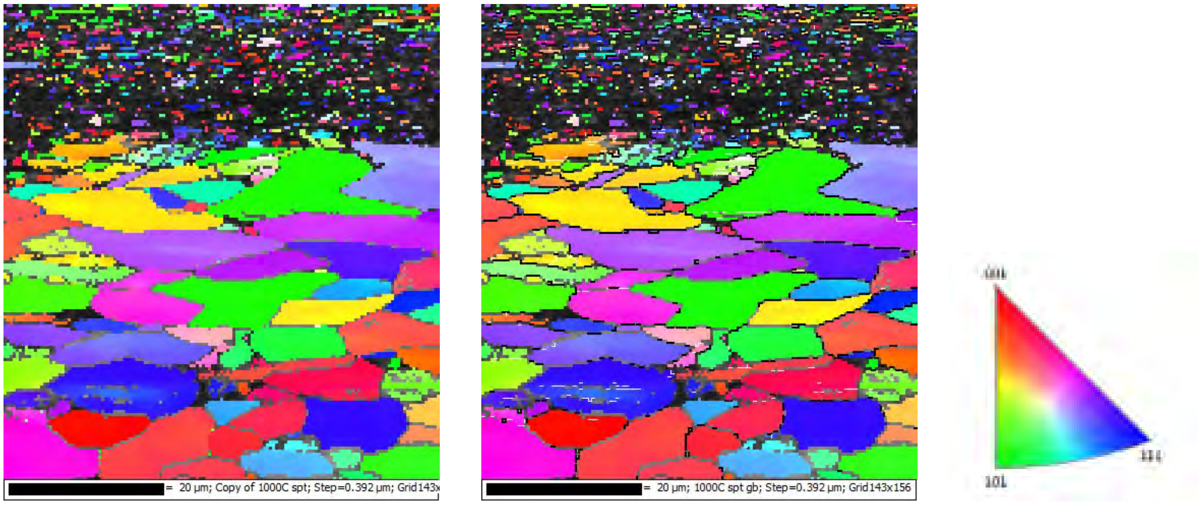

Figure 4.9: EBSD of the 4130 supported sample after a 1000° C heat treatment, showing a clear difference between the coarse-grained area far from the substrate, and the fine-grained area where zero-solutions dominated. Additionally, image (b) shows small grain boundaries (2°) in white and large (10°) grain boundaries in black, showing a finer-grained structure than might have been expected according to the first image.

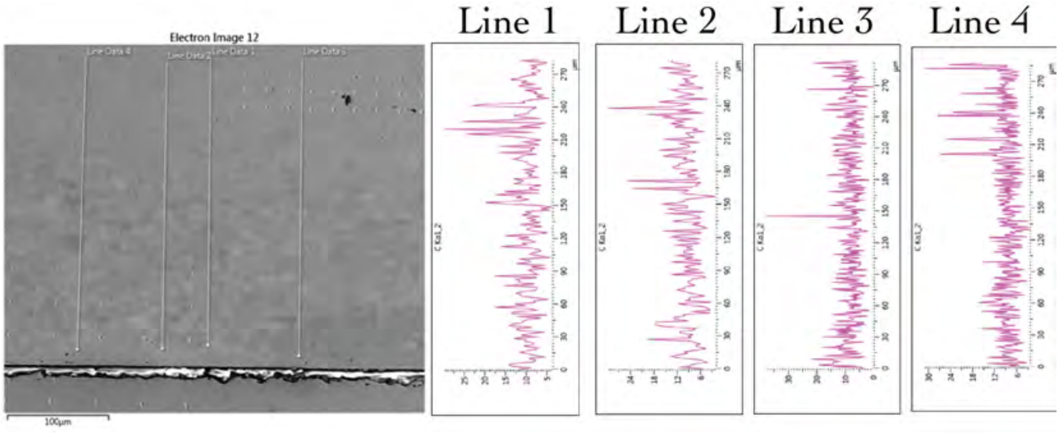

Figure 4.10: EDS lines across a section of the gas-atomized powder deposited on a 4130 coupon, showing increased carbon content near the substrate.

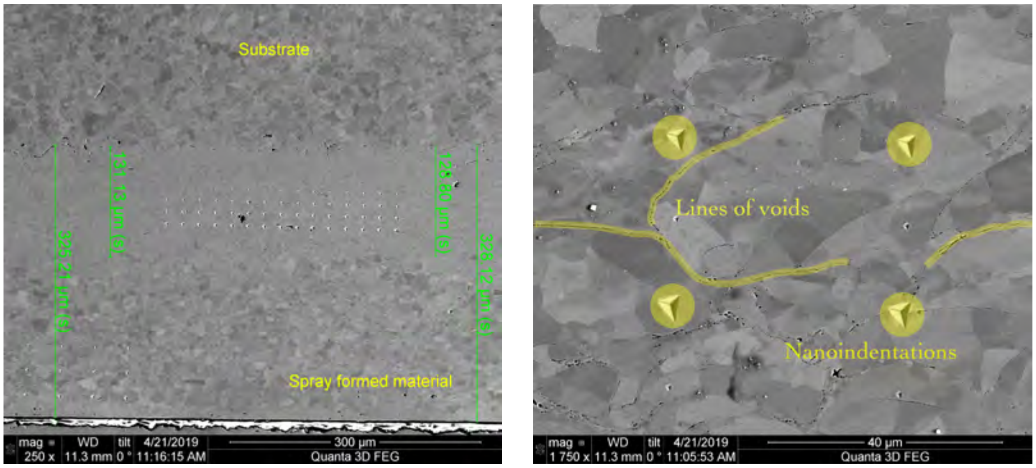

(a) The sprayed 14YWT on 4130 after a 1000° C heat treatment, showing two very distinct grain size regions due to diffusion of carbon from the substrate.

(b) A further magnification of the 4130 supported, 1000° C heat treatment. Lines of voids mark the boundary between the particles originally sprayed.

Figure 4.11

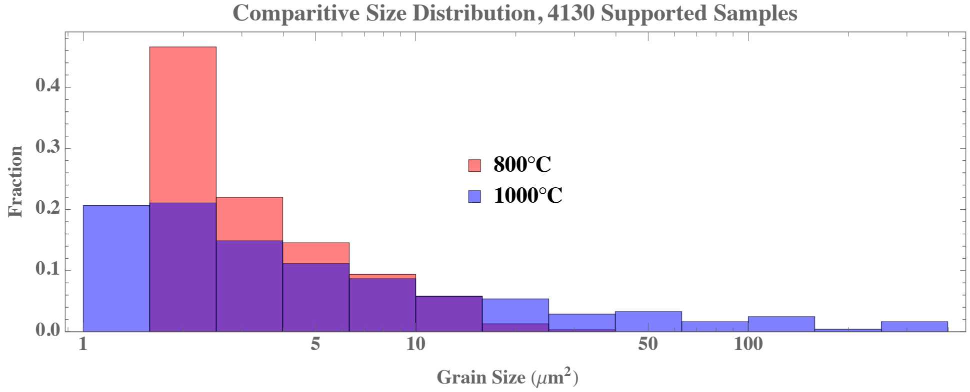

Figure 4.12: Distribution of grain sizes from the coupon supported samples.

4.3.2 Free Standing Plate

These plates were sprayed onto a 6061-T6 aluminum substrate using 95% He/5% N_2 carrier gas at approximately 40 bar (4 MPa), rastering to build up a continuous surface. The substrate was dissolved away by means of a 20% NaOH solution, and portions of resulting samples were vacuum heat treated for 1 hour at 800° C, 1000° C, and 1100° C. [89, 88, 2].

4.3.2.1 Free-standing plate, 800° C heat treatment

The EBSD data for the 800° C, figures 4.13a and 4.13b show behavior related to the similarly-heated supported samples of sec. 4.3.1.2, with significantly damaged regions providing either small individual grains or zero solutions. This is further corroborated by the similarities between the size histograms (figs. 4.12 and 4.13d). In both cases the 800° C heat treatment has had some coarsening effects, but there are still large regions of extremely damaged material that are unable to produce reliable EBSD patterns.

4.3.2.2 Free-standing 1100° C heat treatment

As before, the histogram presented, fig. 4.13d, shows only those grains which were not on an edge of the frame. It may be seen that, at this point, the distribution is, as compared to the 4130 substrate supported 1000° C sample, tending both toward larger and smaller particles. The larger are considered to be regions in which the plastic deformation of the original sprayed particle was not as intense, so that the local disordering was not as great as on the periphery, in turn reducing the local grain nucleation potential and sites, allowing the large grains to form effectively. On the periphery, the reverse would have been true, and this is supported by fig. 4.13c. The nature of the grain sizes is sufficiently bimodal that a naïve analysis of the area of the grains so imaged (neglecting those on the boundary), reveals an average area $11.5 \pm 17.7\,\mu\text{m}^2$. In order to divide the grains into two size groups, the mean and standard deviation for both groups were plotted as a function of the point of division. On this basis $18\,\mu\text{m}^2$ became the splitting point, as the region showed local stability with respect to mean, standard deviation, and particle count. With this demarcation, the small grains accounted for 37.4% of the area considered, but 94 out of the 110 grains under consideration—further supporting the separation into two separate groups. This having been done, the particle major dimension d, provided by the Oxford Instruments EBSD analysis software for each group was $2.37 \pm 0.91\,\mu\text{m}$ and $7.81 \pm 1.99\,\mu\text{m}$, respectively—the single linear dimension having been employed instead of area to compare more directly with other papers which provide this measure preferentially to grain area.

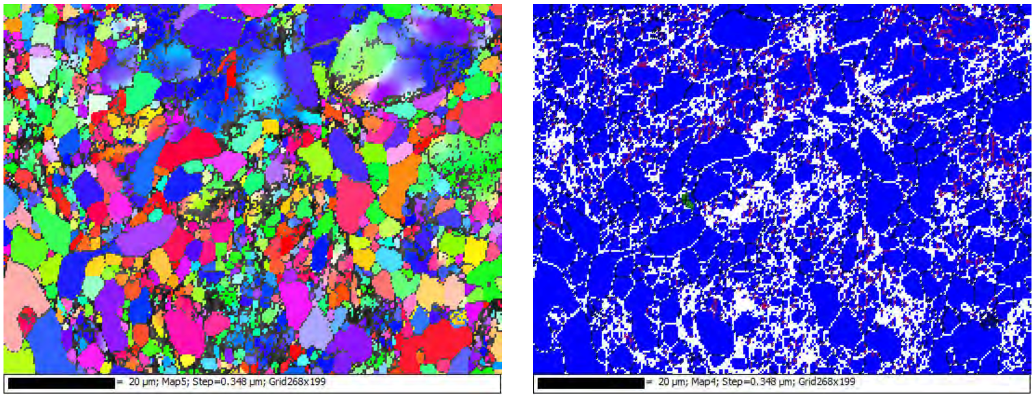

(a) 800° C. IPF-colored grains are overlaid on the band contrast.

(b) 800° C High-angle grain boundaries are in black and low-angle boundaries are in red. The white spaces represent zero-solution points.

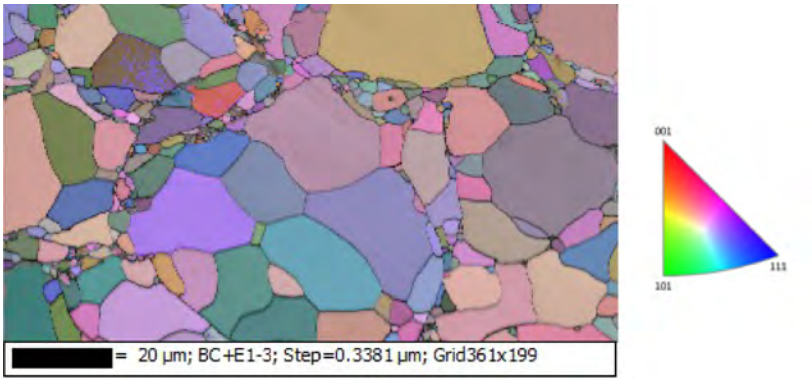

(c) 1100° C. Of particular interest is the combination of relatively large grains immediately adjacent to lines of smaller grains; these are presumably the result of a surfeit of grain nucleation sites near the highly deformed and damaged regions between the originally sprayed particles.

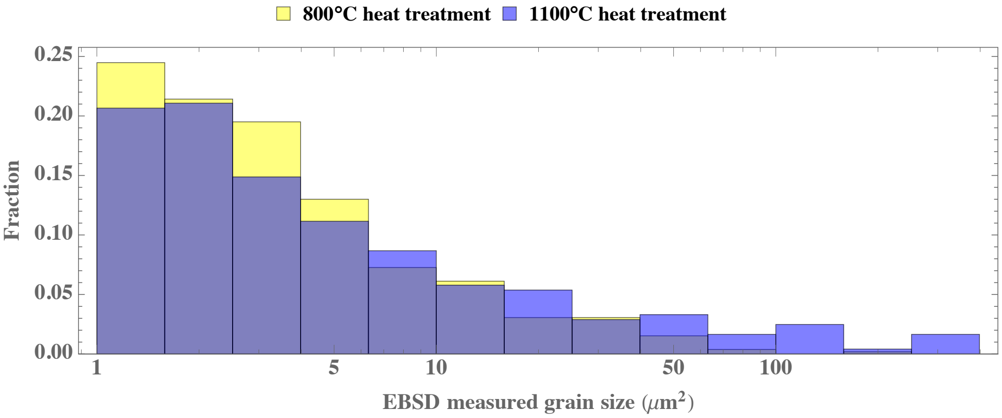

(d) Distribution of grain sizes from the free-standing samples.

Figure 4.13: EBSD maps of the free standing samples, heat treated at 800° C and 1100° C, and a histogram of their grain size distributions

4.4 Grain Orientation

4.4.1 4130 Steel Substrate Samples

Despite the existence of carbon contamination in parts of the samples, it was possible to obtain reasonable grain orientation maps and statistics in the undiffused regions. These are displayed in figs. 4.14a, 4.14b, and 4.14c. In the as-sprayed and 1100° C heat-treated pieces, the distribution is apparently uniformly distributed, implying a lack of texture and a correspondingly isotropic material at bulk scales. Curiously, however, the 800° C piece suggests a [100] texture. It may be that this is related to the substrate and diffusion of carbon into the piece, with an alignment of more martensitic grains between the 4130 base and the more pristine 14YWT to minimize strains within the system. Lack of texture in the 1100° C piece might then be attributed to relaxation and greater diffusion so as to reduce the aligning tendencies.

4.4.2 Free-standing plate

The free-standing plate grain orientations can be found in figs. 4.15a and 4.15b. In this case, the 800° C suggest the presence of a [100] texture, though an inspection of fig. 4.13a, suggests that this may be the result of having chosen a region dominated by a few especially large grains. Its statistical validity may, therefore, be in doubt. The 1100° C pole figure shows a complete lack of texture.

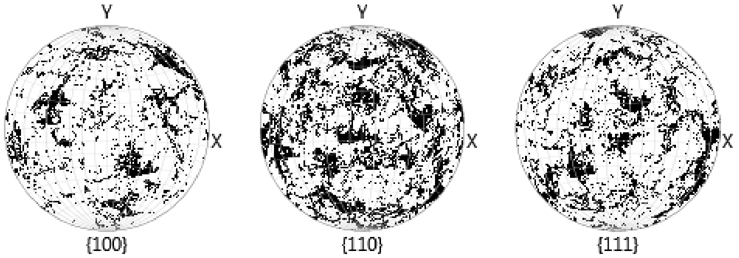

(a) Unheated, with comparatively few solution points.

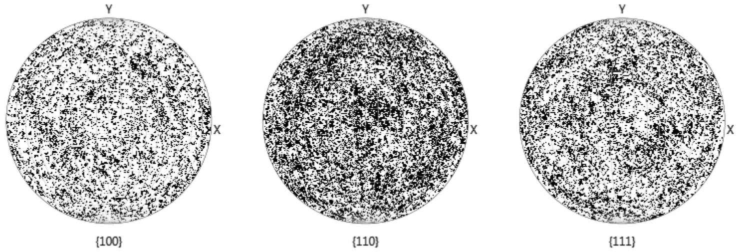

(b) 800° C. This plot hints at the presence of a [100] texture.

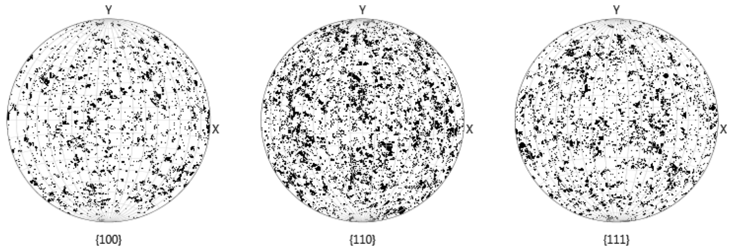

(c) 1000° C

Figure 4.14: Pole figures from substrate-supported samples.

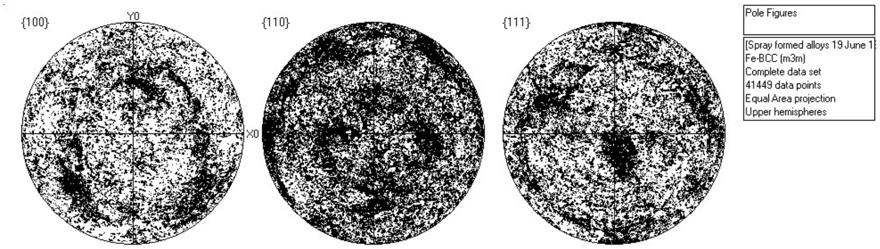

(a) 800° C. The three somewhat-evenly spaced patches in the 111 figure, combined with the quatrefoil in the 110 figure, suggest a weak [111] texture.

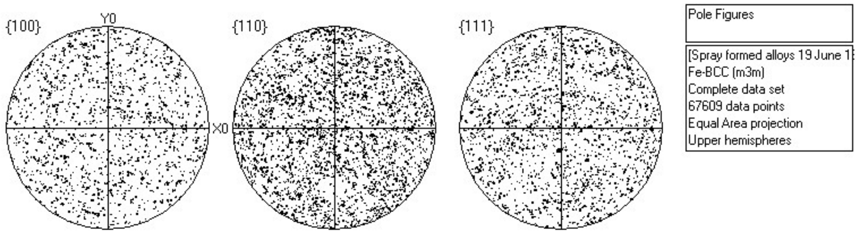

(b) 1100° C

Figure 4.15: Pole figures for freestanding samples.

4.5 Hardness and Reduced Modulus

4.5.1 4130 Steel Substrate Sample

4.5.1.1 Coupon supported, unheated

The sample that did not undergo heat treatment, with the morphology shown in 4.5, showed a range of loading curve behaviors. After inspecting all the curves taken and removing those which were of inferior quality, the remaining were analyzed for the consistency of the curve shape. It became apparent that these curves could be partitioned into sets in which the indentation portions overlaid each other. The modulus and hardness values produced by each of the groups had significantly lower standard deviations than the set of indentation curves as a whole. The different groups may be seen by color in fig. 4.16. The groups had the following hardness values: blue, 3.17 ± 0.08 GPa; red, 3.57 ± 0.11 GPa; and green, 2.91 ± 0.10 GPa. Their reduced moduli were, in turn, blue, 171.8 ± 15.9 GPa; red, 165.5 ± 13.4 GPa; and green, 177.4 ± 22.4 GPa. A quick inspection of the elastic moduli shows that they are mutually within their error bars, but doing so with the hardnesses shows no overlap. The inference is that the degree of cold work spread throughout the sample is not uniform.

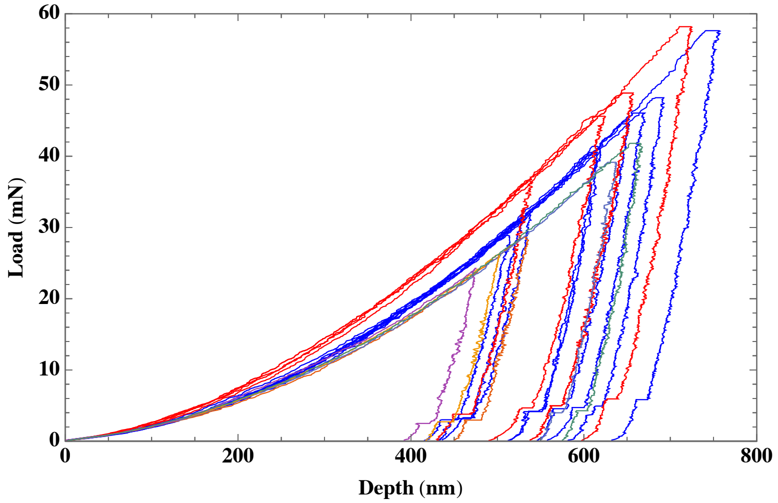

Figure 4.16: Nanoindentations on the 4130 coupon supported material, unheated, could be grouped according to the loading curve created. The measured values for the blue, red, and green groups were: E_r: 171.8 ± 15.9 GPa, H: 3.17 ± 0.08 GPa; E_r: 165.5 ± 13.4 GPa, H: 3.57 ± 0.11 GPa; and E_r: 177.4 ± 22.4 GPa, H: 2.91 ± 0.10 GPa, respectively.

4.5.1.2 Coupon supported, 800° C heat-treated sample

A very large number of indents were made in this case. Many of the load-unload curves showed nearly discontinuous behavior in their unloading section; an example of such behavior is shown in fig. 4.17. Such a curve does not provide a reliable estimate of the reduced modulus. As a result, an additional restriction was placed upon the curves incorporated into this data set: that the mean square error of the fit on that part of the curve should be less than 0.8, as calculated by the MicroMaterials software. This, when combined with the typical assessment of the indenting portion of the curve, provided a relatively clean—though hardly ideal—set of loading-unloading curves from which to infer the hardness and elastic modulus of the material as deposited. The mean values for hardness and modulus are $2.38 \pm 0.19\,\mathrm{GPa}$ and $212.3 \pm 36.3\,\mathrm{GPa}$, respectively. Annealing of some of the defects seen in the unheated sample may account for this softening.

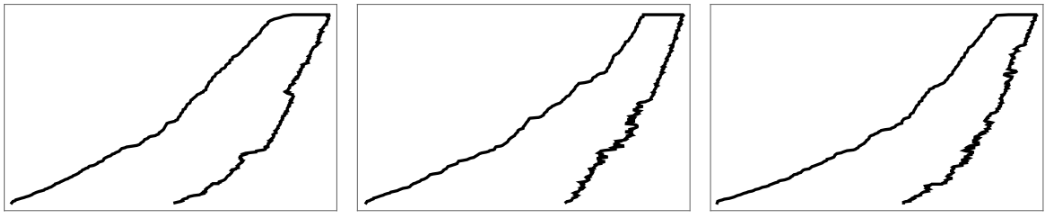

Figure 4.17: Examples of load curve shapes which give unreliable reduced moduli.

4.5.1.3 Coupon supported 1000° C heat-treated sample

This piece illustrates the importance of having multiple means of analyzing a sample. Initially, the data were scattered, even bimodal in their behavior. SEM revealed details about the locations in which the indents had fallen which satisfactorily resolved the question, as shown originally in fig. 4.11a, and incidentally providing an excellent demonstration of Hall-Petch hardening. The nanoindentations that fell in the very fine-grained structure near the substrate were naturally rejected. It is true that an optical microscope could have spotted the indents outside the region, so that SEM was not unique for that application, but nonetheless quite satisfactory to the purpose.

The nanoindentation data presented correspond to the curves shown in fig. 4.18b, which were chosen from a larger set. These had average hardness and reduced modulus of $2.12 \pm 0.17\,\mathrm{GPa}$ and $218.1 \pm 36.5\,\mathrm{GPa}$, respectively—slightly softer than the 800° C heat treated piece, but not statistically different in its reduced modulus..

4.5.2 Free-Standing Plate

These samples were produced and heat-treated at the University of Wisconsin, using the vacuum furnace process. They report that their vacuum for this process was 0.85 Torr [3], which may have had a deleterious effect on the plate if excess oxygen managed to diffuse into the bulk. The surface, however, did not show signs of oxidation; moreover, surface oxidation would have been removed during the polishing steps prior to the nanoindentation.

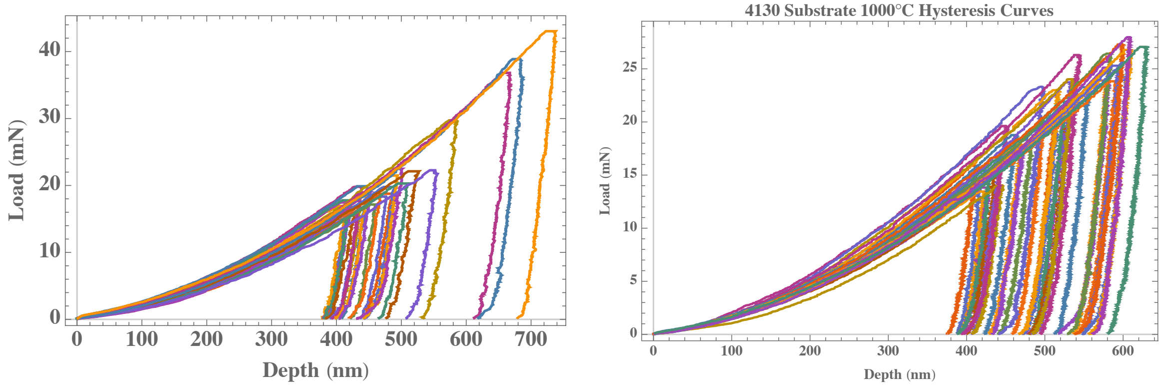

(a) 4130 coupon, 800° C heat treated piece. Er: 212.3 ± 36.3 GPa, H: 2.375 ± 0.2 GPa

(b) 1000° C treated piece, sufficiently far from the diffusion zone to be considered acceptable.

Figure 4.18: Accepted loading-unloading curves for the 4130 substrate supported samples.

4.5.2.1 Free-standing 800° C heat treatment

The loading-unloading curves from this sample are shown in fig. 4.19b. During examination of these curves, it became apparent that there were two groups into which the curves could be sorted, shown as red and blue in said plot. The values calculated from each of these sets may be found in tables A.4 and A.5, and a small but statistically significant difference in hardness can be found in each of these regions, while the elastic moduli found for the regions are statistically equivalent. The underlying cause of the difference is not known at this time, though owing to the fact that the red curves tend to be in sequence, it may have something to do with the particular region of the sample they were in at that time.The presence of the two red lines down at 1073nm, 1243nm, and 1315nm suggest that the effect is not one based upon depth.

4.5.2.2 Free-standing 1100° C heat treatment

The loading-unloading curves for this data were notably clean, as may be seen in fig. 4.19a. Data extracted from these curves are found in table A.6. Though significantly fewer in number than the indents presented for the coupon geometry indentations, these did have a much tighter distribution for both types of measurements and so fewer are justified. One significant point, however, is that the depth on these indents are significantly greater than those taken for the substrate-attached samples of sec. 4.5.1—at least double, in fact. Nonetheless, while the hardnesses of the 1000C supported and the 1100C free-standing did show a small but statistically significant difference in hardness, their reduced moduli were statistically equivalent, supporting the mutual acceptability of the data.

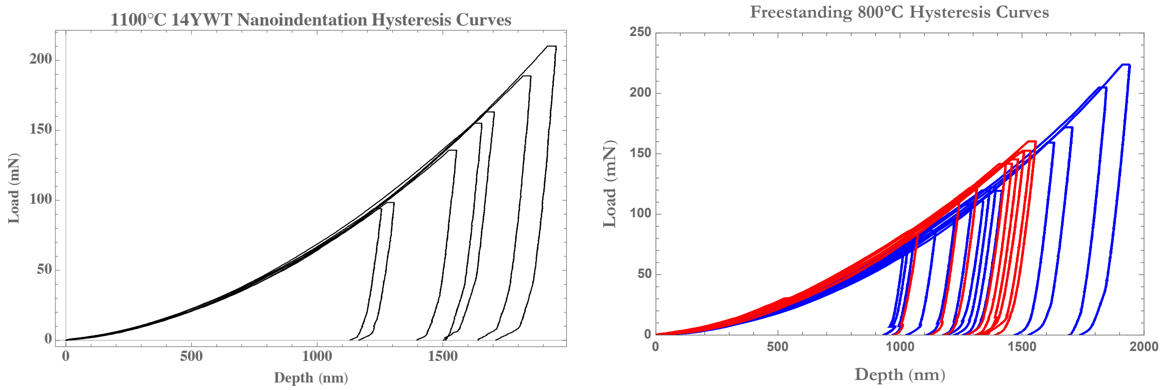

(a)

(b) The series showed two slightly different behavioral regions delineated here by red and blue coloring.

Figure 4.19: Loading-unloading curves of indents in freestanding samples chosen for analysis.

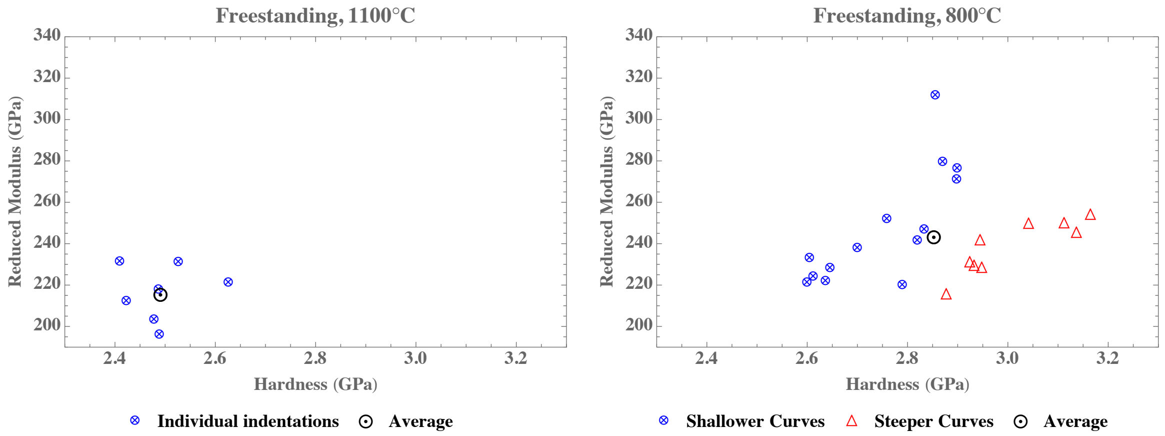

(a) E_r: 216.3 ± 13.3 GPa, H: 2.49 ± 0.07 GPa

(b) E_r: 244.1 ± 23.0 GPa, H: 2.85 ± 0.17 GPa

Figure 4.20

4.5.3 Irradiated 1100° C heat-treated free-standing plate

Argonne National Laboratory (ANL) irradiated 1100° C freestanding 14YWT with 90 MeV Fe ions to approximately 20 dpa at $2\,\mu$m, while the sample was held at 350° C. Fig. 4.21 shows ANL calculations for the expected damage as a function of depth for the irradiation conducted. These were then nanoindented at UC Berkeley. [5]

As fig. 4.22a, there was some surface burn evident, which is most likely due to slight

---

[5] The author would like to express his gratitude to Dr. Xi Huang, a post-doc in the Hosemann Group, for taking this data.

carbon contamination. While this is undesirable, it has the redeeming feature that clearly bounds where the beam hit. Moreover, it may be only tens of nanometers deep, possibly hundreds of nanometers. [4] This would amount to local case hardening of the material to that depth. As the nanoindentations performed were tens to hundreds of nanometers deep, this may have had a negative effect on the quality of the test. With this caveat in mind, there was a distinct difference in the hardness of the 14YWT between the unirratdiated and irradiated regions, as shown in both images of fig. 4.22.

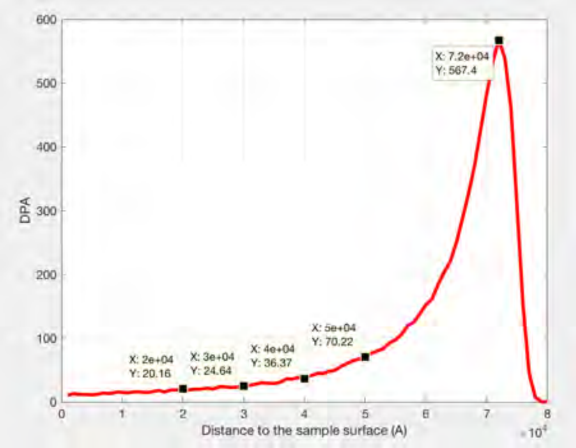

Figure 4.21: Calculated damage as a function of depth caused by the irradiation campaign.

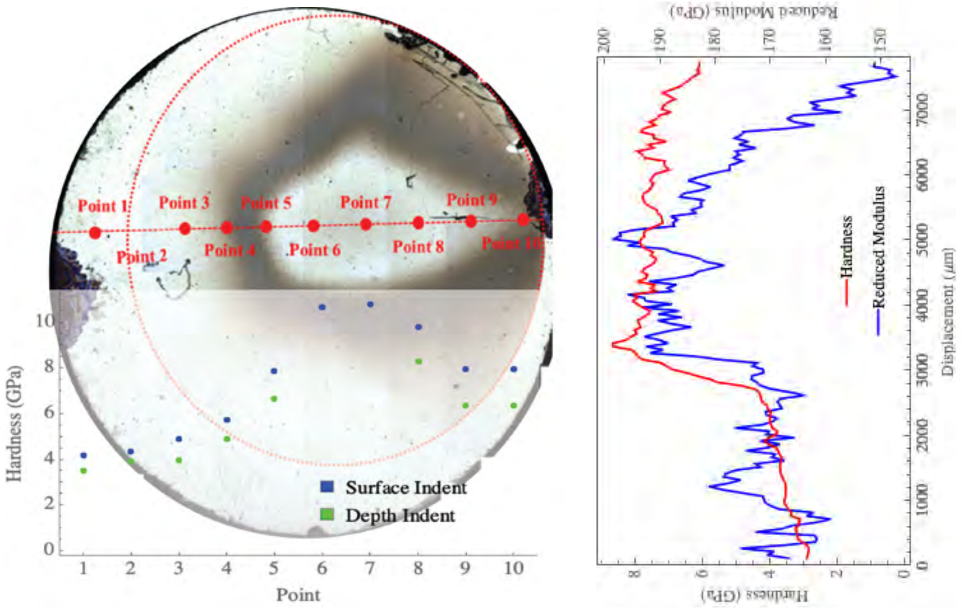

(a) A series of indents both near the surface (< 50 nm) and at depth (> 70 nm) were taken with a Hysitron TI950 at the positions depicted on the image of the irradiated sample. The burn mark marks the periphery of the beam impact on the sample.

(b) A series of nanoindentation tests spaced at 50 μm was conducted across the surface of the sample, to a depth of 300 ± 15 nm. To enhance clarity while retaining key features, the lines have been smoothed by a moving average of 3 points width.

Figure 4.22: Nanoindentation results for Fe-ion irradiated 14YWT.

4.6 Yield and Ultimate Tensile Strength

4.6.0.1 Ring Tensile Test Data

Four 800° C—treated rings and three treated at 1000° C were tested; more were desired, but the tube itself cracked longitudinally in four places whilst being clamped for sawing. All the samples showed brittle behavior, limited difference between the stress at the yield point.

Though an effort was made to remove errors induced by the initial movement of the jaws into position at a small fixed load—2 N—this was not successful in eliminating the early motion of the system. Friction is presumed to have played a significant role in the motion of the system to this point, leading to a distinct knee where friction is presumed to have stopped and tensile forces begun to dominate. In order to compensate for this in the calculation of the strain at the point of rupture, the linear fit to the elastic region of the force curve was propagated back and its intercept with the abscissa taken as the origin. So doing has provided a direct means of comparing the individual force/displacement curves generated, and which are shown in fig. 4.23.

Despite the data being limited, these tensile tests suggest that the 1000° C heat treatment was more conducive than the 800° C treatment for increasing both the yield strength and stress of the spray-formed 14YWT. This is suspected to be the result of diffusion bonding between the spray-formed particles being more rapid at higher temperatures. This is likewise corroborated by the pair of micrographs in fig. 4.25: the 800° C treatment has surface features which show granular surfaces, while the 1000° C show sharp boundaries corresponding to cleavage planes within the iron matrix (see fig 4.25c for a further magnified image). These images may be regarded as typical of their respective surfaces, so that in the 800° C the crack propagated in large part around the sprayed particles, while in the 1000° C sample it was necessary for the crack to pass through the steel. For the latter to have been a difference, the 1000° C rings would necessarily have had to be better consolidated by the heat treatment.

These yield and ultimate tensile strength stresses, though low, are not thought to be unrepresentative of the material in question. While cutting more rings for further tests, the spray-formed tube stock cracked longitudinally in four places—along the four-fold symmetry axes, predictably—due to the clamping force of the sectioning saw vise. This was not a heavy-duty item, and so this event speaks more to the fragility of the samples so formed than to anything else.

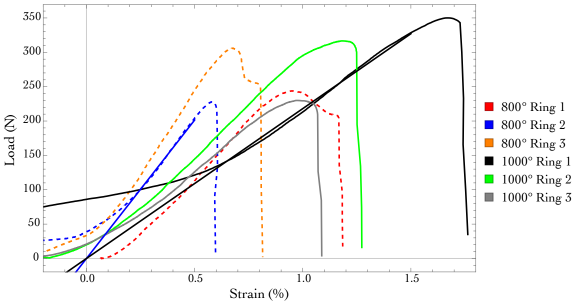

Figure 4.23: Force vs strain for ring tensile tests conducted on the Kammrath-Weiss module, aligned according to the intercept of the linear region with the abscissa. Two such linear fits are shown, associated with 800° C Ring 3 and 1000° C Ring 1. For added clarity, the 800° C heat-treated rings are shown with dashed lines.

4.6.0.2 SSJ2 Tensile Test Data

The SSJ2 tensile bars described in section 3.5.1 provided additional data as to the performance of spray-formed 14YWT. The initial round of tests were conducted on three free-standing spray-formed plates, two of which were vacuum heat-treated at 800° C and 1100° C, respectively, while remaining plate was left in the as-sprayed condition. As the spray deposition head travels in one direction for a significant distance in one direction before stepping orthogonally, tensile bars were cut in both orientations to confirm or reject possible anisotropy in tensile properties resulting thereby. Those cut parallel to the travel direction were denoted H, while those parallel to the step direction were denoted V. From the plots in figures 4.24a and 4.24b, heat treating at 1100° C has imparted significantly greater ductility to the material—failure occurred at 27.5 ± 1.6% strain for the higher temperature treatment, while the 800° C heat treated piece fractured at 6.5 ± 1.1% strain. This was at the expense of some yield strength: the 800° C heat treated samples had a yield strength of 398.0 ± 41.3 MPa while the 1100° C treated samples yielded at 310.4 ± 99.3 MPa.

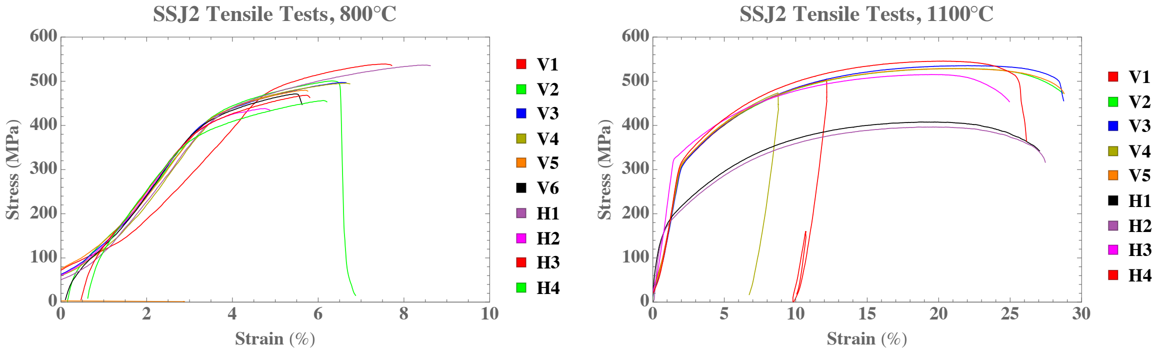

(a) (b)

Figure 4.24: The two curves in (b) which drop precipitously below 15% strain are artifacts of the force imparted on the tensile specimen exceeding the 500 N load limit of the cell, leading to the termination of the run before achievement of the UTS. Nonetheless, the curves do show agreement with the behavior of the other samples up to that point.

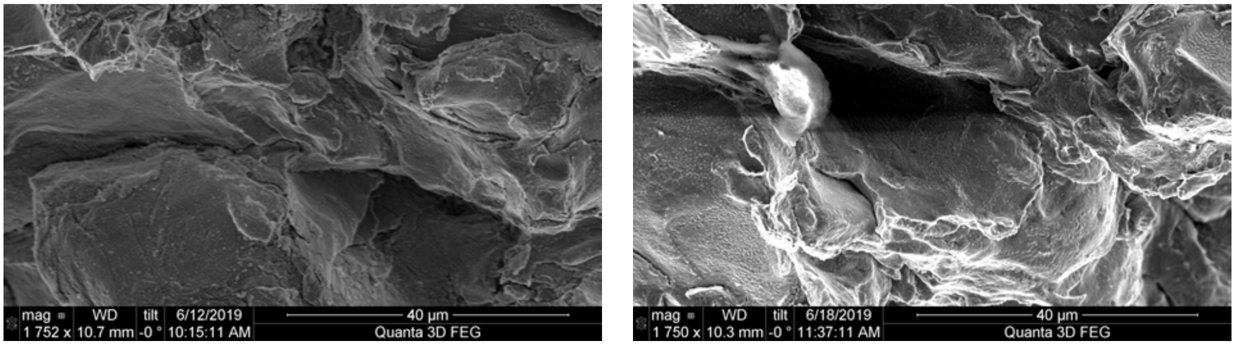

(a) 800°, Ring 3 breakage imaged with secondary electrons.

(b) 1000°, Ring 3

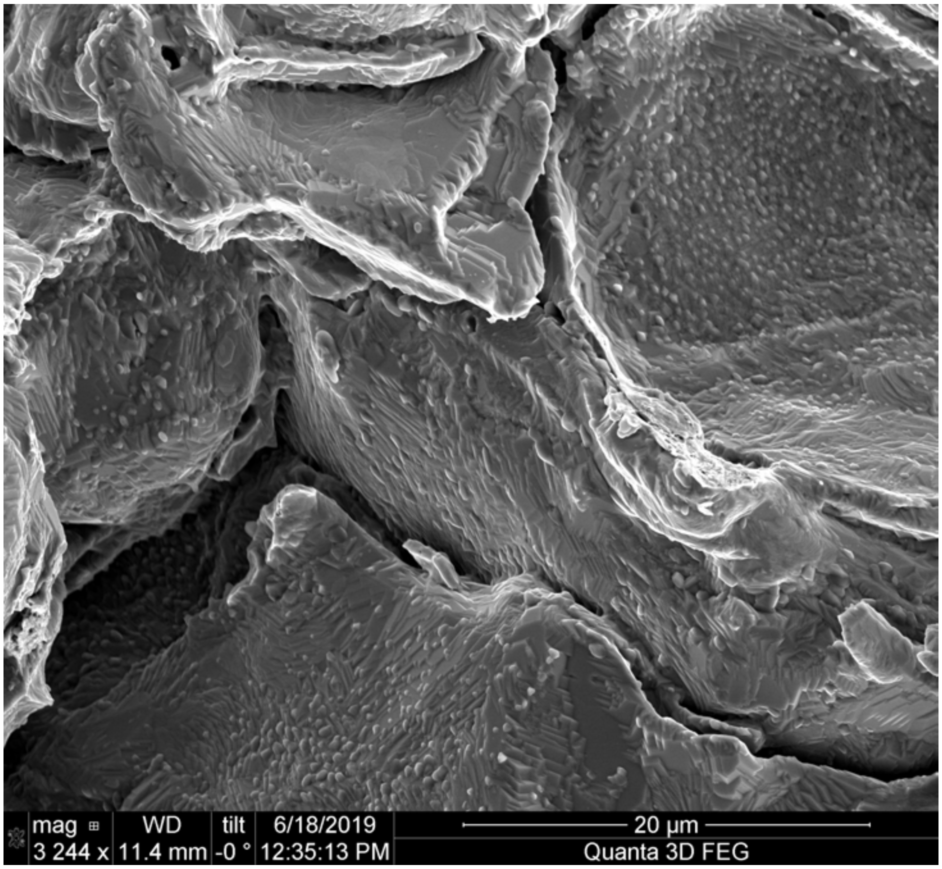

(c) A significant magnification of 1000° C ring 2, showing the same angular, stair-step morphology as (b).

Figure 4.25: Micrographs of the break surface on two of the ring tensile test samples, showing differences in surface morphology.

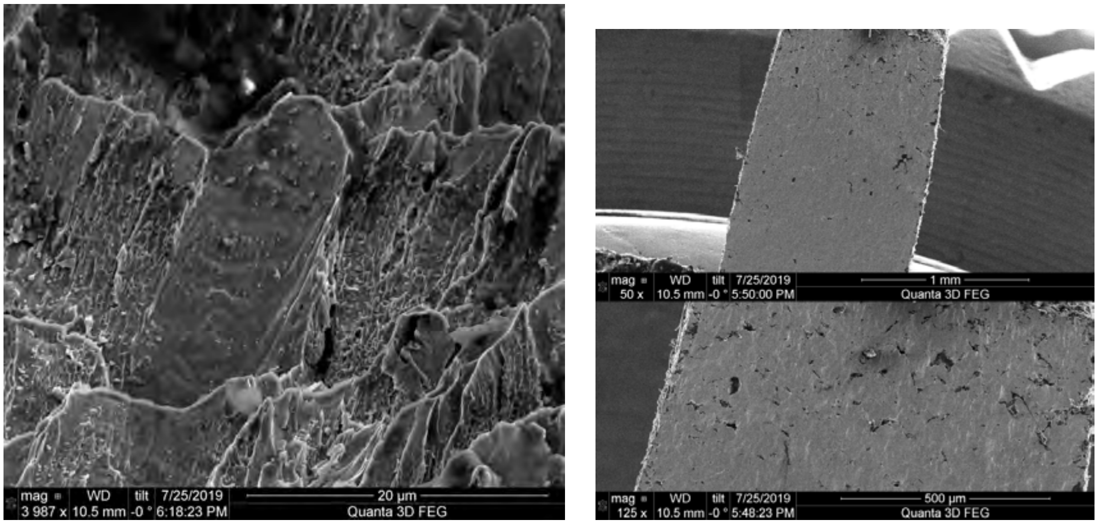

(a) The fracture surface of the sample, showing signs of ductile flow surrounding a less deformed surface.

(b) Though it showed ductility in the test, these local imperfections are distinctly cracks which have opened up.

Figure 4.26: The 1100° C V3 bar was examined following destructive tensile testing.

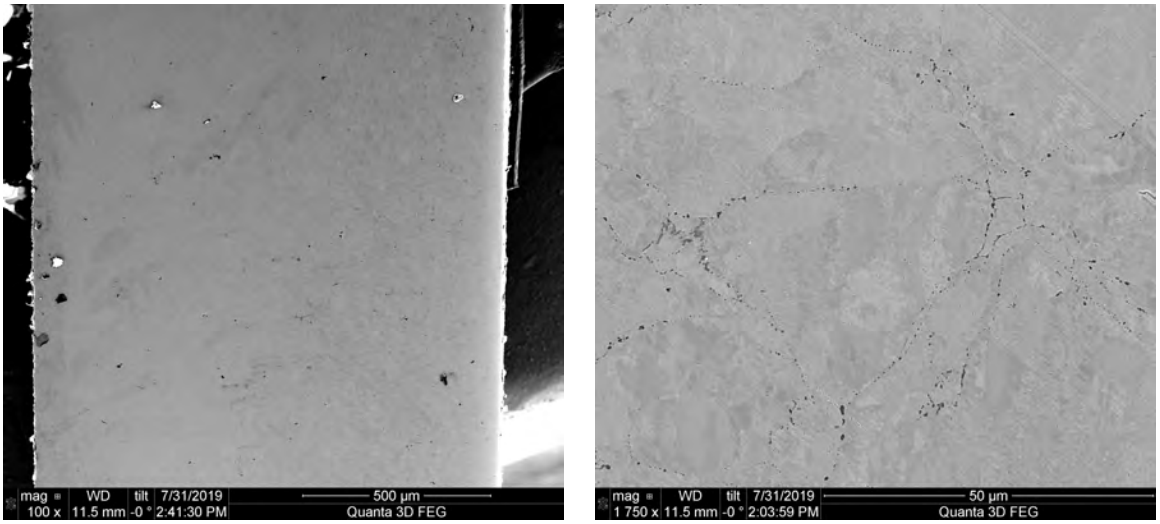

(a) (b)

Figure 4.27: These images are of a part of the 1100° C V3 bar that was not stretched, and which does not show the rifts or other openings that developed in the sample, as shown in fig. 4.26b. Though the surface in (a) looks well consolidated, upon closer inspection (b) indivdiual lines of porosity may be seen, presumably between the particles that impacted during the spray process.

4.6.0.3 Hot Isostatic Pressed SSJ2

In an effort to improve consolidation and material properties thereby, a unit of 1100° C heat-treated 14YWT was commercially hot isostatically pressed (HIPed) with the following conditions: 1121 ± 14°C, 15000 ± 500psi, 4hours (+15, -0 min). Upon the piece's return to Berkeley, it was cut into SSJ2 bars by wire EDM and polished to 2400 grit before being tested. The raw data of these fits is shown in fig. 4.28. On average, the bars were strained 27.1 ± 4.0% when they fractured. The yield stress of the samples was 372.9 + ±67.1 MPa.

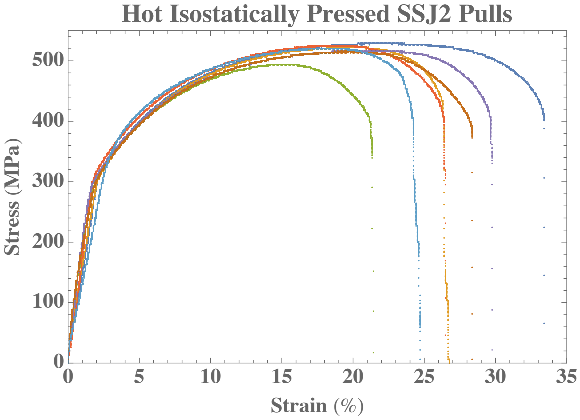

Figure 4.28

Micrography and EDS data were also taken for the HIPed specimen, illustrated in fig. 4.29. Though the SEM image is not high-contrast, it does show that the bimodal grain morphology seen in other heat treatments has persisted. Likewise, it shows that the cracks present in previous micrographs have not closed. The EDS does show bright spots of titanium in an otherwise generally flat field. Comparing the crack pattern in the SEM image, it is apparent that the brightest spots are associated with them. It is possible that Ti has migrated to the surface, but recall fig. 3.4, which shows the emission depths of various signals. The characteristic X-rays picked up in EDS are generated at a much greater depth than the secondary electrons imaged. It follows that all of the surfaces within the crack can be a source of characteristic x-rays—much more emission area inside than on the surface of the sample—and so appears much brighter where the electron image appears dark.

4.7 Internal Cracking and Bonding

Owing to the results above, experiments were conducted to further examine the degree of bonding or inhibition to bonding within the sample by progressive etchings. Using Kaling's II etchant on a nanoindented, 800° C heat treated, free-standing piece, optical microscope images were taken at successive time steps. Sequences of these images are shown in fig. 4.30. The presence of the nanoindentaions serve as in-image reference points.

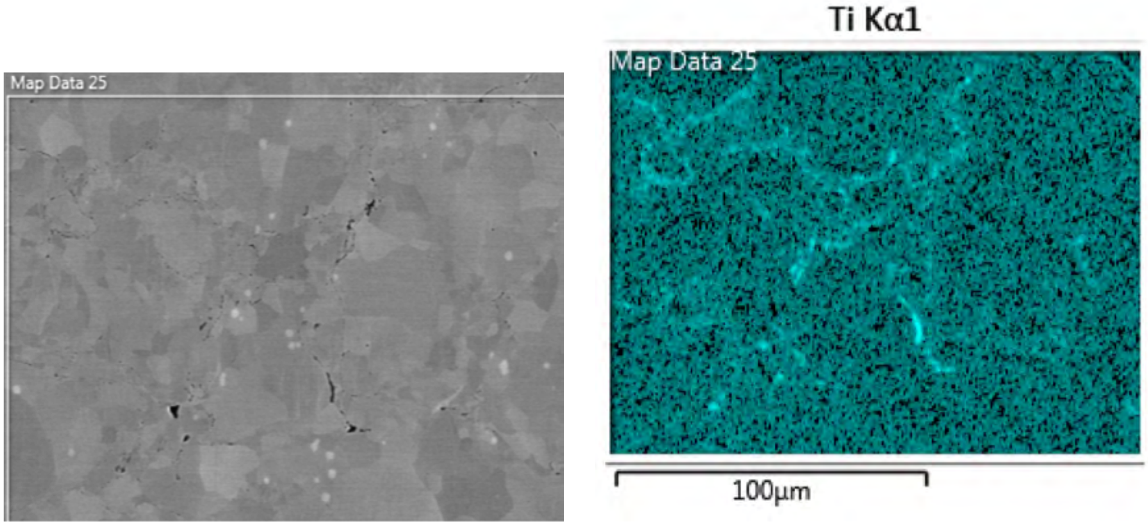

(a) (b)

Figure 4.29: Scanning electron microscopy of the HIP'ed 14YWT sample.

The images show that the etchant has penetrated into the cracking and other areas preferentially, and eaten away at the metal in those areas. The difference between the pristine (0s) etching and 12s suggests both the cleaning of the surface from imperfections remaining after the polishing process, but has also revealed cracks in the surface where etchant has been able to penetrate more rapidly. The difference between 12s and 25s is especially noticeable, regions having opened up and individual pits having apparently gotten deeper. The trend continues throughout the image sequence, with lands and valleys developing by 32s and being fully evolved by 50s.

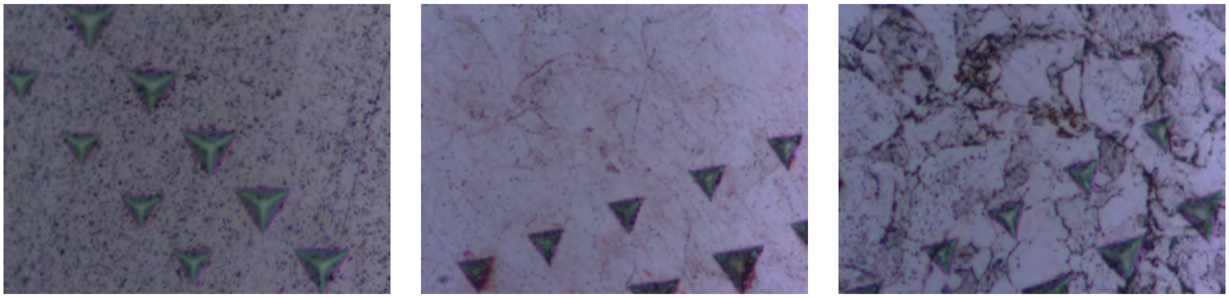

(a) 0 seconds (b) 12 seconds (c) 25 seconds

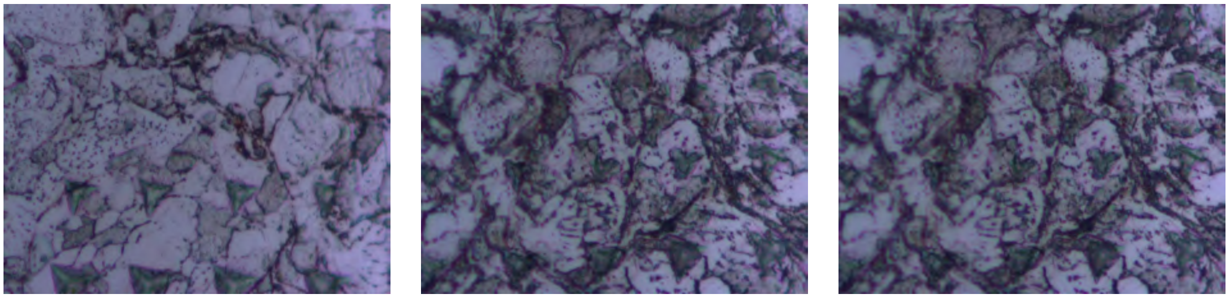

(d) 32 seconds (e) 50 seconds, 1st focal depth (f) 50 seconds, 2nd focal depth

Figure 4.30: Successive etchings of an 800° C surface with Kaling's II etchant at 100x magnification.

Chapter 5

Discussion

5.1 Representative Properties of Hot Extruded 14YWT

Kim *et al.* have performed relevant tensile tests of extruded 14YWT ([81, 28]) using material from Hoelzer's 14YWT SM10 batch. This sample was extruded on at 850°C, the original media having been formed by ball milling in a Zoz CM08 [1]. The samples produced showed nearly brittle behavior at room temperature, with a total elongation of 2.4%, and only 0.7% uniform. Of particular interest in this work was their observation of dimpling on the fracture surface, which was morphologically quite similar to some of the fracture surfaces imaged in this study, e.g. those shown in fig. 4.26a. However, none of their images show the crystallographic cleavage surfaces shown in fig. 4.25c. This may be in part related to the difference in tests, as the cleavage planes were only observed in the ring tensile tests conducted in this study, and which were not present in [81]. Whether such a difference in loading can be solely responsible for an absence of ductile motion remains unsettled, however.

He *et al.* performed an estimated 200 dpa irradiation on hot extruded 14YWT, and preparatory to this they performed an excellent characterization of the grain morphology and nanocluster size and distribution, part of which may be seen fig. 5.1 [56]. Their results report number densities with a lower bound of $1 \times 10^{23}\,\mathrm{m}^{-3}$, with particle sizes from 1 to 20 nm. This work notes, however, that the size distribution of particles was peaked below 1 nm for all the samples shown, with long tails. The average size in all cases was on the order of 1 nm.

Some work done on ODS alloy PM2000 can be used as a comparison for the behavior of oxide particle development. It is true that the oxide particles formed in the system are Y-Al-O rather than Y-Ti-O, and that the diffusion constant of Al in ferrite is many orders of magnitude greater than that of similarly dissolved Ti. [7, 22] That said, the kinetics of the Y-X-O phase will still be rate-limited by the diffusion of the yttrium atoms. It follows that order of magnitude of nanoparticle formation numbers, for given heat treatment temperatures and durations, may be obtained by considering this system. Dawson *et al.*

([39]), in particular, examined mechanically alloyed powders—not consolidated, that is—after various heat treatments. Those most aligned with this study were their explorations at 850 and 1150° C. The latter produced grains as large as 10 μm, though a plethora of fine grains were observed in small pockets. This residual fine structure may be related to the almost bimodal distribution of particle sizes found in the spray formed and heat treated samples of this study, e.g. fig. 4.13c, in that intense mechanical deformation followed by heat treatment, but without further strain were both employed in these processes. A further observation, which may prove helpful later, is that while there was, for their 850° C, 1 hour heat treatment, preponderance of nanoscaled oxides at $8 \times 10^{23}\,\mathrm{m}^{-3}$, there was also a significant density ($\approx 10^{19} - 10^{20}\,\mathrm{m}^{-3}$) of particles larger than 10 nm. Such particles may serve as thermodynamically favorable sites for additional growth and the loss of the small nanoparticles desired in an ODS alloy. Their work also performed series of hardness measurements in the Vickers micro-hardness scale. These results can be converted to the reduced modulus employed in this study through a simple conversion $VH = 94.5H$ ([84, 44]), where H is the nanoindentation-measured hardness in GPa.

Alam, Pal, Maloy, and Odette provide useful information pertaining to hot extruded 14YWT ([8]), first annealed at 850° C for one hour and subsequently extruded at 1000° C. Their tensile test data is directly comparable, particularly at 23° C. For completeness, it should be noted that some of the data employed in that paper came from [37] and is therefore cited independently.

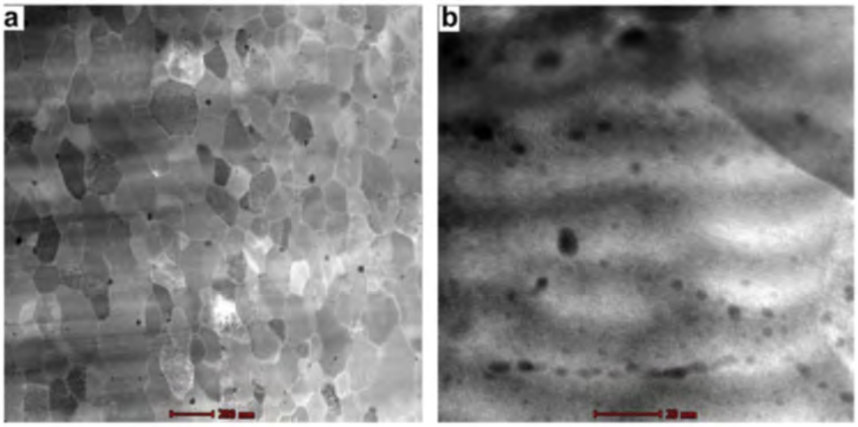

Figure 5.1: Two images of extruded, unirradiated 14YWT: (a) grain structure; (b) HAADF-STEM illustrating nanoclusters. From [56].

[127] measured a ferritic ODS alloy denoted J05, which contained 13.65% Cr, 1.17% W, well as carbon, nickel, and the yttrium and titanium oxides necessary to form the nanoparticles. For a complete breakdown see table A.10. Their samples were created mechanical alloying and hot extrusion at 1100° C. The alloying materials constitute a significant difference between J05 and 14YWT, particularly the significantly reduced proportion of tungsten,

as well as the incorporation of nickel and manganese. Nonetheless, as an ODS alloy it is a material of legitimate comparison to the 14YWT studied in this work. Thee authors report fine grains of 1.2μm length and 550 nm width on average, and a dispersion of nano-oxides on the order of $5 \times 10^{22}\,\mathrm{m}^3$. The yield and ultimate tensile strength values were anisotropic, ranging from slightly above 1 GPa to nearly 1200 GPa at room temperature; likewise, the authors of that work observe that the ductility in the direction of extrusion was twice that of the ductility transverse.

Aydogan *et al* produced an interesting duo of papers ([18, 19]) most relevant to this work in that it employed gas atomization as the source of its feedstock before employing either oxy-fuel deposition in combination with hydrostatic extrusion, or a conventional hot extrusion to consolidate the final bodies. With reference to their data cited in table A.12, the former is denoted process 1 and the latter process 2. Process 1 is particularly interest with respect to this work as it employed a spray process, albeit at significantly higher temperatures and followed by an extrusion step. Nonetheless, aspects of the impact and shear deformation that occur are of relevance and its results may be regarded as somewhat corroborative.

5.2 Direct comparison of properties

5.2.0.1 Grain Size and Distribution, and Orientation

The presence of possible texture within the cold-sprayed samples brooks some discussion. It was particularly observed in the 800° C heat treatments—see figs. 4.14b and 4.15a, but not in the same orientation. Furthermore, upon greater heating, all evidence of texture was erased, as evinced by figures 4.15b and 4.14c. The idea that these are statistical oddities is not greatly creditable and, in any case, not spoken to by the evidence in either direction, but an examination of the EBSD maps, combined with the understanding that the material upon deposition is exceptionally disordered, does suggest that small grains of random orientation and high disorder are being obscured by slightly larger grains of much greater order. A matter of signal strength, in fact. When the system is allowed to anneal more effectively at the higher temperatures, all the grains can show their diffraction patterns more easily, and the artificial existence of texture disappears.

It follows that cold spray, as might be expected from a highly random process, produces a texture-free body. It is not altered in this by the presence of the substrate, either. In this respect, its properties are expected to be isotropic throughout the formed body, so that phenomena such as ductile-to-brittle transition will be consistent throughout. This is also expected to minimize the creep motion of the material, as dislocations will be impeded in their transmission. As such, the texture properties of cold-sprayed 14YWT are held to be favorable with respect to conventionally extruded 14YWT.

The size and distribution of ferrite grains in the heat-treated bulk, however, is not favorable to cold-spraying. One consideration is that the distribution of grain sizes shown by EBSD in fig. 4.13d is actually far less homogenous than originally anticipated. This is not a limited event, and the evidence of the substrate-supported samples indicates that a substantial proportion of the grain boundaries are high-angle ($> 10°$) which tends to imply a high interfacial energy (bearing in mind that, given the periodic nature of crystals, occasionally a high-angle grain boundary will come into a brief zone of good registration with commensurately lower boundary energy). Such boundaries are much more likely to fracture than low-angle grain boundaries, so that their presence must be considered deleterious toward the spray formed material's fracture toughness. [118] In conjunction with this, the smaller grains are not uniformly distributed amongst the large grains, as shown by fig. 4.13c, but rather exist in contiguous regions surrounding them. A little thought suggests an explanation for this: the periphery of the sprayed particles undergo the greatest deformation and so is replete with nucleation sites for small grains, while the interior can be dominated by the grains that were principally present before deformation. (e.g. fig. 4.6). It follows that the regions of small grains may be regarded as contiguous in any spray-formed body after heat treatment. Such small grains have a propensity to allow fractures to propagate around them. It is therefore assessed that spray-formed ODS alloys will have unfavorable fracture toughness behavior in all directions. For comparison, similar concerns about delamination toughness in hot-extruded ODS alloys have been explored [11, 28]: in those cases, the alloys explored showed highly unfavorable fracture toughness for reasons akin to those above, but primarily in one direction. This work therefore concludes that the microstructure of spray-formed 14YWT compares unfavorably with the more conventionally consolidated alloy.

5.2.0.2 Nanoparticles

The spray formed 14YWT in this study performed uniformly poorly as compared to the more customary process of mechanical alloying and hot extrusion. Chief among its failings is the absence of nanoparticles and associated properties. This is shown forcefully by the absence of $Y_2Ti_2O_7$ diffraction peaks in the XRD data presented, and corroborated both by the lack of visible particles in the HRTEM images with respect to the discussion of sec. 4.2, and further corroborated by the low hardness of the material shown in sec. 4.5. Nanoparticles, with their ability to improve creep behavior and radiation tolerance, are the entire basis of the desirability of nanostructured ferritic alloys of the 14YWT form; without them, one would be just as well served to employ a steel of significantly less involved manufacture.

That said, the gas atomized feedstock powder is reported to have had indications of nanoparticles in the beginning, if not uniformly distributed [89]. Whither the particles, then? This work speculates that the intense generation of dislocations during the impact, combined with both the immediate adiabatic heating, serve to dramatically enhance the diffusion of the dissolved yttrium and titanium species within the matrix, thereby precipitating out $Y_2Ti_2O_7$ as particles much larger than the nano-scale sought. While the experiments conducted in the work do not show this, an argument for the possibility can be made as follows.

First, it is well established that the presence of cold work and other damage events can enhance diffusion, as can local heating by providing more activation energy [99, 38, 22]. In the case of high-pressure torsion in the Al-Cu system, [73] has observed that the diffusion coefficient is enhanced by a factor of 10^{12} to 10^{22}, which it attributes principally to increased numbers of lattice defects. [105] and [63] have likewise observed that intense strains from high-pressure torsion and equal-channel angular extrusion, respectively, led to enhanced precipitation of Cu from a well-mixed Al-Cu system. Of particular interest is that both sets of experiments emphasize strain over strain rate, which is an important distinction between their work and cold-spray. Of perhaps the greatest relevance to this work is the recent publication of [101], which found that with strains not exceeding 0.2, self-diffusion in nanocrystaline iron was enhanced between 10 and 80 times. This work therefore speculates that the strain rates found in cold-spray impaction, as great as $10^{9}\,\mathrm{s}^{-1}$ [121], may have a powerful precipitating effect on nano oxides. This will be explored more fully in a later work, as it would serve to condemn the cold spray process for the manufacture of ODS alloys.

5.2.1 Hardness and Reduced Modulus

By the data collected in table A.11, the hardnesses of samples produced by cold spraying are generally 1 GPa (94.5 HV) softer than other ODS alloys, the only exception being the 14YWT produced by the oxy-fuel deposition process explored in [18]. The value of hardness, especially when concerned with fretting and other wear processes to which cladding tubes are subjected, has been discussed in sec. 2.3. This, incidentally, corroborates the finding of sec. 5.2.0.2, in which a distinct lack of nanoparticles was observed. The fact that the hardness in this case does happen to be higher than the hot-spray formed process, though that material did have a greater compliment of nanoparticles, must, therefore, be addressed. One possibility is that the increased hardness in the cold-spray body is not from the Orowan mechanism, as would be the case for a high nanoparticle density, but rather from Hall-Petch hardening due to the proportion of smaller grains throughout the body. An examination of some of the micrographs in [18] casts doubt on—though does not disprove—this supposition. Another possibility, possibly acting in conjunction with the previous consideration, is that the cold-work imparted to the cold-sprayed material very probably was not totally annealed out of the system during the heat treatment. As a matter of comparison, this hardening mechanism would have been prevented by the oxy-fuel deposition method.

As to the reduced modulus, few, if any, papers deigned to publish it; presumably it was not so different from commonly available measures of steel as to lack notoriety in the limited space of journals. The primary source of comparison is [84], which showed 14YWT with reduced moduli ranging from $212.8 \pm 6.6\,\mathrm{GPa}$ when indented to 200nm, and $215.1 \pm 17.3\,\mathrm{GPa}$ when indented to 500nm. The reduced modului found in this work were, in general, slightly higher, though of significantly standard deviation, e.g. $238.6 \pm 12.8\,\mathrm{GPa}$ for 800° C heat-treated, free-standing samples and $216.3 \pm 13.3\,\mathrm{GPa}$ for 1100° C treated, free-standing samples. Consequently, a part made from sprayed 14YWT would be expected to have the same response under less-than-yield-stress load, on average, as a non-sprayed part. The larger variability in this value from cold spraying, however, is not its favor. Such variability requires more conservative—robust—design to guarantee that the wider distribution will still not permit escape from the design space.

The results of the irradiation show that the sample was susceptible to radiation hardening at 350° C, more than doubling following an estimated 20dpa of ion damage. Insofar as nanoparticles, the principle source of radiation tolerance proposed for this material, were not observed, this cannot be considered evidence against the underlying premise of ODS alloy radiation hardness. It does imply, however, that cold sprayed ODS alloys need additional refinements to their process if they are to be resistant to embrittlement at extreme irradiation damage.

5.2.2 Yield and Ultimate Tensile Strength

The most cursory examination of table A.11 shows a deeply disappointing showing from the cold-sprayed body, with a σ_{yield} approximately one-third that of more traditionally formed ODS alloys, while its σ_{UTS} fared, if anything, less well. Consideration of the SEM images of the body before (fig. 4.27a) and after (fig 4.26b) tensile testing provides the smoking gun to explain this: the material has not bonded effectively at all points throughout the material, and in fact regions preferentially pull apart in a manner reminiscent of expanded steel mesh. Such a supposition is supported by the yield and UTS strains measured in this study: the bending of different parts of the material allowed for a deformation that would not have been possible under more effectively consolidated parts. This is further corroborated by the corrosion study performed using Kalling's II reagent, which illustrated the presence of incomplete joins in the material, which allowed the etchant to penetrate preferentially. Finally, the barriers to improved consolidation appear to be more sturdy than the pressures employed in the sample HIPing could overcome, as cracks in the surface persisted—lines of stress rising and weakness which will have to be overcome in a production process.

If it were reasonable to consider recalculate the stress and strain curves using only the area of the proportion of the tensile bar cross-section which were, in fact, well-bonded, it might occur that the yield strength was on par with other consolidation methods. This, however, is not reasonable from the perspective of the final use case: the mass and cost of the finished part do not get a dispensation for the internally unbonded area. If only $1/x^{\text{th}}$ of the cross-sectional area is actually bonded and providing structural support, the whole part must be of x times greater cross-section—with cascading impacts as the mass and cost of the part increase, the volume to contain it increases, as it becomes more susceptible to differential thermal stress.

Chapter 6

Conclusions and Future Work

The irretrievable conclusion of this work is that, on its own, cold spraying is not currently a suitable mechanism for consolidating ODS feedstock into a final product. As discussed in the previous chapter, the process produced bodies that were vastly weaker, were brittle in application, and were evidently absent the nanoparticles which alone are the motivation for pursuing such steels. While the process does have an advantage in that it creates parts of isotropic grain structure, this is hardly a satisfactory recompense for its shortcomings in other important respects.

That sound, metallic bonds can occur as a result of cold-spryaing material is not in doubt, as sections have been displayed in which ductile failure occurred. The sections which do not bond must be significantly reduced, however, before cold-sprayed parts can be considered for possible additive manufacturing employment. It is very probable that surface oxidation and other impurities were present on the surface of the powder and that these contributed significantly, perhaps decisively, in preventing uniform metallic bonding. It follows that the next steps in creating a workable metallic cold-spraying procedure are, first, to develop a reliable and efficient method of thoroughly cleaning oxides, oils, and other contaminants from the surface of every particle of feedstock, and second, working out a procedure by which this pristine surface is retained throughout the spraying process. The use of thorough cleaning may also, by reducing the amount of plastic deformation the sprayed particles must undergo to achieve a bond, expand the window of acceptable particle spray parameters.

Whether, too, changes could be made to the feedstock production itself is an open question. To reiterate an earlier point, feedstock must be soft enough to deform easily when impacting during the cold spray process, and must possess a morphology that allows it to flow easily through a spray nozzle. The use of cryogenic milling, in which the ductility of the feedstock is suppressed, is expected to create feedstock material of smaller dimensions, greater sphericity for improved nozzle flow, and with the proven mechanical solvation of the yttria and titania; combined with appropriate cleaning, this could enable efficient deposition of metal at lower strain rates. This, in turn, could mitigate concerns raised about the precipitation of nanoparticles under high strain conditions. It also brooks consideration that, if a conjunction of events occurs—an adequate body is created directly from cold spraying, the feedstock mean size is small enough to create a strain distribution throughout the material, and high strain rates give rise to increased rates of diffusion—that subsequent heatings to precipitate the required nanoparticles could be minimized or even omitted.

There is no denying that the materials produced in the work were not as functional as had been hoped. What has been learned, however, is sufficient to illustrate what the new questions are, and what experiments undertaken in order to make progress. There is much work to do: this is not the end of cold spray research into ODS alloys—only, perhaps, "the end of the beginning." [35]

Appendix A

Data Tables

A.1 Grain Size and Distributions

Area (μm^2)	d (μm)	Aspect ratio	Border grain
1.7688	1.5007	5.2688	edge
1.608	1.4309	2.7343	no
4.5024	2.3943	1.928	no
3.3768	2.0735	4.5932	no
1.608	1.4309	10.148	no
2.0904	1.6314	3.6304	no
2.0904	1.6314	7.0428	no
2.7336	1.8656	2.2777	no
3.0552	1.9723	2.5787	no
1.9296	1.5674	1.749	no
8.04	3.1995	1.3339	no
1.7688	1.5007	2.4849	no
3.216	2.0236	2.4746	edge
1.7688	1.5007	2.8949	edge

Table A.1: Numerical results of attempting EBSD on the substrate-supported, unheated 14YWT surface shown in fig. 4.5. The vast majority of the points scanned—78%—had no solution. This is further evidence of the extreme deformation of the material in the sample.

A.2 Nanoindentation

Max. Depth (nm)	Plastic Depth (nm)	Max. Load (mN)	Hardness (GPa)	Er (GPa)
419.776	396.015	15.5413	2.38533	170.317
415.889	385.411	16.9313	2.72647	148.169
421.509	399.401	17.4606	2.6398	204.115
422.566	400.672	17.7841	2.6736	209.342
427.479	403.282	15.8981	2.36269	168.357
435.121	409.317	15.5919	2.25687	152.796
437.023	419.978	16.764	2.31803	243.085
441.57	423.132	19.8036	2.70205	263.695
449.009	425.37	19.8814	2.68727	205.521
447.261	429.601	18.6098	2.47137	255.234
452.925	434.894	18.9724	2.46501	252.078
460.257	437.08	17.1545	2.20892	176.533
467.899	450.12	18.4328	2.25183	240.854
477.588	460.857	18.3449	2.14824	249.39
487.208	464.434	18.7692	2.16759	186.153
489.425	470.242	19.7778	2.23357	230.292
495.293	477.119	21.4846	2.3637	260.616
501.388	475.054	22.4871	2.49341	188.994
510.549	483.677	20.2944	2.17846	164.465
526.995	505.966	22.118	2.18849	219.901
555.964	533.229	22.2704	2.00331	195.27
585.676	563.125	29.7168	2.42004	249.949
668.398	644.012	36.8218	2.34353	253.199
687.778	657.839	38.8701	2.37871	213.473
738.15	705.866	43.0435	2.3117	205.371
		Mean	2.375	212.29
		Std. Dev.	0.195	36.294

Table A.2: Nanoindentation results for the substrate-supported 800°C samples, derived from the hysteresis curves presented in fig. 4.18a using the MicroMaterials analysis software.

Max. Depth (nm)	Plastic Depth (nm)	Max. Load (mN)	Hardness (GPa)	Er (GPa)
407.449	394.53	14.6036	2.25637	295.337
413.821	398.968	12.4224	1.8817	216.35
414.264	394.134	15.8752	2.45721	206.229
419.067	406.01	14.5746	2.14023	284.309
423.366	410.305	13.449	1.93836	259.836
430.039	416.703	15.1292	2.12133	282.361
434.834	419.532	14.905	2.06487	240.98
437.36	415.254	15.6309	2.20532	176.532
447.174	428.421	14.03	1.87234	181.66
459.322	438.365	14.9555	1.91568	169.761
462.18	439.732	15.4014	1.96185	162.761
464.973	444.948	18.7649	2.34036	219.967
478.344	462.504	17.4882	2.03484	250.305
489.61	464.559	20.2773	2.34063	182.786
498.881	479.513	18.8025	2.05003	213.06
500.497	476.183	23.3112	2.57375	211.744
508.874	488.963	20.2965	2.13635	219.809
514.396	499.355	19.412	1.96703	273.065
517.224	497.38	19.7879	2.01955	211.734
518.451	494.13	22.991	2.37443	201.922
525.44	502.711	20.2724	2.02945	187.574
526.19	500.853	21.9202	2.20917	182.547
532.799	514.001	21.493	2.06677	235.657
536.686	514.694	24.0201	2.30414	224.836
546.781	528.061	26.2976	2.40784	282.532
574.087	554.145	24.9449	2.09195	240.781
575.994	551.699	22.9554	1.94071	182.605
580.525	556.124	23.9074	1.99194	187.982
585.098	561.969	25.108	2.05241	206.291
585.049	564.131	26.4296	2.14533	239.271
595.881	569.154	25.2922	2.02001	177.754
615.488	590.296	27.3939	2.04649	197.549
601.527	579.885	27.2996	2.10706	232.928
608.543	587.366	25.5753	1.92814	220.41
621.106	590.968	28.8938	2.15405	173.987
		Mean	2.11851	218.092
		Std. Dev.	0.17307	36.4668

Table A.3: Nanoindentation results for the 4130 substrate 1000°C samples, derived from the hysteresis curves presented in fig. 4.18b using the MicroMaterials analysis software.

Max. Depth (nm)	Plastic Depth (nm)	Max. Load (mN)	Hardness (GPa)	Er (GPa)
1013.11	983.488	67.6665	2.85542	311.917
1030.6	996.237	70.4877	2.89883	276.467
1053.85	1018.06	73.5807	2.89769	271.186
1146.35	1108.91	86.4601	2.86982	279.647
1223.88	1181.36	94.32	2.75851	252.127
1294.2	1247.16	107.957	2.83295	247.116
1341.29	1293.03	110.585	2.69969	237.978
1367.41	1316.89	119.795	2.81952	241.777
1392.92	1337.2	122.198	2.78935	220.243
1418.06	1365.72	119.348	2.61172	224.197
1631.55	1570.24	159.26	2.63639	222.151
1706.43	1642.94	171.915	2.59959	221.295
1845.67	1777.94	204.871	2.64532	228.449
1941.59	1872.77	223.805	2.60457	233.156
		Mean	2.751	247.693
		Std. Dev.	0.115	26.612

Table A.4: Nanoindentation results for the free-standing 800°C samples, corresponding to the blue curves of 4.19b using the MicroMaterials analysis software.

Max. Depth (nm)	Plastic Depth (nm)	Max. Load (mN)	Hardness (GPa)	Er (GPa)
1072.79	1030.58	82.3627	3.16518	254.272
1242.53	1192.42	109.29	3.1373	245.593
1315.11	1263.41	121.721	3.11251	250.257
1433.27	1378.09	141.53	3.0418	249.924
1458.14	1402.03	141.846	2.94536	242.103
1483.57	1424.31	145.358	2.92457	231.267
1508.05	1446.71	151.189	2.94846	228.748
1535.45	1470.93	152.553	2.87785	215.851
1556.16	1493.39	160.28	2.93337	229.589
		Mean	3.010	238.623
		Std. Dev.	0.106	12.848

Table A.5: Nanoindentation results for the free-standing 800°C samples, corresponding to the red curves of 4.19b using the MicroMaterials analysis software.

Max. Depth (nm)	Plastic Depth (nm)	Max. Load (mN)	Hardness (GPa)	Er (GPa)
1256.52	1209.32	94.079	2.6257	221.300
1306.60	1261.28	98.453	2.5261	231.269
1554.86	1492.59	135.823	2.4884	196.231
1655.26	1595.42	155.078	2.4868	218.128
1704.96	1639.32	163.141	2.4778	203.598
1850.81	1783.88	188.866	2.4225	212.414
1951.51	1886.90	210.154	2.4092	231.501
		Mean	2.491	216.349
		Std. Dev.	0.072	13.308

Table A.6: Nanoindentation results for the free-standing 1100°C samples, derived from the loading-unloading curves presented in fig. 4.19a using the MicroMaterials analysis software.

A.3 Tensile Testing

Temp.	Ring No.	Height (mm)	Elongation (μm)	Force (N)	Elongation (μm)	Force (N)
800°C	1	2.304 ± 0.097	82.3	232.2	92.6	243.8
800°C	2	2.612 ± 0.032	239.5	1247.4	342.9	1607.6
800°C	3	1.711 ± 0.029	64.4	224.3	66.7	227.9
800°C	4	3.143 ± 0.034	65.2	275.1	77.5	305.9
1000°C	1	1.703 ± 0.035	76.3	334.3	82.9	350.0
1000°C	2	1.834 ± 0.053	115.2	294.2	136.7	316.6
1000°C	3	1.528 ± 0.034	98.0	214.7	112.0	229.9

Table A.7: Raw data for the ring-pull experiments.

Temp.	Ring No.	ϵ_Y (%)	σ_Y (MPa) Simple	σ_Y (MPa) Derived	ϵ_{UTS} (%)	σ_{UTS} (MPa) Simple	σ_{UTS} (MPa) Derived
800°C	1	0.711528	48.979	18.1267	0.800528	51.4259	19.0323
800°C	2	2.06948	232.134	85.9108	2.96248	299.165	110.718
800°C	3	0.558856	63.7245	23.5839	0.578856	64.7472	23.9624
800°C	4	0.566796	42.5469	15.7462	0.673796	47.3104	17.5092
1000°C	1	1.53531	95.4249	35.3159	1.66731	99.9064	36.9745
1000°C	2	0.995107	77.9742	28.8576	1.18111	83.911	31.0547
1000°C	3	0.847875	68.2773	25.2688	0.968875	73.1111	27.0578

Table A.8: Stress and strain values for the ring-pull tests.

Sample	Yield Strain (%)	σ_{Yield} (MPa)	UTS Strain (%)	σ_{UTS} (MPa)
800° C V1	5.23951	433.477	7.55951	473.712
800° C V2	3.34443	398.443	6.32043	493.537
800° C V3	3.25815	444.764	6.53815	555.145
800° C V4	3.6629	389.641	6.6509	460.054
800° C V5	3.45085	453.296	5.69885	528.28
800° C V6	3.17701	413.035	5.45701	500.079
800° C H1	3.561	407.529	8.447	529.846
800° C H2	3.05693	365.304	4.75093	426.678
800° C H3	2.78005	340.826	5.72005	459.015
800° C H4	2.73109	333.692	6.12109	446.52
1100° C V1	1.98581	299.182	12.1338	495.818
1100° C V2	2.22712	362.652	21.6331	604.029
1100° C V3	2.30441	341.871	22.0764	572.605
1100° C V4	2.10923	293.918	8.73923	439.157
1100° C V5	2.16299	388.481	20.275	648.22
1100° C H1	0.849965	176.346	18.782	436.344
1100° C H2	0.525499	141.257	19.6375	436.888
1100° C H3	1.53898	411.086	19.529	650.316
1100° C H4	2.42226	396.982	20.3343	645.814

Table A.9: Stress-strain points for the curves shown in figures 4.24a and 4.24b. The yield stress was calculated according an 0.02% offset to a line fit to the linear portion of each stress-strain curve; the UTS is taken from the maximal point on the system.

A.4 Comparison Properties

Alloy	Fe	Cr	W	Ti	Y	O	C	Si	Ni	Mn	Al	Mo	Cu
J05	Bal.	13.65	1.17	0.30	0.26	0.06	0.05	0.27	0.16	0.33	0	0	0
PM2000	Bal	19	0	0.5	0.4	0.1	0	0	0	0	5.5	0	0
MA957	Bal	13.57	0	0.98	0.20	0.05	0.02	0.03	0.10	0.07	0.09	0.30	0.01
ODM401	Bal	13.6	0	0.85	0.20	0.05	0.007	0	0	0	0.06	0.29	0

Table A.10: Various ODS alloy compositions in wt.%.

Alloy	H (GPa)	E_r (GPa)	σ_{yield} (MPa)	ϵ_{yield} (%)	σ_{UTS} (MPa)	ϵ_{UTS} (%)	Ref.
J05	-	-	1050-1150	-	-	-	[127]
14YWT	-	-	1600	-	1749	-	[81]
14YWT	-	-	-	-	-	-	[56]
14YWT	-	-	1042 ± 102	3.8 ± 3.7	1133 ± 100	12.9 ± 1.5	[8, 37]
14YWT (Proc. 1)	1.872 ± 0.056	-	612 ± 18	-	1133 ± 100	12.9 ± 1.5	[18]
14YWT (Proc. 2)	3.801 ± 0.119	-	1242 ± 39	-	-	-	[18, 19]
14YWT	5.24 ± 0.92	182.8 ± 29.3	1635 ± 7	0.1 ± 0.1	1800 ± 20	0.8 ± 0.1	[84]
MA957	3.40				1035 ± 3		[98]
MA957			840 (L-R), 900 (C-R), 950 (C-L)			18.0 (L-R), 8.5 (C-R), 6.0 (C-L)	[11]
ODM401	3.8 ± 0.1			-			[54]
800° C Substrate	2.38 ± 0.19	208.96 ± 39.40					This work
1000° C Substrate	2.12 ± 0.17	218.09 ± 36.47					This work
800° C Free	2.75 ± 0.12, 3.01 ± 0.11	247.69 ± 26.61, 238.62 ± 12.85	396.63 ± 38.28	3.37 ± 1.42	487.29 ± 39.50	6.31 ± 1.65	This work
1100° C Free	2.49 ± 0.07	216.35 ± 13.31	300.89 ± 83.13	1.54 ± 1.10	570.60 ± 88.88	20.23 ± 1.45	This work

Table A.11: Hardness, modulus, and tensile strength data of 14YWT and other ODS alloys found in other works.

Alloy	NP size (nm)	ρ_N (m^{-3})	Grain size (nm)	Texture	Ref.
J05	2.3	5×10^{22}	1200×550	Strong $\langle 110 \rangle$	[127]
14YWT	$17 - 31$	-	$136 \pm 14\%$	-	[81]
14YWT	1.1	$\sim 1 \times 10^{24}$	100-300	-	[56]
PM2000	2.1 ± 0.7	5×10^{23} (950° C, 1hr)	10×300	-	[39]
14YWT	2.4	4.8×10^{23}	$580 \pm 480 \times 640 \pm 230 \times 1560 \pm 840$	Strong $\{001\}\langle 110 \rangle$	[8, 37]
14YWT (Proc. 1)	7.2 ± 1.5	$2.3 \pm 0.4 \times 10^{21}$	1970 ± 104	Strong $\{001\}\langle 110 \rangle$, $\{111\}\langle 110 \rangle$	[18, 19]
14YWT (Proc. 2)	2.8 ± 0.7	$4.3 \pm 0.7 \times 10^{23}$	49 ± 50	Strong $\{001\}\langle 110 \rangle$ Weak $\{111\}\langle 112 \rangle$	[18, 19]
14YWT	-		-	-	[84]
MA957	2.4	8.5×10^{23}			[98]
Cold-Sprayed, 1100° C free	Not found	$< 5.8 \times 10^{19}$	2370 ± 910 7810 ± 1520	None	This work

Table A.12: Microstructural properties of 14YWT and other ODS alloys found in this and other works.

Bibliography

[1] Conference Paper. Nov. 2010.

[2] Personal Communication. Aug. 2019.

[3] Personal Communication. 2019.

[4] Personal Communication. Oct. 2019.

[5] GE Additive. Press Release. 2020. URL: `https://www.ge.com/additive/additive-manufacturing`.

[6] Kazi F. Ahmmed et al. “Thermal creep behavior in heat-treated and modified textured Zr -Excel pressure tube material”. In: *Materials Science and Engineering: A* 698 (2017), pp. 326–340. ISSN: 09215093. DOI: `10.1016/j.msea.2017.05.005`.

[7] H. C. Akuezue and D. P. Whittle. “Interdiffusion in Fe-Al system: aluminizing”. In: *Metal Science* 17.1 (2013), pp. 27–31. ISSN: 0306-3453. DOI: `10.1179/msc.1983.17.1.27`.

[8] M. E. Alam et al. “On delamination toughening of a 14YWT nanostructured ferritic alloy”. In: *Acta Materialia* 136 (2017), pp. 61–73. DOI: `10.1016/j.actamat.2017.06.041`.

[9] M. J. Alinger, G. R. Odette, and D. T. Hoelzer. “On the role of alloy composition and processing parameters in nanocluster formation and dispersion strengthening in nanostuctured ferritic alloys”. In: *Acta Materialia* 57.2 (2009), pp. 392–406. ISSN: 13596454. DOI: `10.1016/j.actamat.2008.09.025`.

[10] M. J. Alinger, G. R. Odette, and D. T. Hoelzer. “The development and stability of Y-Ti-O nanoclusters in mechanically alloyed Fe-Cr based ferritic alloys”. In: *Journal of Nuclear Materials* 329-333 (2004), pp. 382–386. ISSN: 00223115. DOI: `10.1016/j.jnucmat.2004.04.042`.

[11] M. Alinger, G. R. Odette, and G. E. Lucas. “Tensile and fracture toughness properties of MA957: implications to the development of nanocomposited ferritic alloys”. In: *Journal of Nuclear Materials* 307-311 (2002), pp. 484–489.

[12] Lallit Anand and Sanjay Govindjee. *Introduction to Mechanics of Solid Materials.* 2018.

[13] H. Assadi et al. "Cold spraying — A materials perspective". In: *Acta Materialia* 116 (2016), pp. 382–407. ISSN: 13596454. DOI: `10.1016/j.actamat.2016.06.034`.

[14] H. Assadi et al. "Comment on "Adiabatic shear instability is not necessary for adhesion in cold spray"S". In: *Scripta Materialia* 162 (2019), pp. 512–514. ISSN: 13596462. DOI: `10.1016/j.scriptamat.2018.10.036`.

[15] H. Assadi et al. "On Parameter Selection in Cold Spraying". In: *Journal of Thermal Spray Technology* 20.6 (2011), pp. 1161–1176. ISSN: 1059-9630 1544-1016. DOI: `10.1007/s11666-011-9662-9`.

[16] Hamid Assadi et al. "Bonding mechanism in cold gas spraying". In: *Acta Materialia* 51.15 (2003), pp. 4379–4394. ISSN: 13596454. DOI: `10.1016/s1359-6454(03)00274-x`.

[17] ASTM. *E2627 Standard Practice for Determining Average Grain Size Using Electron Backscatter Diffraction (EBSD) in Fully Recrystallized Polycrystalline Materials*. Standard. 2019.

[18] E. Aydogan et al. "Effect of tube processing methods on microstructure, mechanical properties and irradiation response of 14YWT nanostructured ferritic alloys". In: *Acta Materialia* 134 (2017), pp. 116–127. DOI: `10.1016/j.actamat.2017.05.053`.

[19] E. Aydogan et al. "Effect of tube processing methods on the texture and grain boundarycharacteristics of 14YWT nanostructured ferritic alloys". In: *Materials Science and Engineering: A* 661 (2016), pp. 222–232. DOI: `10.1016/j.msea.2016.02.085`.

[20] Sara Bagherifard et al. "Cold spray deposition for additive manufacturing of freeform structural components compared to selective laser melting". In: *Materials Science and Engineering: A* 721 (2018), pp. 339–350. ISSN: 09215093. DOI: `10.1016/j.msea.2018.02.094`.

[21] N. Bala et al. "Cold spray coating process for corrosion protection: a review". In: *Surface Engineering* 30.6 (2013), pp. 414–421. ISSN: 0267-0844 1743-2944. DOI: `10.1179/1743294413y.0000000148`.

[22] L. Barnard et al. "An ab initio study of Ti-Y-O nanocluster energetics in nanostructured ferritic alloys". In: *Acta Materialia* 60.3 (2012), pp. 935–947. ISSN: 13596454. DOI: `10.1016/j.actamat.2011.11.011`.

[23] Craig R Barrett, William D Nix, and Oleg D Sherby. *The Influence of Strain and Grain Size on the Creep Substructure of Fe-3.0% SI*. Report. Stanford University Dept of Materials Science, 1965.

[24] M. Batista and J. Usenik. "Stresses in a circular ring under two forces acting along a diameter". In: *Journal of Strain Analysis* 31.1 (1996), p. 4.

[25] J. R. Beeler. "Displacement Spikes in Cubic Metals. I. α-Iron, Copper, and Tungsten". In: *Physical Review* 150.2 (1966), pp. 470–487. ISSN: 0031-899X. DOI: `10.1103/PhysRev.150.470`.

[26] Venkata Satish Bhattiprolu et al. "Influence of feedstock powder and cold spray processing parameters on microstructure and mechanical properties of Ti-6Al-4V cold spray depositions". In: *Surface and Coatings Technology* 335 (2018), pp. 1–12. ISSN: 02578972. DOI: `10.1016/j.surfcoat.2017.12.014`.

[27] R. A. Buswell et al. "3D printing using concrete extrusion: A roadmap for research". In: *Cement and Concrete Research* 112 (2018), pp. 37–49. ISSN: 00088846. DOI: `10.1016/j.cemconres.2018.05.006`.

[28] Thak Sang Byun et al. "High temperature fracture characteristics of a nanostructured ferritic alloy (NFA)". In: *Journal of Nuclear Materials* 407.2 (2010), pp. 78–82. ISSN: 00223115. DOI: `10.1016/j.jnucmat.2010.09.031`.

[29] William D. Callister. *Materials Science and Engineering: An Introduction*. Second. John Wiley & Sons, 1991. ISBN: 0471504882.

[30] V. de Castro, S. Lozano-Perez, and M. L. Jenkins. "Stability of nanoparticles in an oxide dispersion strengthened alloy". In: *Journal of Physics: Conference Series* 241 (2010). ISSN: 1742-6596. DOI: `10.1088/1742-6596/241/1/012107`.

[31] V. de Castro et al. "Microstructural characterization of Y_2O_3 ODS-Fe-Cr model alloys". In: *Journal of Nuclear Materials* 386-388 (2009), pp. 449–452. ISSN: 00223115. DOI: `10.1016/j.jnucmat.2008.12.136`.

[32] M. B. Chadwick et al. "ENDF/B-VII.1 Nuclear Data for Science and Technology: Cross Sections, Covariances, Fission Product Yields and Decay Data". In: *Nuclear Data Sheets* 112.12 (2011), pp. 2887–2996. ISSN: 00903752. DOI: `10.1016/j.nds.2011.11.002`.

[33] Hanqing Che, Phuong Vo, and Stephen Yue. "Metallization of carbon fibre reinforced polymers by cold spray". In: *Surface and Coatings Technology* 313 (2017), pp. 236–247. ISSN: 02578972. DOI: `10.1016/j.surfcoat.2017.01.083`.

[34] Richard E. Chinn. *Ceramography: Preparation and Analysis of Ceramic Microstructures*. Materials Park, OH: ASM International, 2002. ISBN: 0-87170-770-5.

[35] Winston S. Churchill. *Speech given on the occasion of the Allied victory at El Alamein*. Nov. 1942.

[36] Wikimedia Commons. *File:Binding energy curve - common isotopes.svg — Wikimedia Commons, the free media repository*. [Online; accessed 5-December-2019]. 2019. URL: `https://commons.wikimedia.org/w/index.php?title=File:Binding_energy_curve_-_common_isotopes.svg&oldid=362996012`.

[37] N. Cunningham et al. *Characterization of a Larger Best Practice Heat of 14YWT in Annealed Powder, HIP Consolidated and Extruded Forms*. Report. 2013.

[38] D Das, I. Manna Chatterjee, and S. K. Pabi. "A MEASURE OF ENHANCED DIFFUSION KINETICS IN MECHANICAL ALLOYING OF Cu-18 at.% Al BY PLANETARY BALL MILLING". In: *Scripta Materialia* 41.8 (1999), pp. 861–866.

[39] Karl Dawson et al. “Nano-particle precipitation in mechanically alloyed and annealed precursor powders of legacy PM2000 ODS alloy”. In: *Journal of Nuclear Materials* 464 (2015), pp. 200–209. ISSN: 00223115. DOI: `10.1016/j.jnucmat.2015.04.039`.

[40] R Devanathan et al. “Cryogenic radiation response of sapphire”. In: *Nuclear Instruments and Methods in Physics Research Section B: Beam Interactions with Materials and Atoms* 141.1 (1998), pp. 366–371. ISSN: 0168-583X. DOI: `https://doi.org/10.1016/S0168-583X(98)00190-6`. URL: `http://www.sciencedirect.com/science/article/pii/S0168583X98001906`.

[41] Thomas James Dolan. *Magnetic Fusion Technology*. London: Springer, 2013. ISBN: 9781447155560. URL: `https://doi.org/10.1007/978-1-4471-5556-0`.

[42] P. Dubey et al. “Effect of bias induced microstructure on the mechanical properties of nanocrystalline zirconium tungsten nitride coatings”. In: *Surface and Coatings Technology* 313 (2017), pp. 121–128. ISSN: 02578972. DOI: `10.1016/j.surfcoat.2017.01.067`.

[43] E. D. Easton et al. *A Physically Based Correlation of Irradiation-Induced Transition Temperature Shifts for RPV Steels*. Report ORNL/TM-2006/530. 2006.

[44] Anthony C. Fischer-Cripps. *Nanoindentation*. New York, NY: Springer, 2011. ISBN: 978-1-4419-9872-9. DOI: `https://doi.org/10.1007/978-1-4419-9872-9`.

[45] John Joseph Fischer. Patent. 1978.

[46] H.J. Frost and M.F. Ashby. *Deformation-mechanism maps: the plasticity and creep of metals and ceramics*. Pergamon Press, 1982. ISBN: 9780080293370. URL: `https://books.google.com/books?id=s9BRAAAAMAAJ`.

[47] H. Fuess. *International Tables for Crystallography, Online MRW*. International Tables for Crystallography. Wiley, 2010. ISBN: 9780470685754. URL: `https://books.google.com/books?id=wvGSyAEACAAJ`.

[48] B. Fultz and J.M. Howe. *Transmission Electron Microscopy and Diffractometry of Materials*. Springer Berlin Heidelberg, 2012. ISBN: 9783642297601. URL: `https://books.google.com/books?id=tgOC3vlEY0sC`.

[49] Anastasios G. Gavras et al. “Effects of processing on microstructure evolution and fatigue crack growth mechanisms in cold-spray 6061 aluminum alloy”. In: *International Journal of Fatigue* 110 (2018), pp. 49–62. ISSN: 01421123. DOI: `10.1016/j.ijfatigue.2018.01.006`.

[50] Michael A. Gibson et al. “3D printing metals like thermoplastics: Fused filament fabrication of metallic glasses”. In: *Materials Today* 21.7 (2018), pp. 697–702. ISSN: 13697021. DOI: `10.1016/j.mattod.2018.07.001`.

[51] E. Gil et al. “XPS and SEM analysis of the surface of gas atomized powder precursor of ODS ferritic steels obtained through the STARS route”. In: *Applied Surface Science* 427 (2018), pp. 182–191. ISSN: 01694332. DOI: `10.1016/j.apsusc.2017.07.205`.

[52] Technische Universität Graz. Web database. 2020. URL: `http://lampx.tugraz.at/~hadley/ss1/crystaldiffraction/atomicformfactors/formfactors.php`.

[53] H. Hadraba et al. “Influence of microstructure on impact properties of 9-18%Cr ODS steels for fusion/fission applications”. In: *Journal of Nuclear Materials* 411.1-3 (2011), pp. 112–118. ISSN: 00223115. DOI: `10.1016/j.jnucmat.2011.01.038`.

[54] Hynek Hadraba et al. “Microstructure and impact properties of ferritic ODS ODM401 (14%Cr - ODS of MA957 type)”. In: *Journal of Nuclear Materials* 417 (2011), pp. 241–244. DOI: `10.1016/j.jnucmat.2011.01.066`.

[55] M. L. Hamilton et al. *Fabrication Technological Development of the Oxide Dispersion Strengthened Alloy MA957 for Fast Reactor Applications*. Report. 2000.

[56] Jianchao He et al. “Stability of nanoclusters in 14YWT oxide dispersion strengthened steel under heavy ion-irradiation by atom probe tomography”. In: *Journal of Nuclear Materials* 455.1-3 (2014), pp. 41–45. ISSN: 00223115. DOI: `10.1016/j.jnucmat.2014.03.024`.

[57] D. F. Heaney and C. Binet. “Hot isostatic pressing (HIP) of metal injection molding (MIM)”. In: *Handbook of Metal Injection Molding*. 2019, pp. 195–202. ISBN: 9780081021521. DOI: `10.1016/b978-0-08-102152-1.00011-8`.

[58] Herbert Heinrich. “The Discovery of Galvanoplasty and Electrotyping”. In: *Journal of Chemical Education* 15.12 (1938). DOI: `10.1021/ed015p565a`.

[59] R.W. Hertzberg. *Deformation and fracture mechanics of engineering materials*. Wiley, 1989. ISBN: 9780471635895. URL: `https://books.google.com/books?id=3LFRAAAAMAAJ`.

[60] D. T. Hoelzer et al. “Influence of processing on the microstructure and mechanical properties of 14YWT”. In: *Journal of Nuclear Materials* 471 (2016), pp. 251–265. ISSN: 00223115. DOI: `10.1016/j.jnucmat.2015.12.011`.

[61] J. Horton. Audiovisual Material. 2000. URL: `https://commons.wikimedia.org/wiki/File:Dqsk-steel-bainitic-weld-tem-image.png`.

[62] P. Hosemann. “Irradiation Effects in Materials Lecture Notes”. Unpublished Work. Berkeley, CA, 2019.

[63] Y. Huang, J. D. Robson, and P. B. Prangnell. “The formation of nanograin structures and accelerated room-temperature theta precipitation in a severely deformed Al-4wt.% Cu alloy”. In: *Acta Materialia* 58.5 (2010), pp. 1643–1657. ISSN: 13596454. DOI: `10.1016/j.actamat.2009.11.008`.

[64] J. A. Hudson. “Tensile Strength and the Ring Test”. In: *International Journal of Rock Mechanicics and Mining Sciences* 6.1 (1968), pp. 91–97.

[65] William Hume-Rothery and Geoffrey Vincent Raynor. *The structure of metals and alloys*. London: Institute of Metals, 1956.

[66] Ian Hutchings and Philip Shipway. "Design and selection of materials for tribological applications". In: *Tribology.* 2017, pp. 283–302. ISBN: 9780081009109. DOI: `10.1016/b978-0-08-100910-9.00008-8`.

[67] Ian Hutchings and Philip Shipway. "Sliding wear". In: *Tribology.* 2017, pp. 107–164. ISBN: 9780081009109. DOI: `10.1016/b978-0-08-100910-9.00005-2`.

[68] Ian Hutchings and Philip Shipway. "Surface engineering". In: *Tribology.* 2017, pp. 237–281. ISBN: 9780081009109. DOI: `10.1016/b978-0-08-100910-9.00007-6`.

[69] IAEA. *Applicability of the leak before break concept.* Report. IAEA, June 1993.

[70] ASTM International. *Standard Specification for Chromium and Chromium - Nickel Stainless Steel Plate, Sheet, and Strip for Pressure Vessels and for General Applications.* Report A240/A240M-18. ASTM International, 2018. DOI: `https://doi.org/10.1520/A0240\_A0240M-18`.

[71] G. Irwin. "Fracture Dynamics". In: *Fracturing of Metals.* Materials Park, OH: American Society for Metals, 1948.

[72] G. R. Irwin. "Structural aspects of brittle fracture". In: *Applied Materials Research* 3.2 (1964), pp. 65–81.

[73] Keiichiro Oh-ishi et al. "High-pressure torsion for enhanced atomic diffusion and promoting solid-state reactions in the aluminum-copper system". In: *Acta Materialia* 61.9 (2013), pp. 3482–3489. ISSN: 13596454. DOI: `10.1016/j.actamat.2013.02.042`.

[74] Yosuke Iwamoto et al. "Measurement of displacement cross sections of aluminum and copper at 5K by using 200 MeV protons". In: *Journal of Nuclear Materials* 508 (2018), pp. 195–202. ISSN: 0022-3115. DOI: `https://doi.org/10.1016/j.jnucmat.2018.05.038`. URL: `http://www.sciencedirect.com/science/article/pii/S0022311518303970`.

[75] Anubhav Jain et al. "Commentary: The Materials Project: A materials genome approach to accelerating materials innovation". In: *APL Materials* 1.1 (2013), p. 011002. DOI: `10.1063/1.4812323`. eprint: `https://doi.org/10.1063/1.4812323`. URL: `https://doi.org/10.1063/1.4812323`.

[76] Josh Kacher et al. "Dislocation interactions with grain boundaries". In: *Current Opinion in Solid State and Materials Science* 18.4 (2014), pp. 227–243. ISSN: 13590286. DOI: `10.1016/j.cossms.2014.05.004`.

[77] Nan Kang et al. "Microstructure and wear properties of selective laser melted WC reinforced 18Ni-300 steel matrix composite". In: *Vacuum* 154 (2018), pp. 69–74. ISSN: 0042207X. DOI: `10.1016/j.vacuum.2018.04.044`.

[78] Ryuta Kasada et al. "Anisotropy in tensile and ductile-brittle transition behavior of ODS ferritic steels". In: *Journal of Nuclear Materials* 417 (2011), pp. 180–184. DOI: `10.1016/j.jnucmat.2010.12.069`.

[79] C. Kenel et al. “Microstructure and oxide particle stability in a novel ODS γ-TiAl alloy processed by spark plasma sintering and laser additive manufacturing”. In: *Intermetallics* 90 (2017), pp. 63–73. ISSN: 09669795. DOI: `10.1016/j.intermet.2017.07.004`.

[80] C. Kenel et al. “Selective laser melting of an oxide dispersion strengthened (ODS) γ-TiAl alloy towards production of complex structures”. In: *Materials & Design* 134 (2017), pp. 81–90. ISSN: 02641275. DOI: `10.1016/j.matdes.2017.08.034`.

[81] Jeoung Han Kim, Thak Sang Byun, and D. T. Hoelzer. “Tensile fracture characteristics of nanostructured ferritic alloy 14YWT”. In: *Journal of Nuclear Materials* 407.3 (2010), pp. 143–150. ISSN: 00223115. DOI: `10.1016/j.jnucmat.2010.09.054`.

[82] Akihiko Kimura et al. “High Burnup Fuel Cladding Materials R&D for Advanced Nuclear Systems”. In: *Journal of Nuclear Science and Technology* 44 (2007), pp. 323–328. DOI: `10.1080/18811248.2007.9711289`.

[83] H. Kishimoto et al. “TEM examination of microstructural evolution during processing of 14CrYWTi nanostructured ferritic alloys”. In: *Journal of Nuclear Materials* 329-333 (2004), pp. 369–371. ISSN: 00223115. DOI: `10.1016/j.jnucmat.2004.04.044`.

[84] David Krumwiede. “Correlation of Nanohardness to Bulk Mechanical Tensile and Shear Properties through Direct Characterization and Comparison of Neutron-Irradiated Steels”. Thesis. 2018.

[85] John R. Lamarsh and Anthony J. Baratta. *Introduction to Nuclear Engineering*. 3rd. Upper Saddle River, NJ: Prentice-Hall Inc., 2001. ISBN: 0-201-82498-1.

[86] Y. Leng. *Materials Characterization: Introduction to Microscopic and Spectroscopic Methods*. Wiley, 2008. ISBN: 9780470822982. URL: `https://books.google.com/books?id=R6weAQAAIAAJ`.

[87] Mia Lenling. Personal Communication. June 2019.

[88] Mia Lenling. “Development of the Cold Spray Process for Manufacturing and Surface Modification of Oxide Dispersion Strengthened (ODS) Stell Fuel Cladding Tubes”. Thesis. 2019.

[89] Mia Lenling et al. “Manufacturing Oxide Dispersion-Strengthened (ODS) Steel Fuel Cladding Tubes Using the Cold Spray Process”. In: *Jom* 71.8 (2019), pp. 2868–2873. ISSN: 1047-4838 1543-1851. DOI: `10.1007/s11837-019-03582-w`.

[90] A. Leyland and A. Matthews. “On the significance of the H/E ratio in wear control: a nanocomposite coating approach to optimized tribological behaviour”. In: *Wear* 246 (2000), pp. 1–11.

[91] W. Li and R. A. Holt. “Anisotropic thermal creep of internally pressurized Zr-2.5Nb tubes”. In: *Journal of Nuclear Materials* 401.1-3 (2010), pp. 25–37. ISSN: 00223115. DOI: `10.1016/j.jnucmat.2010.03.015`.

[92] Yanfen Li et al. "Effects of fabrication processing on the microstructure and mechanical properties of oxide dispersion strengthening steels". In: *Materials Science and Engineering: A* 654 (2016), pp. 203–212. ISSN: 09215093. DOI: `10.1016/j.msea.2015.12.032`.

[93] Tian Liu, Jeremy D. Leazer, and Luke N. Brewer. "Particle deformation and microstructure evolution during cold spray of individual Al-Cu alloy powder particles". In: *Acta Materialia* 168 (2019), pp. 13–23. ISSN: 13596454. DOI: `10.1016/j.actamat.2019.01.054`.

[94] D. Macaulay. *The Way Things Work*. Houghton Mifflin, 1988. ISBN: 9780395428573. URL: `https://books.google.com/books?id=CF0hAQAAIAAJ`.

[95] Benjamin Maier et al. "A novel approach for manufacturing oxide dispersion strengthened (ODS) steel cladding tubes using cold spray technology". In: *Nuclear Engineering and Technology* (2019). ISSN: 17385733. DOI: `10.1016/j.net.2019.01.015`.

[96] Benjamin Maier et al. "Cold spray fabrication of oxide dispersion strengthened steal fuel cladding". In: *National Academy Keck Futures Initiave (NAKFI) Mid-Cycle Meeting*.

[97] J. R. Matthews and M. W. Finnis. "Irradiation Creep Models—An Overview". In: *Journal of Nuclear Materials* 159 (1988), pp. 257–285.

[98] P. Miao et al. "The microstructure and strength properties of MA957 nanostructured ferritic alloy joints produced by friction stir and electro-spark deposition welding". In: *Journal of Nuclear Materials* 367-370 (2007), pp. 1197–1202. ISSN: 00223115. DOI: `10.1016/j.jnucmat.2007.03.232`.

[99] M. Militzer, W. P. Sun, and J. J. Jonas. "Modelling the effect of deformation-induced vacancies on segregation and precipitation". In: *Acta Metallurgica et Materialia* 42.1 (1994), pp. 133–141.

[100] Andrew M. Minor. *MSE 204: Theory of Electron Microscopy and X-Ray Diffraction, Lecture 13*. Lecture Material. 2017.

[101] Roghayeh Mohammadzadeh. "Analysis of plastic strain-enhanced diffusivity in nanocrystalline iron by atomistic simulation". In: *Journal of Applied Physics* 125.13 (2019), p. 135103. DOI: `10.1063/1.5085659`. URL: `https://aip.scitation.org/doi/abs/10.1063/1.5085659`.

[102] E. Morse. *Nuclear Fusion*. Springer International Publishing, 2018. ISBN: 9783319981710. URL: `https://books.google.com/books?id=z6VyDwAAQBAJ`.

[103] L. E. Murr. "Metallurgy principles applied to powder bed fusion 3D printing/additive manufacturing of personalized and optimized metal and alloy biomedical implants: an overview". In: *Journal of Materials Research and Technology* 9.1 (2020), pp. 1087–1103. ISSN: 22387854. DOI: `10.1016/j.jmrt.2019.12.015`.

[104] K. L. Murty, B. V. Tanikella, and J. C. Earthman. “Effect of grain shape and texture on exqui-biaxial creep of stress relieved and recrystallized zircaloy-4”. In: *Acta Metallurgica et Materialia* 42.11 (1994), pp. 3653–3661.

[105] Y. Nasedkina et al. “Mechanisms of precipitation induced by large strains in the Al-Cu system”. In: *Journal of Alloys and Compounds* 710 (2017), pp. 736–747. ISSN: 09258388. DOI: `10.1016/j.jallcom.2017.03.312`.

[106] NIST. Web Page. 2020. URL: `https://www.nist.gov/topics/additive-manufacturing`.

[107] T. L. Oberle. “Properties Influencing Wear of Metals”. In: *JOM* 3.6 (1951), pp. 438–439.

[108] G. R. Odette. “On mechanisms controlling swelling in ferritic and martensitic alloys”. In: *Journal of Nuclear Materials* 155-157 (1988), pp. 921–927.

[109] G. R. Odette, M. J. Alinger, and B. D. Wirth. “Recent Developments in Irradiation-Resistant Steels”. In: *Annual Review of Materials Research* 38.1 (2008), pp. 471–503. ISSN: 1531-7331 1545-4118. DOI: `10.1146/annurev.matsci.38.060407.130315`.

[110] G. R. Odette and G. E. Lucas. “Embrittlement of nuclear reactor pressure vessels”. In: *JOM* 53.7 (2001), pp. 18–22. ISSN: 1543-1851. DOI: `10.1007/s11837-001-0081-0`. URL: `https://doi.org/10.1007/s11837-001-0081-0`.

[111] G. R. Odette and R. K. Nanstad. “Predictive Reactor Pressure Vessel Steel Irradiation Embrittlement Models: Issues and Opportunities”. In: *JOM* 61.7 (2009), pp. 17–23.

[112] D.R. Olander et al. *Fundamental aspects of nuclear reactor fuel elements: prepared for the Division of Reactor Development and Demonstration, Energy Research and Development Administration*. Technical Information Center, Office of Public Affairs, Energy Research and Development Administration, 1976. ISBN: 9780870790317. URL: `https://books.google.com/books?id=2PdTAAAAMAAJ`.

[113] W. C. Oliver and G. M. Pharr. “An improved technique for determining hardness and elastic modulus using load and displacement sensing indentation experiments”. In: *Journal of Materials Research* 7.6 (2011), pp. 1564–1583. ISSN: 0884-2914 2044-5326. DOI: `10.1557/jmr.1992.1564`.

[114] J. Pattison et al. “Cold gas dynamic manufacturing: A non-thermal approach to freeform fabrication”. In: *International Journal of Machine Tools and Manufacture* 47.3-4 (2007), pp. 627–634. ISSN: 08906955. DOI: `10.1016/j.ijmachtools.2006.05.001`.

[115] David Pazos et al. “ODS ferritic steels obtained from gas atomized powders through the STARS processing route: Reactive synthesis as an alternative to mechanical alloying”. In: *Nuclear Materials and Energy* 17 (2018), pp. 1–8. ISSN: 23521791. DOI: `10.1016/j.nme.2018.06.014`.

[116] K. Petráčková, J. Kondás, and M. Guagliano. "Fixing a hole (with cold spray)". In: *International Journal of Fatigue* 110 (2018), pp. 144–152. ISSN: 01421123. DOI: `10.1016/j.ijfatigue.2018.01.014`.

[117] Oxford Instruments PLC. *Grain Size and Grain Boundary Characterisation in SEM.* Web Page. 2020. URL: `https://www.ebsd.com/solving-problems-with-ebsd/grain-size-and-grain-boundary-characterisation-in-sem`.

[118] B. B. Rath and I. M. Bernstein. "The relation between grain-boundary orientation and intergranular cracking". In: *Metallurgical Transactions* 2 (1971), pp. 2972–2845.

[119] J. R. Rieken et al. "Reactive gas atomization processing for Fe-based ODS alloys". In: *Journal of Nuclear Materials* 428.1-3 (2012), pp. 65–75. ISSN: 00223115. DOI: `10.1016/j.jnucmat.2011.08.015`.

[120] A. L. Rouffié et al. "Influences of process parameters and microstructure on the fracture mechanisms of ODS steels". In: *Journal of Nuclear Materials* 433.1-3 (2013), pp. 108–115. ISSN: 00223115. DOI: `10.1016/j.jnucmat.2012.08.050`.

[121] Tobias Schmidt et al. "Development of a generalized parameter window for cold spray deposition". In: *Acta Materialia* 54.3 (2006), pp. 729–742. ISSN: 13596454. DOI: `10.1016/j.actamat.2005.10.005`.

[122] Tobias Schmidt et al. "From Particle Acceleration to Impact and Bonding in Cold Spraying". In: *Journal of Thermal Spray Technology* 18.5-6 (2009), pp. 794–808. ISSN: 1059-9630 1544-1016. DOI: `10.1007/s11666-009-9357-7`.

[123] Marta Serrano, Mercedes Hernández-Mayoral, and Andrea García-Junceda. "Microstructural anisotropy effect on the mechanical properties of a 14Cr ODS steel". In: *Journal of Nuclear Materials* 428.1-3 (2012), pp. 103–109. ISSN: 00223115. DOI: `10.1016/j.jnucmat.2011.08.016`.

[124] Jingjie Shen et al. "Microstructural characterization and strengthening mechanisms of a 12Cr-ODS steel". In: *Materials Science and Engineering: A* 673 (2016), pp. 624–632. ISSN: 09215093. DOI: `10.1016/j.msea.2016.07.030`.

[125] R. Singh et al. "Influence of coating thickness on residual stress and adhesion-strength of cold-sprayed Inconel 718 coatings". In: *Surface and Coatings Technology* 350 (2018), pp. 64–73. ISSN: 02578972. DOI: `10.1016/j.surfcoat.2018.06.080`.

[126] R. E. Smallman and A. H. W. Ngan. "Precipitation Hardening". In: *Modern Physical Metallurgy.* 2014, pp. 499–527. ISBN: 9780080982045. DOI: `10.1016/b978-0-08-098204-5.00013-4`.

[127] A. Steckmeyer et al. "Tensile anisotropy and creep properties of a Fe—14CrWTi ODS ferritic steel". In: *Journal of Nuclear Materials* 426.1-3 (2012), pp. 182–188. ISSN: 00223115. DOI: `10.1016/j.jnucmat.2012.03.016`.

[128] Thorsten Stoltenhoff, Joel Voyer, and H. Kreye. "Cold Spraying - State of the Art and Applicability". In: *International Thermal Spray Conference, 2002* (2002).

[129] J. L. Straalsund, R. W. Powell, and B. A. Chin. "An overview of neutron irradiation effects in LMFBR materials". In: *Journal of Nuclear Materials* 108 & 109 (1982), pp. 299–305.

[130] K.S. Thorne and R.D. Blandford. *Modern Classical Physics: Optics, Fluids, Plasmas, Elasticity, Relativity, and Statistical Physics*. Princeton University Press, 2017. ISBN: 9781400848898. URL: `https://books.google.com/books?id=U1S6BQAAQBAJ`.

[131] S. Ukai. "Oxide Dispersion Strengthened Steels". In: *Comprehensive Nuclear Materials*. 2012, pp. 241–271. ISBN: 9780080560335. DOI: `10.1016/b978-0-08-056033-5.00069-0`.

[132] S. Ukai et al. "Alloying design of oxide dispersion strengthened ferritic steel for long life FBRs core materials". In: *Journal of Nuclear Materials* 204 (1993), pp. 65–73.

[133] Dien Wang et al. "Ultrafast laser-enabled 3D metal printing: A solution to fabricate arbitrary submicron metal structures". In: *Precision Engineering* 52 (2018), pp. 106–111. ISSN: 01416359. DOI: `10.1016/j.precisioneng.2017.11.015`.

[134] G.S. Was. *Fundamentals of Radiation Materials Science: Metals and Alloys*. Springer New York, 2016. ISBN: 9781493934386. URL: `https://books.google.com/books?id=yDGmDAAAQBAJ`.

[135] E. L. Wheeler. *Scientific glassblowing ; with a pref. by G. Ross Robertson*. New York: Interscience Pub., 1958, 478 p. URL: `//catalog.hathitrust.org/Record/001043757%20http://hdl.handle.net/2027/mdp.39015054392637%20http://hdl.handle.net/2027/uc1.b3421925`.

[136] Markus B. Wilms et al. "Laser additive manufacturing of oxide dispersion strengthened steels using laser-generated nanoparticle-metal composite powders". In: *Procedia CIRP* 74 (2018), pp. 196–200. ISSN: 22128271. DOI: `10.1016/j.procir.2018.08.093`.

[137] W. G. Wolfer. "Fundamental Properties of Defects in Metals". In: *Comprehensive Nuclear Materials*. 2012, pp. 1–45. ISBN: 9780080560335. DOI: `10.1016/b978-0-08-056033-5.00001-x`.

[138] Yuan Wu et al. "The crystal structure, orientation relationships and interfaces of the nanoscale oxides in nanostructured ferritic alloys". In: *Acta Materialia* 111 (2016), pp. 108–115. ISSN: 13596454. DOI: `10.1016/j.actamat.2016.03.031`.

[139] Shuo Yin et al. "Cold spray additive manufacturing and repair: Fundamentals and applications". In: *Additive Manufacturing* 21 (2018), pp. 628–650. ISSN: 2214-8604. DOI: `https://doi.org/10.1016/j.addma.2018.04.017`. URL: `http://www.sciencedirect.com/science/article/pii/S2214860417302993`.

[140] Clarence Zener. "Theory of Growth of Spherical Precipitates from Solid Solution". In: *Journal of Applied Physics* 20.10 (1949), pp. 950–953. ISSN: 0021-8979 1089-7550. DOI: `10.1063/1.1698258`.

[141] S. J. Zinkle and G. S. Was. “Materials challenges in nuclear energy”. In: *Acta Materialia* 61.3 (2013), pp. 735–758. ISSN: 13596454. DOI: `10.1016/j.actamat.2012.11.004`.